



**PROVIDING A THEORETICAL BASIS FOR
NANOTOXICITY RISK ANALYSIS
DEPARTING FROM TRADITIONAL
PHYSIOLOGICALLY-BASED
PHARMACOKINETIC (PBPK) MODELING**

DISSERTATION

Dirk P. Yamamoto, Lt Col, USAF, BSC
AFIT/DS/ENV/10-S01

**DEPARTMENT OF THE AIR FORCE
AIR UNIVERSITY**

AIR FORCE INSTITUTE OF TECHNOLOGY

Wright-Patterson Air Force Base, Ohio

APPROVED FOR PUBLIC RELEASE; DISTRIBUTION UNLIMITED

The views expressed in this document are those of the author and do not reflect the official policy or position of the United States Air Force, the Department of Defense, or the United States Government.

AFIT/DS/ENV/10-S01

PROVIDING A THEORETICAL BASIS FOR NANOTOXICITY RISK
ANALYSIS DEPARTING FROM TRADITIONAL PHYSIOLOGICALLY-BASED
PHARMACOKINETIC (PBPK) MODELING

DISSERTATION

Presented to the Faculty
Graduate School of Engineering and Management
Air Force Institute of Technology
Air University
Air Education and Training Command
in Partial Fulfillment of the Requirements for the
Degree of Doctor of Philosophy

Dirk P. Yamamoto, BS, MS, MSPH
Lt Col, USAF, BSC

September 2010

APPROVED FOR PUBLIC RELEASE; DISTRIBUTION UNLIMITED

AFIT/DS/ENV/10-S01

PROVIDING A THEORETICAL BASIS FOR NANOTOXICITY RISK
ANALYSIS DEPARTING FROM TRADITIONAL PHYSIOLOGICALLY-BASED
PHARMACOKINETIC (PBPK) MODELING

Dirk P. Yamamoto, BS, MS, MSPH
Lt Col, USAF, BSC

Approved:

//signed//

September 2010

Dr. Michael L. Shelley
Chairman

Date

//signed//

September 2010

Dr. William P. Baker
Member

Date

//signed//

September 2010

Dr. John M. Colombi
Member

Date

Accepted:

//signed//

September 2010

M. U. Thomas
Dean, Graduate School of Engineering
and Management

Date

Abstract

The same novel properties of engineered nanoparticles that make them attractive may also present unique exposure risks. But, the traditional physiologically-based pharmacokinetic (PBPK) modeling assumption of instantaneous equilibration likely does not apply to nanoparticles. This simulation-based research begins with development of a model that includes diffusion, active transport, and carrier mediated transport. An eigenvalue analysis methodology was developed to examine model behavior to focus future research. Simulations using the physico-chemical properties of size, shape, surface coating, and surface charge were performed and an equation was determined which estimates area under the curve for arterial blood concentration, which is a surrogate of nanoparticle dose.

Results show that the cellular transport processes modeled in this research greatly affect the biokinetics of nanoparticles. Evidence suggests that the equation used to estimate area under the curve for arterial blood concentration can be written in terms of nanoparticle size only. The new paradigm established by this research leverages traditional *in vitro*, *in vivo*, and PBPK modeling, but includes area under the curve to bridge animal testing results to humans. This new paradigm allows toxicologists and policymakers to then assess risk to a given exposure and assist in setting appropriate exposure limits for nanoparticles.

This research provides critical understanding of nanoparticle biokinetics and allows estimation of total exposure at any toxicological endpoint in the body. This effort is a significant contribution as it highlights future research needs and demonstrates how modeling can be used as a tool to advance nanoparticle risk assessment.

Acknowledgements

I would like to express my sincere appreciation to my advisor, Dr Mike Shelley, for his patience and coaching over the past three years. Keeping the student focused wasn't necessarily easy. I've learned more than you'll ever know. Dr John Colombi, thank you for always sharing your candid thoughts and recommending practical ways to tackle the complex problems. Special thanks goes to Lt Col Kyle Novak, who helped tremendously by educating me on how to apply mathematical rigor to build and analyze the pharmacokinetic model. His help in teaching me MATLAB[®] and L^AT_EX was critical to my successful completion. Finally, I thank Dr Bill Baker for stepping up late in the research to replace Lt Col Novak after he was deployed. You have confirmed that mathematics governs everything, including nanoparticle biokinetics in the human body.

Finally, an enormous amount of gratitude goes out to my family. To my parents: you taught me the most important lessons of life—work hard, always do your best, and education is a necessity. You've cheered me on my entire life and I owe all successes to you. To my children: yes, when dad goes to work, he does indeed sit in front of the computer all day long. This dissertation is eternal proof of that. Hopefully, you'll now understand that education never ends. Finally, to my wife: thank you for following me on this Air Force journey that has spanned (so far) 18 years, six assignments, three graduate degrees, SOS/ACSC/AWC, two AF tech schools, two board certifications/licenses, and countless TDY's. You've always viewed each new assignment and base with optimism and your tireless work makes it possible for me to focus on the mission. Thank you always for being there when I'm both physically and mentally absent...

Dirk P. Yamamoto

Table of Contents

	Page
Abstract	iv
Acknowledgements	v
List of Figures	viii
List of Tables	xii
List of Symbols	xiii
List of Abbreviations	xv
I. Introduction	1
1.1 Overview	1
1.2 Research Questions	2
1.3 Assumptions	3
II. Literature Review	5
2.1 Nanotoxicology	5
2.1.1 Absorption, Distribution, Metabolism, Excretion (ADME)	7
2.1.2 Organs of Concern	11
2.2 Cellular Transport	19
2.2.1 Simple Diffusion	20
2.2.2 Active Transport	21
2.2.3 Carrier Mediated Transport	22
2.2.4 Phagocytosis	23
2.3 Physiologically-Based Pharmacokinetic Modeling	25
2.3.1 Parameterizing	26
2.3.2 Traditional Assumptions of PBPK	27
2.4 Current State of Nano Risk Assessment	28
2.4.1 Risk Assessment Frameworks	28
2.4.2 Existing Models	31
III. Methodology	33
3.1 Phase I: Model Formulation	33
3.1.1 A Simple Three-Compartment Model	33
3.1.2 Additions to the Three-Compartment Model	36
3.1.3 The PBPK Model	40
3.1.4 Range Finding	48

	Page
3.1.5 Eigenvalue Analysis	52
3.2 Phase II: Inclusion of Physico-Chemical Properties	60
3.2.1 Size-Related Effects	61
3.2.2 Shape-Related Effects	76
3.2.3 Surface Coating Effects	78
3.2.4 Surface Charge Effects	79
3.3 Phase III: Defining a New Paradigm for Nano Risk Analysis	82
3.3.1 The Approach	83
IV. Results and Analysis	87
4.1 Phase I: Model Formulation Results	87
4.1.1 Range Finding Results	88
4.1.2 Comparison of Plots for Transport Processes	100
4.1.3 Eigenvalue Analysis Results	103
4.2 Phase II: Physico-Chemical Properties Results	108
4.2.1 Final Transport Equations	108
4.2.2 Physico-Chemical Simulations	110
4.3 Phase III: New Paradigm Results	112
4.3.1 Multiple Regression Analysis	112
4.3.2 An Alternative to Linear Regression	116
V. Conclusion	120
5.1 Addressing the Research Questions	121
5.2 Recommendations for the Future	123
Appendix A. Research Assumptions	125
Appendix B. Full PBPK Model in STELLA®	126
Appendix C. Model Ordinary Differential Equations (ODEs)	134
Appendix D. Matrix Formats for MATLAB® Model	158
Appendix E. Eigenvalue Analysis Background	167
Appendix F. Eigenstructure Matrices	176
Bibliography	180
Vita	188

List of Figures

Figure		Page
1	Potential consequences of nanoparticle exposures	6
2	Confirmed and potential routes for nanoparticle exposures	8
3	Cross-sectional view of liver lobule	14
4	Kidney glomerulus, surrounded by Bowman’s Capsule	16
5	Spleen anatomy	17
6	Tissue-to-blood partition coefficient	28
7	Hypothesized PBPK model for nanoparticles	32
8	Conceptual PBPK model, with three compartments	34
9	Three compartment model with source, exchange, loss	37
10	STELLA [®] icons used for modeling	39
11	Full PBPK model for nanoparticle exposures	41
12	Deposition in the respiratory tract, based on particle size	42
13	Eigenstructure format for full 24-subcompartment model	53
14	Subassemblies for the kidneys	56
15	Eigenstructure format for kidney three-subcompartment model	57
16	Eigenvalues and associated eigenvectors as $T_{e;i}$ is varied	57
17	Example: log-log plot of the eigenvalues for the kidney as $T_{e;i}$ is varied	58
18	Regions of the respiratory tract	61
19	Deposition in the respiratory tract, based on particle size	62
20	Interstitial translocation factor (ITF)	65

Figure		Page
21	Paracellular transport efficiency factor (PTEF)	66
22	Transcytosis efficiency factor (TEF)	67
23	Diagram of fenestrations in blood vessels	68
24	Liver accumulation factor (LAF)	70
25	Spleen accumulation factor (SPAF)	72
26	Kidney filtration efficiency factor (KFEF)	73
27	Brain paracellular efficiency factor (BPEF)	74
28	Phagocytosis size factor (PSF)	76
29	Cellular uptake efficiency factor (CUEF)	77
30	Cellular uptake shape factor (CUSF)	77
31	Phagocytosis coating factor (PCF))	80
32	Surface charge factor (SCF)	81
33	Instantaneous equilibration model	89
34	Nanoparticle concentrations for IE	89
35	Two-subcompartment model for $T_{b:t}$ range-finding	90
36	Nanoparticle concentrations for $T_{b:t}$ range finding	92
37	Tissue nanoparticle concentrations for $T_{b:t}=5$	92
38	Three-subcompartment model for $T_{e:i}$ range-finding	93
39	Nanoparticle concentrations for $T_{e:i}$ range finding	94
40	Tissue nanoparticle concentrations for $T_{e:i}=0.05$	94
41	Three-subcompartment model for $V_{\max at}$ range-finding	95
42	Nanoparticle concentrations for $V_{\max at}$ range finding	96
43	Tissue nanoparticle concentrations for $V_{\max at}=0.5$	97

Figure		Page
44	Three-subcompartment model for V_{maxcmt2} range-finding	98
45	Nanoparticle concentrations for V_{maxcmt2} range finding	99
46	Tissue nanoparticle concentrations for $V_{\text{maxcmt2}}=0.5$	99
47	Nanoparticle concentrations under various transport assumptions	101
48	Example: final operational concept with diffusion in parallel with active and carrier mediated transport	102
49	Example: first-order approximation of Michaelis-Menten kinetics.....	104
50	Comparison of the linearized and non-linear results.....	105
51	Eigenplots for the various organs.....	107
52	Eigenplots for the lungs and GI tract.....	107
53	Scatter plot showing area under the curve (AUC) for the simulations	111
54	3-d scatterplot of AUC vs. size vs. shape	113
55	3-d scatterplot of AUC vs. size vs. surface coating and surface charge	114
56	Plot of the regression equation vs. actual data	115
57	Parameter estimates for n=3000 simulations.....	116
58	Fitted equation.....	117
59	Lung representation in STELLA [®]	126
60	Liver representation in STELLA [®]	127
61	Kidney representation in STELLA [®]	128
62	Spleen representation in STELLA [®]	129
63	Brain representation in STELLA [®]	130

Figure		Page
64	Richly perfused tissue representation in STELLA [®]	131
65	Slowly perfused tissue representation in STELLA [®]	132
66	GI tract representation in STELLA [®]	133
67	Lung model in STELLA [®]	134
68	Liver IE and expanded models in STELLA [®]	137
69	GI model in STELLA [®]	140
70	Kidney IE and expanded models in STELLA [®]	142
71	Spleen IE and expanded models in STELLA [®]	145
72	Brain IE and expanded models in STELLA [®]	148
73	RPT IE and expanded models in STELLA [®]	151
74	SPT IE and expanded models in STELLA [®]	154
75	Index for the 24 rows	159
76	Liver, kidney, spleen, and brain subcompartments	163
77	Example used for eigenvalue analysis	171
78	Eigenstructure (using L2 norm)	172
79	Contributions of exponential terms and total concentration in kidney subcompartments	174
80	Comparison of subcompartments	175
81	Index showing which subcompartments correspond to which rows	176
82	Eigenstructure for $T_{ei}=0.05$	177
83	Eigenstructure for $T_{ei}=0.5$	178
84	Eigenstructure for $T_{ei}=5$	179

List of Tables

Table		Page
1	Physiological parameters for the PBPK model	45
2	Fractions of cardiac output	46
3	Organ volumes	46
4	Subcompartment volumes	47
5	Transport parameters needing range finding	49
6	Transport parameter values selected	49
7	Range finding results	88
8	Phase III physico-chemical properties simulations	111

List of Symbols

C_x	Concentration of nanoparticles in subcompartment ‘x’ (x1000 particles/liter)
K_m	Michaelis-Menten constant (in units of concentration, x1000 particles/liter)
$P_{t:b}$	Partition coefficient, ratio of tissue conc to blood conc (unitless)
Q_x	Blood flow rate for subcompartment ‘x’ (liters/hour)
$T_{b:t}$	Diffusion transfer coefficient, blood-to-tissue (x1000 particles/hour)
$T_{e:i}$	Diffusion transfer coefficient, extra-to-intracellular (x1000 particles/hour)
V_{\max}	Michaelis-Menten maximum rate of transport (x1000 particles/hour)
V_{\maxat}	Michaelis-Menten maximum rate of transport for active transport, extra- to intracellular direction (x1000 particles/hour)
$V_{\maxcmt1}$	Michaelis-Menten maximum rate of transport for carrier mediated transport, extra-to intracellular direction (x1000 particles/hour)
$V_{\maxcmt2}$	Michaelis-Menten maximum rate of transport for carrier mediated transport, intra-to extracellular direction (x1000 particles/hour)
V_x	Volume in subcompartment ‘x’ (liters)

List of Abbreviations

ADME	Absorption, Distribution, Metabolism, Excretion
AFIT	Air Force Institute of Technology
AFRL	Air Force Research Laboratory
ALV	Alveolar (region of the respiratory tract)
AM	Alveolar Macrophage
ATP	Adenosine Triphosphate
AUC	Area Under Curve
BBB	Blood-Brain Barrier
BE	Bioenvironmental Engineering
BPEF	Brain Paracellular Efficiency Factor
BW	Body Weight
cm	centimeter (10^{-2}m)
CNS	Central Nervous System
COPD	Chronic Obstructive Pulmonary Disease
CUEF	Cellular Uptake Efficiency Factor
CUSF	Cellular Uptake Shape Factor
DF	Deposition Fraction
GFR	Glomerular Filtration Rate
GI	Gastrointestinal
HA	Head-Airways (region of the respiratory tract)
KFEF	Kidney Filtration Efficiency Factor
LAF	Liver Accumulation Factor

MPS	Mononuclear Phagocytic System
μm	micron ($10^{-6}\text{m}=1000\text{ nm}$)
NIOSH	National Institute for Occupational Safety and Health
nm	nanometer (10^{-9}m)
NNI	National Nanotechnology Initiative
ODE	Ordinary Differential Equation
OLS	Ordinary Least Squares
OSHA	Occupational Safety and Health Administration
PBPK	Physiologically Based Pharmacokinetic
PCF	Phagocytosis Coating Factor
PEG	Polyethylene Glycol
PEL	Permissible Exposure Limit
PSF	Phagocytosis Size Factor
PTEF	Paracellular Transport Efficiency Factor
PTFE	Polytetrafluoroethylene
RES	Reticuloendothelial System
RPT	Richly Perfused Tissue
SCF	Surface Charge Factor
SPAF	Spleen Accumulation Factor
SPT	Slowly Perfused Tissue
TB	Tracheo-Bronchial (region of the respiratory tract)
TEF	Transcytosis Efficiency Factor
USAF	United States Air Force

PROVIDING A THEORETICAL BASIS FOR NANOTOXICITY RISK
ANALYSIS DEPARTING FROM TRADITIONAL PHYSIOLOGICALLY-BASED
PHARMACOKINETIC (PBPK) MODELING

I. Introduction

1.1 Overview

Nanotechnology is a growing field of science and manufacturing in which nanoparticles are exploited for their novel properties [28, 53, 1, 2, 3, 5]. *Engineered* nanoparticles, which are particulate structures less than 100 nanometers (nm) in size, lead to intriguing possibilities in consumer products, materials, and diagnostic/therapeutic medicine. Without a doubt, the rapid growth in the use of nanotechnology is likely to provide significant benefits to society, but increasing concern regarding potential adverse health effects of nanoparticles has driven considerable research worldwide.

In response to such concerns, the Clinton administration started the National Nanotechnology Initiative (NNI), designed to coordinate nanotechnology-related research across federal agencies and to create a strategic research plan to address the environmental and health implications of nanotechnology. Research funding has nearly tripled from \$464 million in 2001 to an estimated \$1.301 billion in 2006, largely due to stimulus from NNI [46]. An estimated \$29 billion in sales of nanotechnology products was projected for 2008, with the worldwide nanotechnology industry growing to an estimated \$1 trillion by 2015 [60]. With respect to the Department of Defense, the Air Force Research Laboratory (AFRL) has nanotechnology research and design emphasis in the following areas: energy, information, bio/nano, sensors, materials,

structures, and propulsion. Projects include: improving battery life, determining toxicity and biological interactions, nanocomposite materials, self-healing nanomaterials, and nanocoatings for fuel components [81].

This dissertation looks at existing literature, in order to develop a pharmacokinetic model representing theorized transport processes which explain nanoparticle kinetics and distribution within the body. Due to their small size, nanoparticles can pass between or through cells [54], allowing translocation to parts of the body not typically reachable by larger particles. The traditional pharmacokinetic modeling assumption of instantaneous equilibration, in which there is an instantaneous equilibration between blood and tissue within the capillary beds of the circulatory system, does not appear to apply to engineered nanoparticles, therefore warranting more rigorous modeling of the nanoparticle transport by including physico-chemical properties of engineered particles. Similarly, toxicological dose-response research on chemicals often relies on a metric of mass to represent dose, whereas physico-chemical properties must also be considered when dealing with nanoparticles.

1.2 Research Questions

Instantaneous equilibration between blood and tissue within the capillary beds of the circulatory system is a commonly used assumption for chemical models and presumably is not a good assumption for nanoparticle modeling. Instead, there are several known transport processes that apply to biological systems, many of which have not been extensively modeled in PBPK models. However, it is not known for certain which of these transport processes apply to nanoparticles. Therefore, the research questions posed as the basis for this dissertation are:

1. *For nanoparticle PBPK modeling, what are the implications of these different processes on tissue concentrations, as compared to an assumption of instant-*

neous equilibration?

2. *How can these implications guide the direction of nanotoxicity research, particularly in determining parameter values for transport processes elucidated to be important?*
3. *How will these findings suggest a possible new paradigm for nanoparticle risk analysis, particularly in the area of dose-response assessment?*

These three research questions are used as the basis for the dissertation and the three phases of research (i.e., Model Formulation, Inclusion of Physico-Chemical Properties, and Defining a New Paradigm for Risk Analysis) are specifically designed to provide answers to these questions. These answers are presented in Section 5.1 on page 121.

1.3 Assumptions

A goal of this research is to create a fully-functional, physiologically-accurate nanoparticle PBPK model which explores the impact of cellular transport processes on overall system behavior. Further goals include guiding future research and helping define a more appropriate approach to risk analysis for nanomaterials.

It is acknowledged here, and in the literature, that translocation rates and details on accumulation and retention in critical target sites are largely unknown [54]. With the considerable lack of data regarding nanoparticle biokinetics, several assumptions must first be made in order to enable this dissertation research. Note that a further discussion of assumptions is located in Appendix A on page 125. The key assumptions are:

1. Physiological parameters were estimated as best as possible, using the methodology to be described later in Section 2.3.1 on page 26. For example, parameters

such as organ volumes, blood flow rates, respiration rates, etc., are fairly well published, but other parameters such as the fraction of organ volume classified as extracellular or intracellular are not.

2. Model is not calibrated against in vitro or in vivo data. A motivating factor driving this research is the fact that such data are limited and, therefore, a goal of this dissertation is to encourage research toward quantifying unknown parameters governing nanoparticle biokinetics.
3. Initial assumption is that the same transport processes apply to all organs and mathematical representations of the transport processes are identical across the organs. However, the second phase of research explores the effects of nanoparticle physico-chemical properties and these organ-specific characteristics are used to modify the mathematical representations.
4. High concentrations do not necessarily equate to adverse effects. This research does not address the toxic effects of specific nanomaterials as that is the focus of in vitro research.

II. Literature Review

2.1 Nanotoxicology

The primary motivation behind this proposed dissertation research is founded on the widely accepted belief that nanoparticles present unique exposure risks as compared to larger sized particles of the same material. Although the toxicology of a base material may be thoroughly defined, the toxicity of the same material when in nano size may be very different [57]. In general, it is believed that physico-chemical properties of nanoparticles, such as size, shape, surface charge, solubility, surface area, etc., influence both the disposition of particles in the lungs and the biological responses [47].

For example, although larger particles of gold are relatively inert, nano-sized particles of gold can elicit a biological response [54] and can be fairly toxic to tissue. Greater surface area per unit mass renders nanoparticles more active biologically than larger-sized particles of the same chemistry [57]. This is because smaller particles occupy less volume, resulting in more particles in a given volume and greater surface area per unit mass [54]. Smaller particles have a greater fraction of atoms at the surface, leading to increased surface reactivity [31]. In addition, surface modifications of nanoparticles can significantly alter their properties, with distribution of nanoparticles strongly depends on surface characteristics [57]. It is important to note that agglomeration and aggregation may occur during handling of bulk nanomaterials, thus increasing the effective size of the material and thereby potentially affecting the nanotoxicity.

Although the toxicological effects of engineered nanoparticles on the human body are not fully understood, existing research on combustion-derived nanoparticles offers considerable insight into possible effects. This includes generation of free radicals and

oxidative stress, leading to inflammation and possible cardiovascular disease, asthma, chronic obstructive pulmonary disease (COPD), scarring, and cancer [77]. Fibrosis in the alveolar interstitium is also possible [69]. Figure 1 shows the potential exposure pathways and health consequences of nanoparticle exposures, due to inhalational exposure.

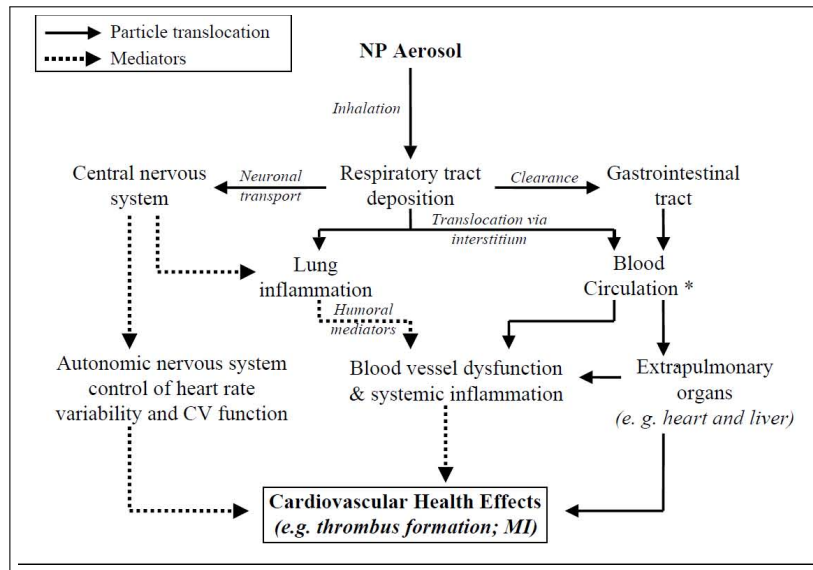


Figure 1. Potential pathways, consequences of nanoparticle exposures (from Oberdörster, et al.) [58]

Nanoparticles also present additional exposure and uptake pathways that present challenges in health risk assessments. For example, once nanoparticles are deposited in the alveolar region (i.e., deep lung), they appear to be able to translocate out of the lungs and reach other target organs in the body [57]. Specifically, nanoparticles penetrate the alveolar epithelial lining of the deep lung and subsequently enter the lung interstitium to a greater extent than an equal mass of larger particles [47]. Also, nanoparticles have a propensity to cross cell barriers, enter cells, and interact with subcellular structures [58], thus presenting new interactions not necessarily seen for larger particles. The ability to reach new regions, unhindered by natural blocking mechanisms, makes nanoparticles attractive in medical applications [31], but these

same abilities present challenges when trying to assess risk of exposure to nanomaterials in the occupational setting.

Due to their size, very low mass concentrations of nanoparticles in air can represent extremely high particle number concentrations. Extraordinarily high number concentrations (number of particles per given mass) can be of toxicological significance as evidence suggests that high number concentrations inhaled can overwhelm the clearance mechanism of phagocytosis in the deep lung, thus allowing more nanoparticles to translocate out of the lungs and reach various toxic endpoints in the human body [11, 79]. This overloading phenomenon and potential systemic translocation present significant challenges in occupational risk exposure, whereas larger particles tend to be cleared from or remain sequestered in the deep lungs. Note also that the relatively low mass associated with nanoparticles suggests that number concentration (i.e., number of particles per unit volume) is a more relevant descriptor of exposure than traditional mass concentration. Besides number concentration, the surface area of a nanoparticle may be a better predictor (than mass), due to the higher biologic activity associated with higher surface area.

In general, the lack of toxicological data presents a challenge in performing risk assessments for exposures to nanoparticles. Most nanotoxicology research to date has been performed *in vitro*, i.e., in cell cultures. The challenge, therefore, is extrapolating these *in vitro* findings to the *in vivo* environment (i.e., inside the living organism), especially to the human scale. The incomplete data set, and sometimes inconclusive results, have led to the inability to set nanoparticle-specific exposure limits.

2.1.1 Absorption, Distribution, Metabolism, Excretion (ADME).

Very few pharmacokinetic studies, which detail the rate and extent of absorption, distribution, metabolism, and excretion (ADME), have been performed on nanoma-

terials. Figure 2 shows confirmed and potential exposure routes, including inhalation, ingestion, and dermal.

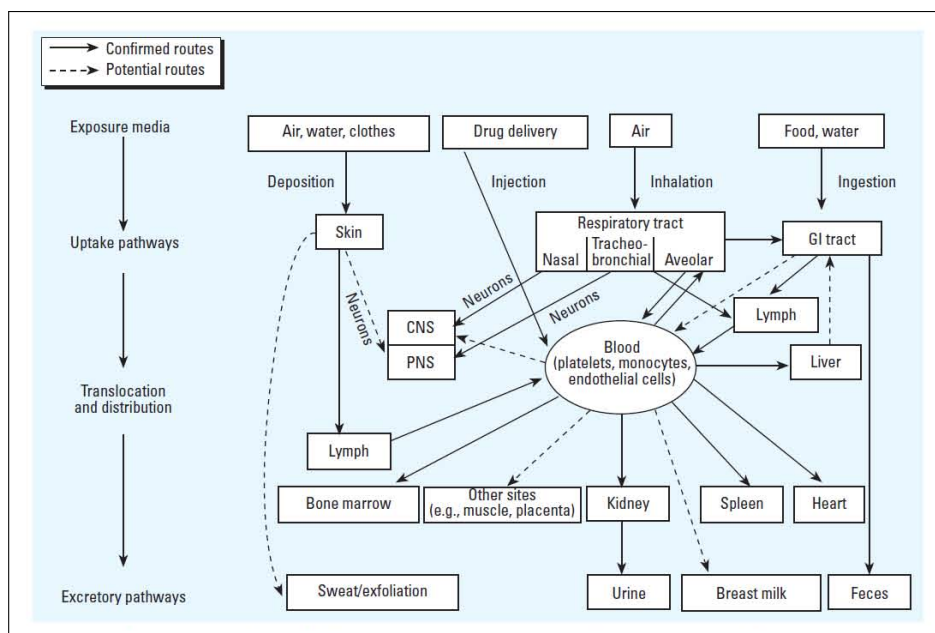


Figure 2. Confirmed and potential routes for nanoparticle exposures (from Oberdörster et al. and Environmental Health Perspectives) [57]

The lack of studies has left many unanswered questions, including one posed by Riviere and Tran in their article on pharmacokinetics of nanomaterials which asks whether nanoparticle movement follows traditional thinking of diffusion as the primary mode of chemical movement [64]. A primary objective of this dissertation research is to present a pharmacokinetic model, which begins to explore ADME by including cellular transport processes not typically included in such models.

2.1.1.1 Absorption.

Absorption is the generic term used to describe how toxicants initially enter the mammalian system by crossing tissue membranes and entering the bloodstream at several sites including the gastrointestinal tract, lungs, and skin [34]. In most occupational settings, the primary route of exposure to nanoparticles is likely to be

inhalation, and therefore the primary site of absorption is the lungs. Ingestion of nanoparticles is possible from eating or drinking contaminated items and from clearance due to phagocytosis with subsequent swallowing.

Dermal absorption of nanoparticles is theorized as being possible, although its likelihood is debatable. There is conflicting evidence on whether nanoparticles effectively penetrate the skin and can enter circulation. The skin provides a large surface area, approximately 1.5 m^2 for humans, and in theory, presents a large potential route of exposure. It is comprised of the epidermis, dermis, and subcutaneous layers. The outer portion of the epidermis, called the stratum corneum, forms a $10 \text{ }\mu\text{m}$ thick keratinized layer of dead cells which is normally considered a fairly tight barrier against nanoparticle penetration.

Tinkle, et al., concluded that risk of dermal translocation is minimal to non-existent, except in the event of broken skin and where skin flexing occurs [75]. Penetration at the hair follicles is another possible pathway [8]. Evidence suggests that if dermal penetration does occur, such as through compromised skin, nanoparticles appear to be able to translocate via lymphatic uptake to regional lymph nodes, with subsequent entrance into the blood circulation system.

For inhaled particles, larger particles tend to be deposited further up in the respiratory tract, due to gravitational settling, impaction, and interception. The nasal and upper airway regions present a fairly robust barrier with epithelial tissue covered in a layer of thick mucus. Particles smaller than $10 \text{ }\mu\text{m}$ can reach the gas exchange surfaces (alveoli), where Brownian motion leads to deposition [8]. Very small particles ($< 1 \text{ }\mu\text{m}$) can be exhaled, thereby reducing deep lung deposition [87].

2.1.1.2 Distribution.

After the toxicant is absorbed into the blood, distribution to tissues throughout the body normally occurs fairly rapidly. Rate of distribution is determined primarily by blood flow and rate of diffusion out of capillaries and into organs and tissue [34]. Distribution to several organs may occur, via multiple means of translocation (e.g., circulatory system, lymphatic system, neurons). Nanoparticles may have unique distribution properties as research indicates that regardless of exposure route, the body distribution of nanoparticles is highly dependent on the surface characteristics and size of the particles [27].

2.1.1.3 Metabolism.

Although metabolism (biotransformation) commonly occurs for exposures to foreign chemicals (xenobiotics), there is no evidence in literature of biotransformation of nanoparticles. Therefore, this dissertation research will not cover metabolism.

2.1.1.4 Excretion.

Several clearance mechanisms exist to eliminate toxicants, including nanoparticles, from the body. Exhalation, urine, and feces are the primary modes of excretion. Exhalation of nanoparticles occurs as not all inhaled particles are deposited within the respiratory tract. Urine is produced during the filtration of blood as it travels through the kidney. Nanoparticles can also travel through the gastrointestinal (GI) tract following digestion to exit the body as feces. In addition, the liver can pass foreign materials into bile which exits to the GI tract for possible excretion with feces. The liver can effectively remove foreign materials from both systemic circulation and portal circulation (blood flow from the GI tract). Bodily fluids, such as sweat, saliva, tears, and breast milk are other possible means of secreting toxicants [34], but are

not included in this dissertation.

2.1.2 Organs of Concern.

2.1.2.1 Respiratory Tract.

Research indicates significant differences exist between the fate of nano-sized particles versus larger particles, with respect to deposition and clearance in the respiratory tract. In general, smaller particles travel deeper into the respiratory tract where they can undergo deposition. For example, particles of diameter 1 μm and smaller, which includes nanoparticles, can reach the deep lung where alveolar sacs reside [34].

The primary means of deposition of nanoparticles in the respiratory tract is Brownian motion (diffusion), which dominates at smaller diameters. Nanoparticles typically behave much like gas molecules, moving randomly by Brownian motion [69]. Inertial impaction, gravitational settling, and interception do not contribute significantly to nanoparticle deposition, due to the small particle mass and momentum. It should be noted that these statements pertain to singlet particles (monodisperse) and the existence of agglomerates and aggregates will lead to disposition following larger particle size behavior. Note also that electrostatic precipitation will occur only with nanoparticles carrying significant electrical charge relative to its surroundings [57].

Evidence suggests that a high fraction of inhaled nanoparticles can deposit in the tracheobronchial and pulmonary regions of the lung, with the deposition being greater than that for inhalation of equivalent amounts of coarse or fine particles. Also, high deposition in one region of the respiratory tract does not necessarily imply a corresponding high dose.

Regarding the fate of nanoparticles in the respiratory tract, several clearance mechanisms are possible. First, a portion of inhaled particles may be exhaled. Second, deposited particles can be captured in the mucus which lines the conducting zone of

the respiratory tract. Particles captured in the mucus layer of the airways can be cleared via the mucociliary escalator, where mucus is moved along at a velocity of 1-2 cm/min by cilia projecting from the top of epithelial cells [16]. Third, particles reaching the deep lung (alveolar space) can be phagocytized and subsequently cleared by the mucociliary escalator.

Additionally, particles can remain sequestered in the lungs with some crossing the lung epithelium into the interstitial region. The alveolar wall (epithelium) is only one cell thick, leaving only a thin barrier between inhaled nanoparticles and the bloodstream, thus presenting a pathway into the interstitial region for nano-sized particles. Results of several studies have shown that nanoparticles deposited in the respiratory tract gain access to epithelial cells and interstitial fluid [57]. Known as ‘interstitial translocation’, it is caused by nanoparticles escaping phagocytosis due to either their small size [57] or overloading of the alveolar macrophage capacity to phagocytize particles.

Several studies have demonstrated this translocation capability of nanoparticles, including a study using ultrafine particles of polytetrafluoroethylene (PTFE) which showed that shortly after a 15-minute exposure, the fluorine-containing particles were found in interstitial sites of the conducting airways [57]. Once in the interstitium, translocation away from the respiratory tract and into the circulatory or lymphatic systems is possible [8]. Oberdörster et al., demonstrated how inhaled ^{13}C particles (25 nm) were rapidly cleared from rat lungs within 24 hours and translocated to other organs, including the liver and spleen [56, 47].

Note that it is likely that alveolar translocation is dependent on particle size and surface chemistry [57]. It is yet to be determined the exact mechanisms by which ultrafines penetrate cellular membranes. Therefore, the exact mechanism of penetration through pulmonary tissue leading into capillaries is undetermined.

Many chemical PBPK models use a simplifying assumption for the lungs in which the toxicant in the alveolar space is assumed to equilibrate very rapidly with capillary blood. This instantaneous equilibration is represented using a partition coefficient. For nanoparticles, it is likely more appropriate to expand the model to include deposition, macrophage/mucociliary escalator clearance, and translocation away from the interstitium.

2.1.2.2 Gastrointestinal Tract.

The gastrointestinal (GI) tract presents a potential exposure pathway, following ingestion of food or water containing nanoparticles, or due to clearance of inhaled nanoparticles from the respiratory tract by the mucociliary escalator. Several studies conclude that nanoparticles can be efficiently absorbed through the GI tract, with translocation into the lymphatic and circulatory systems [31]. For unintentional exposures, it is believed that most nanoparticles simply pass thru the gastrointestinal tract and are rapidly eliminated [57].

If not rapidly eliminated, products of digestion can be absorbed into blood capillaries. Absorption is most likely due to passive diffusion, with small particles being more readily absorbed into blood than large particles [34]. Jani, et al., found a size-dependent uptake of polystyrene particles for the range 50-3000 nm through the GI mucosa [30].

It should be noted that these products do not enter general circulation directly. Instead, the blood first travels from capillaries of the gastrointestinal tract to the liver via the hepatic portal vein, where it then enters capillaries in the liver for possible biotransformation or capture. Note that for nanoparticles, biotransformation (metabolism) is not believed to occur.

2.1.2.3 Liver.

The structure of the liver is comprised of liver cells, called hepatocytes, arranged in thin layers in a radial pattern around a central vein. Hexagonal blocks of such layers are called lobules. Spaces, called sinusoids, exist between the layers of hepatocytes and are supplied by two sources of blood. First, the liver is supplied by arterial blood from the hepatic artery. Second, the liver is supplied by the hepatic portal vein, which transports blood from the gastrointestinal tract and spleen. This physiological feature prevents contaminants from entering systemic circulation directly and is called the “first-pass effect”. Combined, these two supplies carry approximately 25% of systemic circulation to the liver at any given time [18]. See Figure 3.

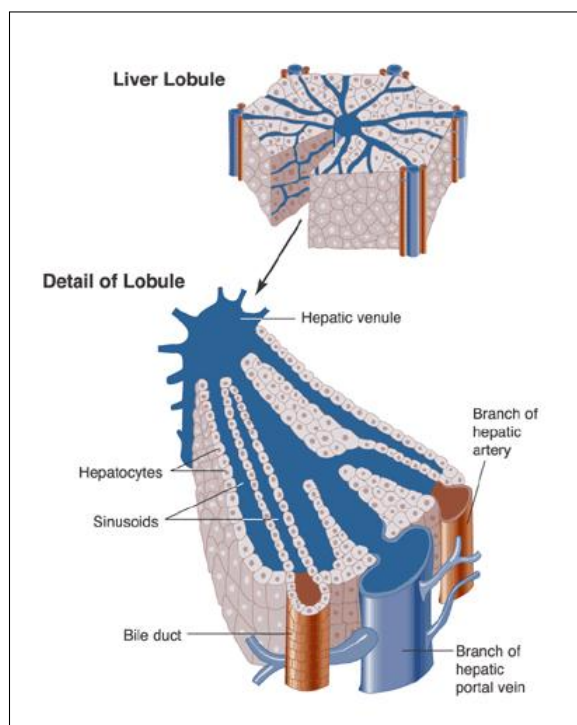


Figure 3. Cross-Sectional View of Liver Lobule (*from wikipedia.org*)

It should be noted that the liver is more commonly known for its ability to metabolize small molecules, using various enzymes resident in the liver. Although nanoparticles do not appear to undergo such metabolism, the liver is part of the reticuloen-

dothelial system (RES) and has a large number of phagocytic cells to remove foreign material. Phagocytic cells in the liver, called Kupffer cells, can trap foreign material passing by engulfment.

In addition, the endothelial cells lining the sinusoids have small pores called fenestrae, typically 100-150 nm in diameter, which allow passage of nanoparticles to parenchymal cells (hepatocytes), where endocytic processes occur for uptake of smaller particles [20]. Solutes (and foreign material) in the blood pass between endothelial cells of the walls lining the sinusoids, beyond which are the hepatocytes. After interaction with hepatocytes, blood exits through hepatic vein and out of the liver. In addition, the liver also produces bile which is a clearance mechanism for toxicants [16]. It is stored in the gallbladder prior to discharge to the duodenum (upper small intestine), where it can then be excreted along with feces. Potential damage to the liver includes lesions, such as inflammation or necrosis (i.e., localized death of cells) [54].

2.1.2.4 Kidneys.

The kidneys are a major filtering system to eliminate toxicants flowing in blood and excrete them via urine. Like the liver, they receive a considerable amount of cardiac output (approximately 25%), or approximately 1.2-1.3 liters of blood per minute. The nephron is the functional unit of the kidney, each of which contains glomeruli, which are small tufts of blood capillaries. These capillaries have small fenestrations which allow glomerular filtration of blood with transit across Bowman's Capsule. See Figure 4 on the following page. Once across, the fluid (e.g., water and electrolytes) is either reabsorbed into blood or excreted. A particle diameter <5.5 nm is the threshold for glomerular filtration, hence the possible removal of nanoparticles through excretion to urine [43].

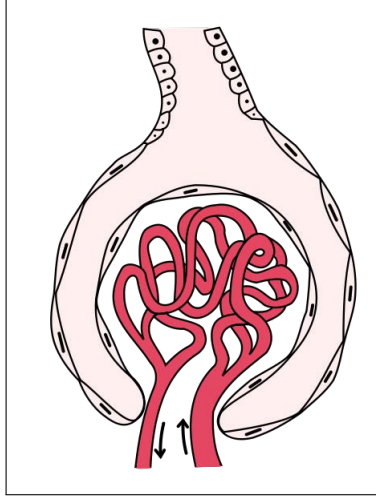


Figure 4. Kidney glomerulus, surrounded by Bowman's Capsule (*from wikipedia.org*)

2.1.2.5 Spleen.

The spleen is the largest lymphatic organ in the body and has important immunological and filtering functions [48]. It destroys old red blood cells while also serving as a blood reservoir and is divided into segments, each having its own separate blood supply. Each segment contains red and white pulp, with white pulp being lymphatic tissue and the red pulp contains phagocytic cells [48]. It is an important part of the reticuloendothelial system, with a large number of phagocytic cells available to remove foreign material.

The spleen receives arterial blood from the splenic artery, which flows into splenic arterioles (surrounded by white pulp) and then capillaries. Instead of flowing directly into venules, these capillaries first empty into the red pulp. From there, the blood flows into venous sinusoids. To leave the sinusoids, blood elements (including particles) must pass through openings in the sinusoids, called interendothelial slits (or fenestrations). Therefore, it is believed that red pulp provides a filtering function for the spleen with clearance (i.e., capture) of larger particles (>250 nm dia.) [18]. Once through the interendothelial slits, blood enters venous flow by passing through

through the splenic vein and reaching the portal vein (i.e., portal circulation leading to the liver).

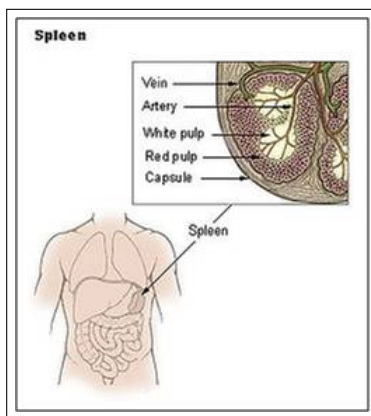


Figure 5. Spleen anatomy (*from wikipedia.org*)

2.1.2.6 Brain.

The brain is of special interest to researchers, especially with nanoparticles being shown to induce the production of reactive oxygen species and oxidative stress, both of which have been linked to neurodegenerative diseases such as Parkinson's and Alzheimer's [32, 6]. Besides possible harmful effects, nanoparticles can be used for beneficial purposes, such as carriers of pharmaceuticals. Two goals of pharmaceutical companies are to either avoid opsonization of nanoparticles by covering them with hydrophilic polymer coatings (e.g., PEG) or by attaching specific ligands for brain targeting [59, 29].

The phagocytic cells, such as those in the liver and spleen, help limit the exposure of nanoparticles at the cerebrovasculature as they can remove a significant percentage of nanoparticles [45]. But once nanoparticles reach the brain, normally physiologic processes are in place which effectively protect the brain from foreign material, including nanoparticles. The blood-brain barrier (BBB) serves to protect neurons from systemic circulation agents/toxins by forming a very tight capillary barrier (i.e., very

tight junctions between endothelial cells lining the blood capillaries of the brain). It forms a physical barrier with a negative electrostatic charge between the blood vessels and brain, which selectively restricts access of certain substances [8].

However, evidence suggests that nanoparticles may be able to overcome the BBB due to their small size. Integrity of the BBB defense mechanism can also be compromised by specific circulatory diseases (e.g., hypertension) and brain inflammation which increases the likelihood of toxicants, including nanoparticles, crossing over the barrier.

In general, more specialized transport mechanisms are necessary to effectively overcome the tight junctions between endothelial cells lining the blood vessels of the brain. Such mechanisms include active transport and carrier-mediated transport [16, 27]. Kreuter’s research on using nanoparticles to deliver drugs through the BBB describes the most likely transport mechanism as being endocytosis by the endothelial cells lining the brain blood capillaries, with diffusion into the brain and subsequent drug release within the cells [35].

Besides crossing the fairly tight barrier presented by the BBB, another route into the brain exists through the olfactory nerve pathway following inhalation [23]. Research indicates that the olfactory nerve pathway (nose-to-brain) should be considered a route of entry to the central nervous system (CNS) of humans for inhalational exposures to nanoparticles. Oberdörster, et al. concluded that the CNS can be targeted by ultrafine particles after deposition on the olfactory mucosa in the nasopharyngeal region, with subsequent translocation via the olfactory nerve to the olfactory bulb within the brain [57]. Their research demonstrated that inhalation of carbon-13 (^{13}C) ultrafine particles resulted in significant increase in ^{13}C in the olfactory bulb over seven days [55]. This translocation pathway involving neuronal axons does not apply to larger particles [57]. Remarkably, this pathway was first described in 1941

by Bodian and Howe, whose research on the 30 nm polio virus and exposures to primates revealed that the olfactory nerve and bulbs are routes of entry to the CNS for intranasal instillation [58].

2.2 Cellular Transport

There are several known cellular transport processes that apply to biological systems, many of which have not been extensively modeled in PBPK models. Three such examples include diffusion, active transport, and carrier mediated transport, which have been cited in literature as possible transport processes for nanoparticles [41].

Although it is not known for certain which of these transport processes apply to nanoparticles, there is value in beginning the modeling of such processes as it may improve our understanding of the toxicokinetics of nanoparticles [84]. Therefore, this work focuses on developing mathematical representations of these three cellular transport processes for inclusion in a general nanoparticle PBPK model for comparison against the traditional assumption of instantaneous equilibration. Doing so will help guide future research and perhaps lead to the enhancement of nanoparticle risk assessment by looking beyond traditional PBPK assumptions.

The exact mechanisms for transport of nanoparticles across cellular membranes are debatable, but the two general categories of cellular transport are passive and active transport. Notable processes under the passive transport family are diffusion and carrier mediated transport. Although active transport also relies on “carriers”, we recognize active transport as a separate process as it is a uni-directional process with an ability to concentrate a solute against the concentration gradient. These three transport processes (diffusion, active transport, and carrier mediated transport) are the focus of this research.

2.2.1 Simple Diffusion.

The first cellular transport process included as a possible explanation for the movement of nanoparticles is diffusion. Simple diffusion is based on Fick's First Law (of Diffusion) and is dependent on the concentration gradient, such as that between two compartments. Net diffusion will cease when the concentration gradient=0. Flow between the compartments is bi-directional.

For the mathematical representation, a transfer coefficient, T , is used to characterize the rate of transfer of nanoparticles between compartments. The transfer coefficient, T , represents the $P \times A$ product (permeation constant \times surface area) that would be found in in vitro research, but is unknown in this case.

Equation 1 shows a hypothesized mathematical representation for diffusion, with a partition coefficient $P_{2:1}$ defined in terms of concentrations C_1 and C_2 . The partition coefficient describes the distribution (ratio of the concentrations) of a chemical, compound, etc., in two phases/media when at equilibrium. Simple diffusion includes paracellular diffusion (permeating the cell membrane by traveling through aqueous pores between cells) and transcellular diffusion (traveling through the cells themselves) [34].

$$\text{Diffusion Transport Rate} = T \times \left(C_1 - \frac{C_2}{P_{2:1}} \right) \text{ (\#particles/hour)} \quad (1)$$

where

T = transfer coefficient (liters/hour)

C_1 = concentration in subcompartment 1 (#particles/liter)

C_2 = concentration in subcompartment 2 (#particles/liter)

$P_{2:1}$ = partition coefficient from 2:1 (unitless)

2.2.2 Active Transport.

Active transport relies on specific protein molecules to serve as carriers, allowing substances to move across the cell membrane. The protein molecules are selective in which substances can be carried across the cellular membrane. Transport occurs independent of the concentration gradient, thus allowing a substance to move from regions of lower concentration to higher concentration [80]. The material that is transported binds to the carrier molecule for transport into or out of the cell. As travel across the membrane is against the concentration gradient, the cell must expend energy that is usually derived from adenosine triphosphate (ATP). The energy is necessary as the protein molecule changes shape in order to move the substance. An example of active transport is the sodium-potassium pump, which facilitates movement of sodium and potassium across cellular membranes.

As active transport relies on the availability of a protein molecule carrier to transport a substance across the cellular membrane, it is assumed that loading up of carriers is saturable. This saturable rate of transport is modeled here using Michaelis-Menten kinetics, which is more commonly seen in metabolism processes for chemicals in the liver. By convention, Michaelis-Menten kinetics are traditionally represented using V_{\max} and K_m . V_{\max} represents the maximum rate of transport (i.e., at full saturation of the carrier), while the Michaelis-Menten constant, K_m , represents the concentration

of nanoparticles prevailing when the transport rate is half of V_{\max} (i.e., 50% saturation of the transporter protein). The general equation representing active transport, assuming Michaelis-Menten kinetics, is shown in Equation 2.

$$\text{Active Transport Rate} = \frac{V_{\max} \cdot C}{K_m + C} \text{ (#particles/hour)} \quad (2)$$

where

$$V_{\max} = \text{max rate of transport (\#particles/hour)}$$

$$C = \text{concentration (\#particles/liter)}$$

$$K_m = \text{Michaelis-Menten constant (\#particles/liter)}$$

At low and high concentrations, Equation 2 can be simplified as shown in Equation 3. More specifically, at low concentrations the rate of transport behaves linearly with respect to concentration since V_{\max}/K_m is a constant. At higher concentrations, this rate saturates and is approximated by the constant, V_{\max} .

$$\text{Active Transport Rate} \approx \begin{cases} \frac{V_{\max} \cdot C}{K_m}, & C \ll K_m \\ V_{\max}, & K_m \ll C \end{cases} \quad (3)$$

2.2.3 Carrier Mediated Transport.

Similar to active transport, carrier mediated transport also relies on protein carriers to transport a material across the cell membrane. These carriers can transport ions and uncharged solutes, with some carriers transport single solutes while others can transport 2-3 solutes at a time (single substrate and multiple substrate carriers).

Carrier-mediated transport is typically found when a molecule is too large to dif-

fuse through pores of the cell membrane or low lipid solubility and an electrical charge inhibits movement [33]. Carrier-mediated transport is also assumed to be saturable process. Assuming carrier mediated transport can occur in either direction and that there are two separate carriers involved, two sets of Michaelis-Menten constants are used to represent the saturable rates. See Equation 4.

$$\text{Carrier Mediated Transport Rate} = \frac{V_{\max 1} \cdot C_1}{K_{m1} + C_1} - \frac{V_{\max 2} \cdot C_2}{K_{m2} + C_2} \text{ (#particles/hour)} \quad (4)$$

where

$V_{\max 1}$ = max rate of transport, from 1 to 2 (#particles/hour)

C_1 = concentration in subcompartment 1 (#particles/liter)

K_{m1} = Michaelis-Menten constant, from 1 to 2 (#particles/liter)

$V_{\max 2}$ = max rate of transport, from 2 to 1 (#particles/hour)

C_2 = concentration in subcompartment 2 (#particles/liter)

K_{m2} = Michaelis-Menten constant, from 2 to 1 (#particles/liter)

2.2.4 Phagocytosis.

Phagocytosis is a clearance mechanism in which large particles and microorganisms are engulfed by the cell membrane, through formation of large vacuoles (aka vesicles) which allow entry into the cell. Initially, foreign particles must bind to receptors on the surface of the phagocyte, subsequently triggering a process in which pseudopods extend outward and around the particles to form vacuoles. These vacuoles, also known as phagosomes, are generally >250 nm in diameter [1]. Nicknamed “cellular eating”, phagocytosis is the most prevalent clearance mechanism for deposited

particles (fine and coarse particles) in the alveolar region where it is performed by alveolar macrophages [57]. Another example of phagocytosis is the capture of invading foreign cells (e.g., bacteria) by white blood cells.

Phagocytosis is mainly carried out by specialized cells, known as phagocytes. The reticuloendothelial system (RES), which is also known as the mononuclear phagocytic system (MPS), is a group of mononuclear cells originating from the bone marrow which perform phagocytosis and remove small foreign particles from blood. Such cells are found throughout the body, but the principal organs where macrophages are found are the lungs, spleen, liver, and lymph nodes [18]. Lockman, et al., cites that a large portion (80-85%) of nanoparticles are removed from vascular space by such cells [45]. In mammals, this includes three classes of white blood cells: neutrophil granulocytes (i.e., neutrophils), dendritic cells, and macrophages, of which the latter are most common [1]. Neutrophils are the most abundant type of white blood cells in humans. They are normally found in the blood stream, but can also concentrate at sites of acute inflammation during chemotaxis.

However, the efficacy of phagocytosis of nanoparticles is affected by particle size. For example, human alveolar macrophages are typically 14-21 μm in diameter and are most effective at engulfing particles of comparable size. Particles that are much larger or smaller may not be effectively engulfed. Phagocytosis itself occurs within 6-12 hours after deposition, but actual clearance via the mucociliary escalator occurs much slower, with retention half-times of solid particles in the alveolar region of about 70 days in rats and up to 700 days in humans [57]. This longer retention time is due to the dependence on random migration for phagocytized material to reach the mucociliary escalator, which extends down to only the terminal bronchioli [37].

2.3 Physiologically-Based Pharmacokinetic Modeling

Physiologically-based pharmacokinetic (PBPK) modeling, which has roots dating back to 1924, has been a critical tool to both the pharmaceutical and toxicokinetic communities. As in vivo research is very costly and time-consuming, physiologically-based pharmacokinetic (PBPK) modeling is a valuable tool for exposure limit determination. It describes the time-course behavior of chemicals based on a mathematical model that mirrors the physiological structure of the body[63].

PBPK models offer the ability to estimate chemical concentrations in specific organs or tissue by mechanistically considering whole tissue systems linked together dynamically by blood flow [68]. The body is treated as parallel compartments representing organs or tissues, with each compartment characterized by appropriate physiological, physico-chemical, and biochemical parameters. Compartments can represent single organs or can represent a family of tissues or organs. Tissues are consolidated into a single compartment whenever feasible, unless the physiological, physico-chemical or biochemical parameters have noticeably different effects on the chemical uptake and disposition [39]. Examples of compartments used in PBPK models includes: adipose tissue, liver, brain, gastrointestinal tract, kidney, and lung.

Each tissue compartment is typically described with a mass balance ordinary differential equation (ODE) in time which describes the change in the amount of the chemical over time, typically in units of mass per time or number of particles per time, in the case of nanoparticles. The general form of an ordinary differential equation describing a compartment shows that the accumulation (or change in amount per unit time) in any compartment is the sum of all input rates minus the sum of all output rates. See Equation 5 on the following page. In addition, mass balance must be maintained throughout the model, e.g., total blood flow (cardiac output) should equal the sum of blood flows to the various compartments. The mass balance

differential equations, which serve as a mathematical representation of the body, can be numerically integrated to calculate the amount of contaminant in a tissue or organ (i.e., compartment).

$$\text{Accumulation} = \text{Rate of Transfer In} - \text{Rate of Transfer Out}$$

$$\Rightarrow \frac{d(\text{Amount})}{dt} = \sum Q_{\text{in}} C_{\text{in}} - \sum Q_{\text{out}} C_{\text{out}} \quad (\text{mass/time or } \# \text{ particles/time}) \quad (5)$$

In the absence of full data sets, PBPK models are useful as they can be used for extrapolations within a species or even between species. Within a species, the PBPK model can be combined with a limited set of experimental data to predict the remainder of the concentration profile for a chemical exposure. Scaling of parameters can also be used to extrapolate between species and is best accomplished by using published data (for tissue volumes, flow rates, other physiological constants, etc.). PBPK serves as an effective tool to leverage both dose-response and mechanistic data to more accurately predict human risk [12].

2.3.1 Parameterizing.

Model parameterization refers to establishing plausible physiological, physico-chemical, and biochemical parameters necessary for use in the model equations [39]. Physiological properties include: body weight, organ weight, fractions of the body allocated to each compartment, tissue blood flow (i.e, blood flow to and from tissue), cardiac output, volume of tissues, and alveolar ventilation rate [15, 62]. Actual values should be used whenever possible, but in the absence of such published data, parameter values can often be scaled using conversion factors (multipliers) from various

published research efforts.

2.3.2 Traditional Assumptions of PBPK.

Many articles featuring PBPK modeling have appeared in literature [4, 9, 13, 14] and perhaps it was the Ramsey/Andersen model for styrene in 1984 which re-popularized the use of PBPK models for toxicokinetics and pharmacology [61]. Such models often include what might be referred to as the “traditional” assumption of instantaneous equilibration between tissue and tissue blood of an organ. This traditional assumption is commonly used to describe pharmacokinetic behavior of volatile organic chemicals in tissue. However, the assumption may not be sufficient to describe nanoparticle time-course behavior as there are other physico-chemical properties of nanoparticles (e.g., size, shape, surface area, surface charge) that likely cause a fundamental difference in behavior. In general, particles are known for being retained in tissue, which is a property of potential toxicological significance [62]. In other words, nanoparticles are different than molecules and this likely warrants a departure from traditional PBPK modeling techniques.

Part of this assumption is the use of partition coefficients, which represent the relative distribution of the chemical between two phases at equilibrium [39]. Throughout many models, it is assumed that instantaneous venous equilibration exists which allows the use of partition coefficients to describe the relationship between concentrations in the compartment to the venous blood flowing out of the compartment. Whenever possible, partition coefficients should be experimentally determined [65]. Figure 6 on the next page shows the calculation of concentration in venous blood C_v using the partition coefficient P .

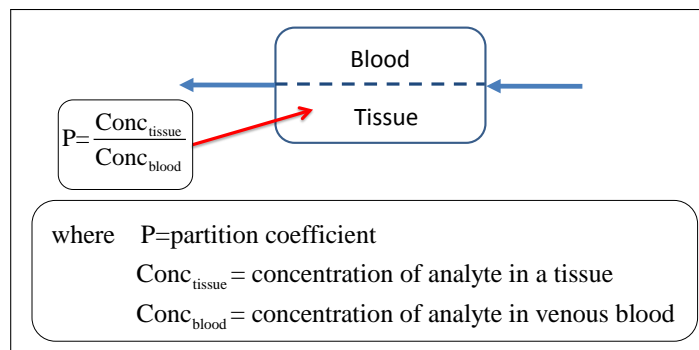


Figure 6. Tissue-to-blood partition coefficient

2.4 Current State of Nano Risk Assessment

“It is neither feasible nor sensible to conduct safety evaluations for all nanomaterials in current or future production; therefore, a risk assessment paradigm should be flexible and based on current knowledge of similar materials.”

- Igor Linkov, et al. [44]

2.4.1 Risk Assessment Frameworks.

Currently, there is no comprehensive risk assessment framework for nanomaterials, primarily due to the lack of toxicologic data on engineered nanoparticles [57]. In addition, there is a lack of adequate information describing the relationships between external exposure, disposition, and internal (target organ) dose. More information is necessary about characteristics of barriers to nanoparticles reaching target tissue (e.g., respiratory tract, skin, gut, and blood-brain barrier) and the kinetics for uptake, transport, and clearance of nanoparticles [44]. Beyond toxicological aspects, more information is also necessary on the plausibility of exposures (i.e., real-world exposure concentrations) [44].

The lack of such data prevents the National Institute for Occupational Safety and Health (NIOSH), which is responsible for conducting research and making recommendations to the Occupational Safety and Health Administration (OSHA) and other regulatory agencies, employers, workers, and the general public [52], from mak-

ing recommendations for exposure limits for engineered nanomaterials. In addition, OSHA itself does not have a permissible exposure limit (PEL) specific to engineered nanomaterials.

The current risk assessment paradigm generally involves toxicologic testing as the basis for addressing potential risk. Relying on this paradigm, it could take decades before a thorough data set exists, due to the thousands of nanoparticle variants possible as they are engineered to attain very specific properties.

In the absence of exposure limits, emphasis has been placed on determining occupational safety and health best practices to protect workers during production, handling, and use of nanomaterials. NIOSH recommends that workplaces implement *risk management programs* to emphasize such best practices. Risk management is an integral part of an overall occupational safety and health program for workplaces producing or using nanomaterials. A necessary part of any risk management program is to implement the hierarchy of controls [51], which is: 1) elimination 2) substitution 3) engineering 4) administrative 5) personal protective equipment

Due to the differences presented by engineered nanoparticles, coupled with the rapidly expanding nanotechnology field as a whole, a strategic plan has been developed by NIOSH to address data gaps. This plan is designed to guide their research on occupational safety and health concerns related to nanotechnology and includes 10 critical topic areas, with one of them being “risk assessment” [51].

In the NIOSH plan, the first goal regarding risk assessment focuses on utilizing existing exposure-response data for ultrafines to identify potential hazards and assess potential risks of occupational exposures to nanomaterials. Ultrafines (<100 nm) include such particles as coal dust, welding fumes, combustion byproducts, etc. Much can be learned from legacy data, but note that these are not *engineered* particles (i.e., not intentionally produced) and so they may exclude the physico-chemical

properties driving the unique toxicological behavior. Another difference between ultrafines and engineered nanoparticles is that ultrafines are *polydisperse* (i.e., of many sizes), whereas manufacturers of engineered nanoparticles purposely strive to produce *monodisperse* (i.e., of a single size) particles. A second goal is to develop a new framework for assessing potential hazards, using new toxicologic data [51].

Since 2005, NIOSH activities for advancing risk assessment have included analyzing existing data on titanium dioxide (TiO₂), developing lung deposition models, performing extensive literature reviews on ultrafines, developing hazard and risk estimates for carbon and metal nanoparticles using new NIOSH toxicity data, and calibrating models using new toxicity data. Future risk assessment research planned for fiscal years 2011-2012 includes evaluating/validating exposure-dose response models, investigating models with additional routes of exposure, developing risk estimates using models, and characterizing risk of nanoparticle exposure in the workplace [52].

2.4.1.1 Framework Shortfalls.

Even with this extensive on-going research agenda, the current risk assessment framework based on using existing knowledge on similar sized non-engineered particles has many shortfalls. As stated earlier, using research data from ultrafines generated during combustion processes, welding, and mining dust does not factor in the unique toxicological effects due to engineered properties of nanoparticles, such as increased surface area of nanoparticles leading to higher biological activity. In addition, the framework does not even begin to address even a fraction of the sheer number of nanoparticle variants that are possible.

2.4.2 Existing Models.

Although there are many PBPK models in literature, most focus on chemicals and not particle biokinetics. Models that are specific to nanoparticles are primarily focused on the lungs. Several very detailed lung models exist in the literature, including those by Tran et al. and Kuempel [79, 78, 40]. These models address the complexities presented by nanoparticles, including deposition, sequestration, phagocytosis, and interstitial translocation in the lungs.

Figure 7 on the following page shows the hypothesized model of Tran and Donaldson, which is perhaps the first one published specific to nanoparticles and serves as a baseline for this dissertation research. In the next chapter, the methodology to construct and analyze a PBPK model is described.

Extension of PBPK model

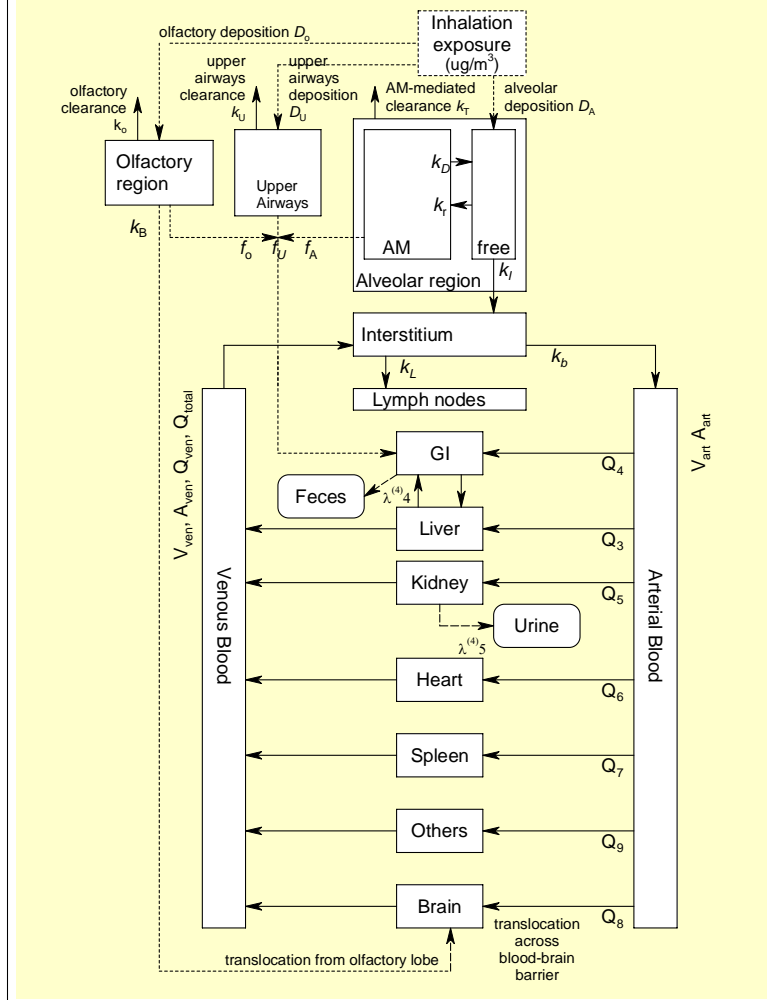


Figure 7. Hypothesized PBPK model for nanoparticles (from Tran/Donaldson)[77]

III. Methodology

“Essentially, all models are wrong, but some are useful.”

- George Box

3.1 Phase I: Model Formulation

Developing an overall model of human exposures to nanoparticles is especially important in the absence of extensive in vivo research and published exposure standards on a limitless variety of engineered nanomaterials that are possible. As mentioned in Shelley, et al., it is important to be able to translate the findings from the ever-growing in vitro nanotoxicity data into in vivo effects, in order to enhance risk assessment. In their article, the authors underscore the importance of developing PBPK models, which will also help accelerate development of nanoparticle risk assessment [68].

3.1.1 A Simple Three-Compartment Model.

To describe how the PBPK model for this research was developed, first consider two compartments linked together by a third compartment as shown in Figure 8. The lines with arrows represent systemic blood flow, with Q denoting blood flowrate (liter-s/hour) and C denoting nanoparticle concentration (# particles/liter). The product of $Q \cdot C$ represents a rate term (# particles/hour). Compartment 3, which is where contributions from compartments 1 and 2 are combined, is representative of the lung compartment.

As described earlier in Section 2.3 on page 25, we can denote the accumulation in any compartment as:

$$\text{Accumulation} = \frac{\text{change in amount}}{\text{time}} = \sum_{i=1}^n \text{Input}_i - \sum_{j=1}^m \text{Output}_j \quad (6)$$

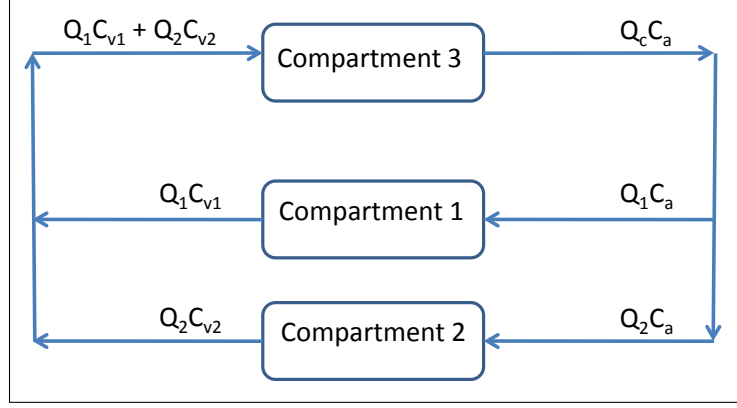


Figure 8. Conceptual PBPK model, with three compartments

For the three compartments shown in Figure 8, the following ordinary differential equations can be written as shown in Equations 7a to 7c on this page.

$$\frac{d(C_1 V_1)}{dt} = V_1 \frac{dC_1}{dt} = Q_1 C_a - Q_1 C_{v1} = Q_1 C_a - \frac{Q_1 C_1}{P_1} \quad (7a)$$

$$\frac{d(C_2 V_2)}{dt} = V_2 \frac{dC_2}{dt} = Q_2 C_a - Q_2 C_{v2} = Q_2 C_a - \frac{Q_2 C_2}{P_2} \quad (7b)$$

$$\begin{aligned} \frac{d(C_a V_3)}{dt} &= V_3 \frac{dC_a}{dt} = Q_1 C_{v1} + Q_2 C_{v2} - Q_c C_a \\ &= \frac{Q_1 C_1}{P_1} + \frac{Q_2 C_2}{P_2} - Q_c C_a \end{aligned} \quad (7c)$$

where

C_x = nanoparticle concentration (#particles per liter)

V_x = volume (liters)

Q_x = blood flowrate (liters per hour)

P_x = partition coefficient (unitless)

We can then consolidate the system of ODEs into matrix notation, with the first, second, and third rows representing the ODEs for compartments 1, 2, and 3, re-

spectively. Terms can be grouped, resulting in a matrix A multiplied by a vector of concentrations, as shown below.

$$V \frac{d}{dt} \begin{bmatrix} C_1 \\ C_2 \\ C_a \end{bmatrix} = \text{Input} - \text{Output} \quad (8a)$$

$$= \begin{bmatrix} Q_1 C_a \\ Q_2 C_a \\ \frac{Q_1 C_1}{P_1} + \frac{Q_2 C_2}{P_2} \end{bmatrix} - \begin{bmatrix} \frac{Q_1 C_1}{P_1} \\ \frac{Q_2 C_2}{P_2} \\ Q_c C_a \end{bmatrix} \quad (8b)$$

$$= \begin{bmatrix} 0 & 0 & Q_1 \\ 0 & 0 & Q_2 \\ \frac{Q_1}{P_1} & \frac{Q_2}{P_2} & 0 \end{bmatrix} \begin{bmatrix} C_1 \\ C_2 \\ C_a \end{bmatrix} - \begin{bmatrix} \frac{Q_1}{P_1} & 0 & 0 \\ 0 & \frac{Q_2}{P_2} & 0 \\ 0 & 0 & Q_c \end{bmatrix} \begin{bmatrix} C_1 \\ C_2 \\ C_a \end{bmatrix} \quad (8c)$$

$$= \begin{bmatrix} -\frac{Q_1}{P_1} & 0 & Q_1 \\ 0 & -\frac{Q_2}{P_2} & Q_2 \\ \frac{Q_1}{P_1} & \frac{Q_2}{P_2} & -Q_c \end{bmatrix} \begin{bmatrix} C_1 \\ C_2 \\ C_a \end{bmatrix} \quad (8d)$$

As V=diagonal matrix of the subcompartment volumes, we can write V^{-1} as follows:

$$V = \begin{bmatrix} V_1 & 0 & 0 \\ 0 & V_2 & 0 \\ 0 & 0 & V_3 \end{bmatrix} \Rightarrow V^{-1} = \begin{bmatrix} \frac{1}{V_1} & 0 & 0 \\ 0 & \frac{1}{V_2} & 0 \\ 0 & 0 & \frac{1}{V_3} \end{bmatrix}$$

Therefore,

$$\Rightarrow \frac{d}{dt} \begin{bmatrix} C_1 \\ C_2 \\ C_a \end{bmatrix} = V^{-1} \begin{bmatrix} -\frac{Q_1}{P_1} & 0 & Q_1 \\ 0 & -\frac{Q_2}{P_2} & Q_2 \\ \frac{Q_1}{P_1} & \frac{Q_2}{P_2} & -Q_c \end{bmatrix} \begin{bmatrix} C_1 \\ C_2 \\ C_a \end{bmatrix} \quad (9a)$$

$$= \begin{bmatrix} \frac{1}{V_1} & 0 & 0 \\ 0 & \frac{1}{V_2} & 0 \\ 0 & 0 & \frac{1}{V_3} \end{bmatrix} \begin{bmatrix} -\frac{Q_1}{P_1} & 0 & Q_1 \\ 0 & -\frac{Q_2}{P_2} & Q_2 \\ \frac{Q_1}{P_1} & \frac{Q_2}{P_2} & -Q_c \end{bmatrix} \begin{bmatrix} C_1 \\ C_2 \\ C_a \end{bmatrix} \quad (9b)$$

$$= \begin{bmatrix} -\frac{Q_1}{P_1 V_1} & 0 & \frac{Q_1}{V_1} \\ 0 & -\frac{Q_2}{P_2 V_2} & \frac{Q_c}{V_2} \\ \frac{Q_1}{P_1 V_3} & \frac{Q_2}{P_2 V_3} & -\frac{Q_c}{V_3} \end{bmatrix} \begin{bmatrix} C_1 \\ C_2 \\ C_a \end{bmatrix} \quad (9c)$$

$$= \begin{bmatrix} & & \\ A & & \\ & & \end{bmatrix} \begin{bmatrix} C_1 \\ C_2 \\ C_a \end{bmatrix} \quad \text{“Matrix Form”} \quad (9d)$$

Writing the system of ODEs in matrix form allows eigenvalues and eigenvectors to be calculated, which can be used to determine the solution to the system and for eigenvalue analysis. Both of these items will be discussed later on.

3.1.2 Additions to the Three-Compartment Model.

To extend this model further, we can include mechanisms such as a source term, exchange between two compartments, and a loss mechanism. See Figure 9. Here, the source term, s , is shown as a constant input to Compartment 3. We also expand the model to include a subcompartment representing the tissue portion of an organ, to demonstrate an exchange between blood and tissue. In this example, a blood subcompartment is connected to a tissue subcompartment with diffusion as the transport

process.

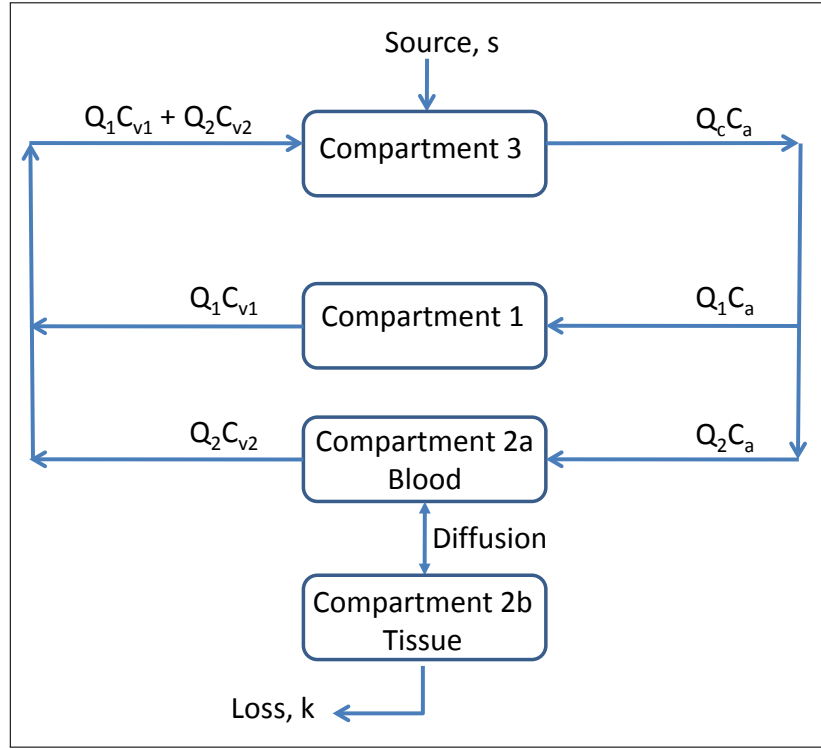


Figure 9. Three compartment model with source, exchange, loss

$$\frac{d(C_1 V_1)}{dt} = V_1 \frac{dC_1}{dt} = Q_1 C_a - Q_1 C_{v1} = Q_1 C_a - \frac{Q_1 C_1}{P_1} \quad (10a)$$

$$\begin{aligned} \frac{d(C_{2a} V_{2a})}{dt} &= V_{2a} \frac{dC_{2a}}{dt} = Q_2 C_a - Q_2 C_{v2} - T \left(C_{2a} - \frac{C_{2b}}{P_{2b:2a}} \right) \\ &= Q_2 C_a - \frac{Q_2 C_{2a}}{P_2} - T \left(C_{2a} - \frac{C_{2b}}{P_{2b:2a}} \right) \end{aligned} \quad (10b)$$

$$\frac{d(C_{2b} V_{2b})}{dt} = V_{2b} \frac{dC_{2b}}{dt} = T \left(C_{2a} - \frac{C_{2b}}{P_{2b:2a}} \right) - k C_{2b} \quad (10c)$$

$$\begin{aligned} \frac{d(C_a V_3)}{dt} &= V_3 \frac{dC_a}{dt} = Q_1 C_{v1} + Q_2 C_{v2} - Q_c C_a + s \\ &= \frac{Q_1 C_1}{P_1} + \frac{Q_2 C_2}{P_2} - Q_c C_a + s \end{aligned} \quad (10d)$$

The equations below show the formulation of the system of ordinary differential equations.

$$V \frac{d}{dt} \begin{bmatrix} C_1 \\ C_{2a} \\ C_{2b} \\ C_a \end{bmatrix} = \text{Input} - \text{Output} + \text{Exchange} - \text{Loss} + \text{Source} \quad (11a)$$

$$\Rightarrow \frac{d}{dt} \begin{bmatrix} C_1 \\ C_{2a} \\ C_{2b} \\ C_a \end{bmatrix} = \dots = V^{-1} \begin{bmatrix} -\frac{Q_1}{P_1} & 0 & 0 & Q_1 \\ 0 & -\frac{Q_2}{P_2} - T & \frac{T}{P_{2b:2a}} & Q_2 \\ 0 & T & -\frac{T}{P_{2b:2a}} - k & 0 \\ \frac{Q_1}{P_1} & \frac{Q_2}{P_2} & 0 & -Q_c \end{bmatrix} \begin{bmatrix} C_1 \\ C_{2a} \\ C_{2b} \\ C_a \end{bmatrix} + V^{-1} \begin{bmatrix} 0 \\ 0 \\ 0 \\ s \end{bmatrix} \quad (11b)$$

$$= \dots = \begin{bmatrix} -\frac{Q_1}{P_1 V_1} & 0 & 0 & \frac{Q_1}{V_1} \\ 0 & -\frac{Q_2}{P_2 V_{2a}} - \frac{T}{V_{2a}} & \frac{T}{P_{2b:2a} V_{2a}} & \frac{Q_2}{V_{2a}} \\ 0 & \frac{T}{V_{2b}} & -\frac{T}{P_{2b:2a} V_{2b}} - \frac{k}{V_{2b}} & 0 \\ \frac{Q_1}{P_1 V_3} & \frac{Q_2}{P_2 V_3} & 0 & -\frac{Q_c}{V_3} \end{bmatrix} \begin{bmatrix} C_1 \\ C_{2a} \\ C_{2b} \\ C_a \end{bmatrix} + \begin{bmatrix} 0 \\ 0 \\ 0 \\ \frac{s}{V_3} \end{bmatrix} \quad (11c)$$

$$= \begin{bmatrix} & & & \\ & A & & \\ & & & \end{bmatrix} \begin{bmatrix} C_1 \\ C_{2a} \\ C_{2b} \\ C_a \end{bmatrix} + \begin{bmatrix} 0 \\ 0 \\ 0 \\ \frac{s}{V_3} \end{bmatrix} \quad (11d)$$

3.1.2.1 Software Implementation.

Software such as STELLA[®], makes construction of PBPK and other types of models a relatively simple procedure using drag-and-drop icons that are connected together. Figure 10 shows the various objects that can be used in STELLA[®], along with a visual example of how a simple PBPK compartment (i.e., organ) is quickly modeled using those same icons. Stocks are used to model accumulation in compartments or subcompartments and each stock yields an ODE. Flows are used to represent rates of transport (either blood- or other flow rate). Converters are used to implement various physiological or transport parameters. Connectors (i.e., red arrows) are used to connect icons together.

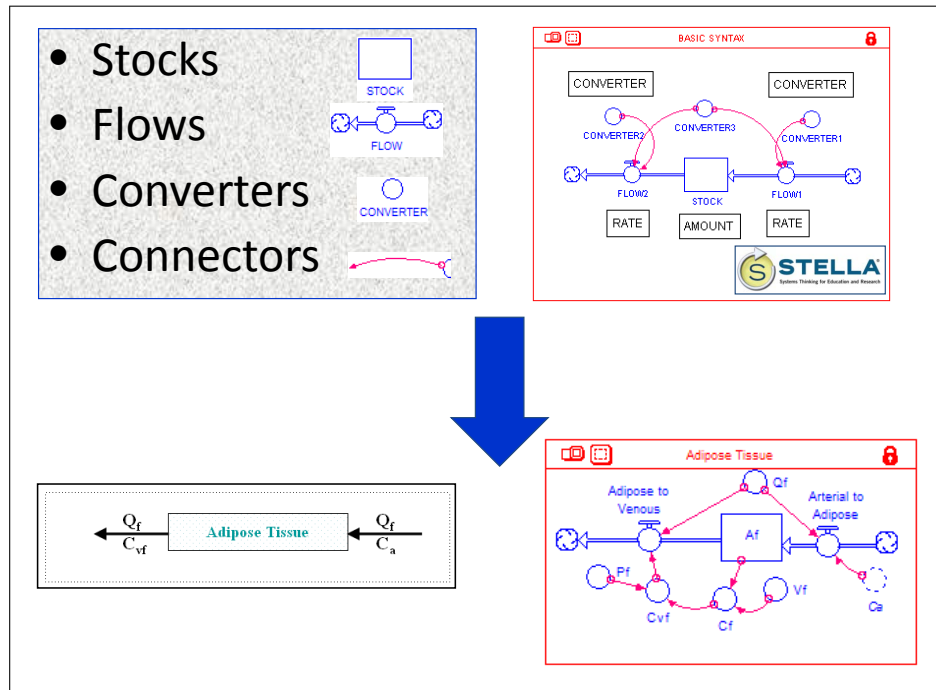


Figure 10. STELLA[®] icons used for modeling [70]

Alternatively, using MATLAB[®] allows greater flexibility as complex simulations (e.g., for-loops, etc.) can be run and eigenvalue analysis can be performed. Although the complexity of this research warrants use of MATLAB[®], an identical version of the

model will be maintained in STELLA[®], as it provides an easy-to-visualize pictorial representation and can be used to help validate MATLAB[®] results as modifications to the model are made. Additional benefits of using MATLAB[®] include its more powerful suite of ODE solvers (numerical methods), flexibility, and overall robustness when it comes to simulations and analysis of systems.

3.1.3 The PBPK Model.

The next phase of research included developing a whole-body human PBPK model. First, a comprehensive literature review was conducted to identify the organs critical to distribution and uptake, and also organs that could be toxicological endpoints. This information, combined with physiology and anatomy fundamentals, was used to begin developing the PBPK model. The methodology of assembling ODEs for a simple three-compartment model in Sections 3.1.1 and 3.1.2 was used to assemble the full PBPK model. The format of the matrices used for the full PBPK model can be viewed in Appendix D on page 158.

The PBPK model includes compartments for the lungs, liver, gastrointestinal tract, kidneys, spleen, brain, slowly perfused tissue, and other richly perfused tissue. The lungs are an essential part to the model, as they provide the inhalational exposure pathway for nanoparticles. It is modeled using more complexity than most traditional PBPK models as deposition and clearance processes are included. More traditional models often assume rapid equilibration across the alveolar walls, no significant metabolism (loss mechanism) in lung tissue, and negligible storage capacity (buildup) in the lungs [65].

The liver, GI tract, kidneys, spleen, and brain are included due to their possible role in transport, removal, and accumulation of nanoparticles [20, 57, 54]. The slowly- and richly perfused tissue compartments account for the remainder of the human body

to maintain mass balance. Slowly perfused tissue includes muscle, skin, and fat. Liver, kidneys, spleen, brain, slowly-perfused, and richly perfused are modeled using blood, extracellular, and intracellular subcompartments, whereas the GI tract is modeled with two subcompartments (lumen and blood), due to its anatomical structure. See Figure 11.

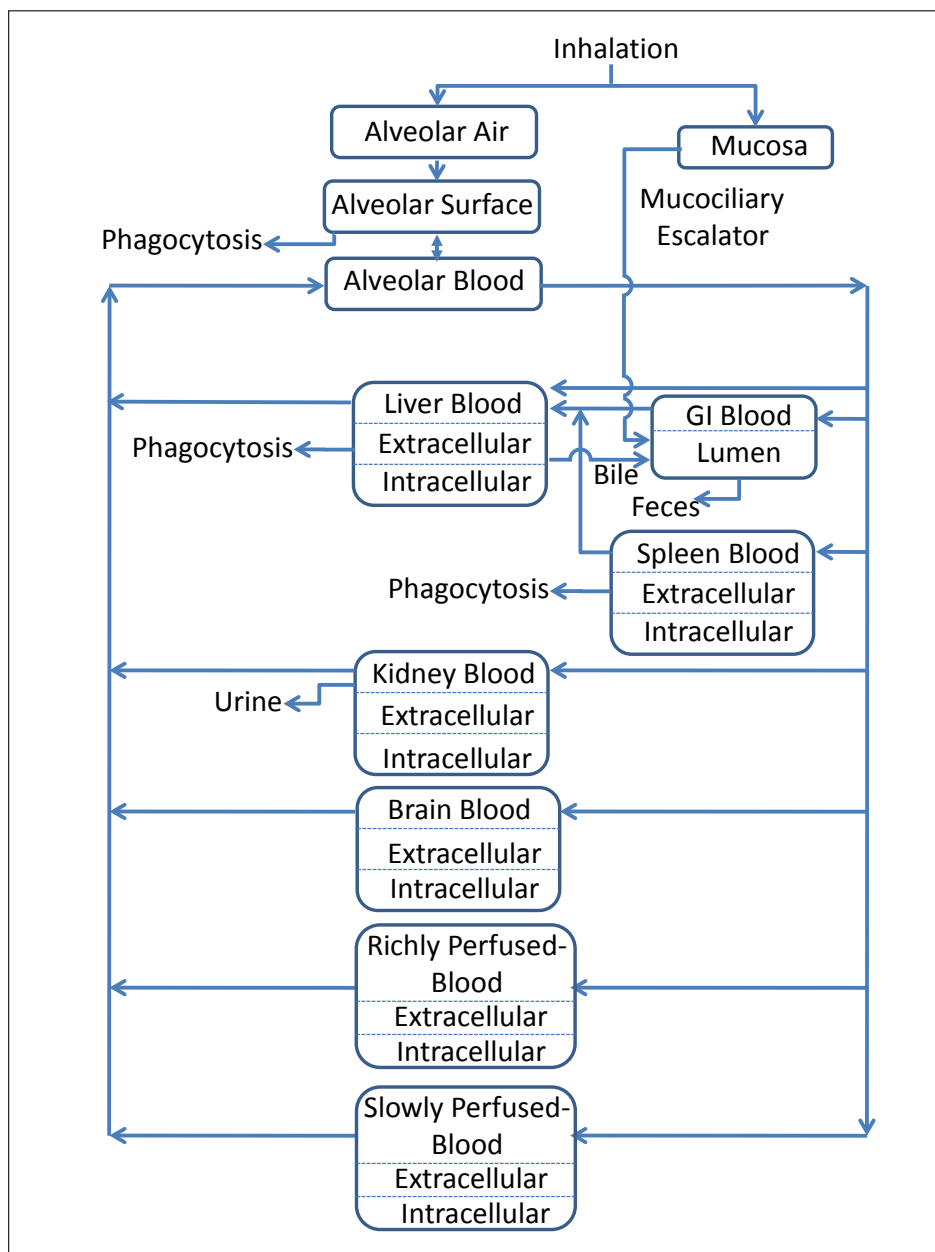


Figure 11. Full PBPK model for nanoparticle exposures

Three primary design considerations for the PBPK model are inclusion of particle deposition, translocation, and loss mechanisms. *Particle deposition* involves where in the respiratory tract nanoparticles are deposited. *Translocation* describes the movement of particles out of the respiratory tract. Various *loss mechanisms* are included as they explain how nanoparticles can, in theory, be removed from the body. Full explanations of these three design considerations are shown below.

3.1.3.1 Particle Deposition.

Given a constant inhalational source, these nanoparticles may undergo deposition in the head-airways, tracheobronchial, or alveolar regions of the lungs. Deposition behavior is based on size, with large particles >100 nm being primarily deposited in the head-airways region of the respiratory tract. At sizes <100 nm, deposition in the head-airways increases as size decreases, leaving fewer particles available for deposition lower in the respiratory tract. See Figure 12.

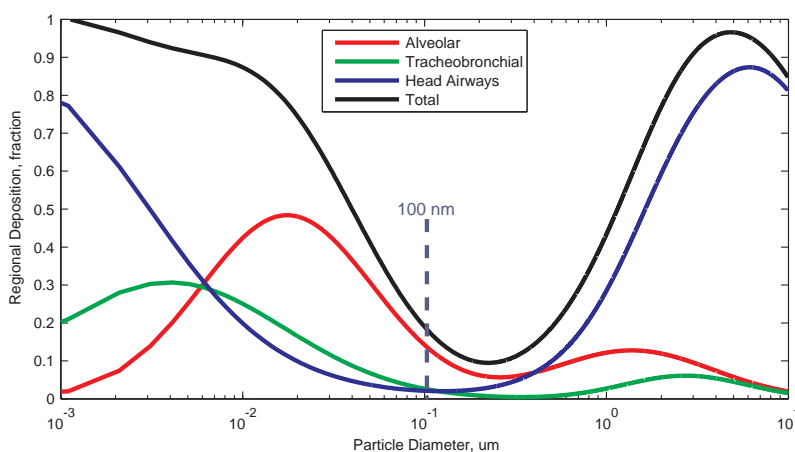


Figure 12. Deposition in the respiratory tract, based on particle size (*adapted from Hinds*) [26]

3.1.3.2 Translocation.

If deposited in the tracheobronchial or head-airways regions, particles may be removed to the GI tract via mucociliary clearance. For the tracheobronchial region, we simplify the model by assuming uniform nanoparticle distribution over the inner surface of a cylinder, with uniform mucus transport velocity also. The rate of nanoparticles exiting the tube via mucociliary clearance is calculated by multiplying the surface area concentration (i.e., # of nanoparticles per area) by mucus transport velocity and trachea perimeter. Particles leaving the trachea via mucociliary clearance then travel to the GI tract thru ingestion.

Particles deposited in the alveolar region (i.e., deep lung) can undergo translocation to reach systemic blood flow and distribution throughout the body. Arterial blood with a flow rate equal to cardiac output, Q_c , is distributed to the five primary organs in the model (i.e., GI tract, spleen, liver, kidneys, and brain), with the balance of the body's tissue being clustered as *richly perfused tissue* and *slowly perfused tissue*.

It is also assumed that reverse translocation can occur (i.e., nanoparticles can travel from alveolar blood back to the alveolar surface) as the barrier is only two cells thick. However, the model does not include the ability for nanoparticles to leave the alveolar surface and enter alveolar air, as no evidence suggests that nanoparticles can be re-entrained into alveolar air, unlike chemicals.

3.1.3.3 Loss Mechanisms.

The primary loss mechanisms out of the system are through exhalation, urine, feces, and phagocytosis. These loss mechanisms are critical as they explain how nanoparticles leave the body and allow the system to approach steady state, as will be discussed in Chapter 4.

Understanding the physiology is critical to building an adequate PBPK model. Several of the key physiological design features include:

- Primary exposure pathway is inhalational exposure
- Secondary exposure pathway: ingestion of nanoparticles cleared from the respiratory tract due to mucociliary clearance
- Exhalation and phagocytosis are additional means of clearance from the respiratory tract
- A simplified approach to model the respiratory system was used. More complex models exist [67, 79, 78], but are beyond the scope of this research.
- GI tract was included as it receives particles cleared from the respiratory tract and as GI blood must flow first to the liver before reaching systemic circulation (i.e., “first-pass effect”)
- The spleen serves as a size-dependent filtering mechanism which traps particles of large enough size; what is not filtered can serve as additional burden on the liver, similar to GI blood. Phagocytosis occurs in the spleen, also.
- The liver is similar to the spleen as it is a filtering mechanism and has phagocytosis present. Like the kidneys, it has a very large inflow of blood. Besides phagocytosis, the liver can also excrete waste to the GI tract, via bile.
- The kidneys allow particles that are small enough to pass through the glomerulus (i.e., glomerular filtration) for excretion via urine. Larger particles cannot pass across this glomerular boundary (aka Bowman’s Capsule) and are presumably returned to systemic flow. Reabsorption and secretion are not modeled here.
- Phagocytosis is modeled as a first-order loss and is present in the lungs, liver, and spleen.

Typically, bloodflow rates to each organ are expressed as fractions of cardiac output, Q_c , with the sum total of the fractions equaling one. Organ volumes are commonly derived from body weight, BW. This convention of using Q_c and BW allows for allometric scaling, which is the scaling of parameters based on different size mammals. The values for Q_c and BW used in the model are shown in Table 1. Blood flow fractions, based on Q_c , are shown in Table 2 on the next page and organ volume fractions, based on BW, are shown in Table 3.

Table 1. Physiological parameters for the PBPK model

Physiological Parameter	Variable	Value	Reference	Notes
Cardiac Output	Q_c	290 liters/hr	[61]	blood flow rates to organs: fractions of Q_c
Body Weight	BW	70 kg	[76]	tissue volumes expressed as a function of BW

Table 2. Fractions of cardiac output

Physiological Parameter	Variable	Fraction of Cardiac Output	Reference	Notes
Fraction of cardiac output to liver	LQ_{frac}	0.06	[76]	Net of 27% when including portal circ.
Fraction of cardiac output to portal circ.	$PortalQ_{frac}$	0.21	[76]	Includes GI tract and spleen
Fraction of cardiac output to GI	GIQ_{frac}	0.195	–	Back-calculated: =portal - spleen
Fraction of cardiac output to spleen	$SplQ_{frac}$	0.015	[76]	
Fraction of cardiac output to kidneys	KQ_{frac}	0.223	[21]	
Fraction of cardiac output to brain	BQ_{frac}	0.134	[21]	
Fraction of cardiac output to RPT	RQ_{frac}	0.206	[21]	Adapted from Gearhart et al.
Fraction of cardiac output to SPT	SQ_{frac}	0.167	[21]	Adapted from by Gearhart et al.

Table 3. Organ volumes

Organ	Variable	Fraction of BW	Resulting Volume (liters)	Reference	Notes
Liver	LV_{frac}	0.04	2.8	[21]	
Kidneys	KV_{frac}	0.0043	0.3	[21]	
Spleen	$SplV_{frac}$	0.002	0.14	–	Assumed.
Brain	BV_{frac}	0.0214	1.5	[21]	
Richly Perfused	$rptV_{frac}$	0.0323	2.3	[21]	Adapted from Gearhart et al. by subtracting off spleen
Slowly Perfused	$sptV_{frac}$	0.7214	64	[21]	Adapted from Gearhart et al. by adding adipose

Traditional PBPK modeling often treats organ volume as being synonymous with tissue volume (i.e., treats blood volume as negligible), so few data exist detailing appropriate volumes for the blood portion in organs or tissue groups. In addition, no data were available detailing the amount of extracellular (i.e., “outside the cell”) and intracellular (i.e., “inside the cell”). Instead, estimates for these three volumes are shown in Table 4.

Table 4. Subcompartment volumes

Physiological Parameter	Variable	% of Organ Volume	Notes
Blood Volume	V_{blood}	10	Estimated since not known
Extracellular Space Volume	V_{extra}	50	Estimated since not known
Intracellular Space Volume	V_{intra}	40	Estimated since not known

3.1.4 Range Finding.

In traditional PBPK modeling, in vitro and in vivo data would be used to establish the key physiological and transport parameters for the PBPK model. An iterative approach is then taken, where the model mathematics are fine-tuned to represent in vivo results (i.e., model matches reality). Doing so, it creates a model that can then be used for extrapolation to higher doses and from species to species.

A goal of the research was to take the baseline model shown in Section 3.1.3 and insert the mathematical representations of the transport processes to begin exploring the effects of these processes on the biokinetics of nanoparticles in the body. For this research, however, there are no definitive data to represent the transport parameters shown in Table 5 on the next page and, therefore, the concept of *range finding* was proposed. The goal of the range finding is not to determine 100% correct values; rather, it is to perform a comparative analysis and identify reasonable values to enable this explorative PBPK model. A single value is chosen for each transport parameter and is used across all organs, in order to enable the model. Note that the transport parameters will be modified later, based on physico-chemical properties suggested by literature, to provide organ-specific behavior. This will be discussed later in Section 3.2.

Other parameters exist which are important to the PBPK model, but are of secondary importance as compared to the parameters described in Table 5 on the following page. A summary of the transport parameters that are not part of range finding is shown in Table 6 on the next page. Note that the partition coefficients establish the ratio of concentrations as they approach steady state, while the Michaelis-Menten constants help define the steepness of the Michaelis-Menten curves, which are plots of transport rate vs. concentration.

Table 5. Transport parameters needing range finding

Physiological Parameter	Variable	Notes
Transfer Coefficient, blood-to-tissue	$T_{b:t}$	For diffusion between blood and tissue
Transfer Coefficient, extra-to-intracellular	$T_{e:i}$	For diffusion between extra- and intracellular
Active Transport, Max Rate of Transport	$V_{\max at}$	Saturable rate for active transport from extra- and intracellular
Carrier Mediated Transport, Max Rate of Transport	$V_{\max cmt1}$	Saturable rate for carrier mediated transport from extra- to intracellular
Carrier Mediated Transport, Max Rate of Transport	$V_{\max cmt2}$	Saturable rate for carrier mediated transport from intra- to extracellular

Table 6. Transport parameter values selected

Physiological Parameter	Variable	Value Chosen	Notes
Partition Coefficient tissue-to-blood	$P_{t:b}$	2	Estimated since not known.
Partition Coefficient intra-to-extracellular	$P_{i:e}$	3	Estimated since not known.
Active Transport, Michaelis-Menten Const.	K_{mat}	1	Estimated since not known. Active transp extra- to intra-.
Carrier Mediated, Michaelis-Menten Const1	K_{mcmt1}	1	Estimated since not known. Carrier med. from extra- to intra-.
Carrier Mediated, Michaelis-Menten Const2	K_{mcmt2}	1	Estimated since not known. Carrier med. from intra- to extra-.

3.1.4.1 Range Finding for $T_{b:t}$.

The first transport parameter needing range finding (Table 5) is the blood-to-tissue transfer coefficient, $T_{b:t}$, for diffusion between blood and tissue in the various organs. For this portion of range finding, each organ is represented using two subcompartments (i.e., blood and tissue). IE is a long-standing, traditional modeling technique used in PBPK modeling and as it represents the fastest a compartment can “load up”, it is treated as an upper bound. A single value for $T_{b:t}$ is selected by finding a value that best keeps all organ concentrations in mid-range between the concentrations seen

while using IE and zero. Mid-range was chosen as it provides concentration results distinguishable from IE, while avoiding near-zero concentrations which will not provide meaningful insight into organ behavior. For some organs, concentration remains fairly constant even as $T_{b:t}$ is varied, so determining a true mid-range value is not possible.

3.1.4.2 Range Finding for $T_{e:i}$.

To do range finding on $T_{e:i}$, we first insert the value for $T_{b:t}$ chosen during the exercise described in the paragraph above, which defines the diffusion behavior between blood and extracellular. As $T_{e:i}$ represents the transport parameter governing diffusion between extracellular and intracellular, the model is changed to the three-subcompartment setup (i.e., blood, extra-, and intracellular). $T_{e:i}$ is then varied over a range to find a single value that can be used across all organs. In the absence of quantitative data describing reasonable tissue concentrations for diffusion between extracellular and intracellular environments, a $T_{e:i}$ value was chosen that keeps concentrations within $2\times$ those seen by using the value of $T_{b:t}$ chosen in the previous step. Although an arbitrary value, using this criteria results in concentrations within reason (i.e., not inexplicably large).

3.1.4.3 Range Finding for V_{maxat} .

Range finding for V_{maxat} , which is the Michaelis-Menten maximum rate for active transport from extracellular to intracellular, relies on a three-subcompartment representation for each organ. For this simulation, active transport and diffusion work in parallel between extra- and intracellular subcompartments. V_{maxat} is varied over a range of values and the goal is to choose a value for V_{maxat} that best keeps concentrations within $2\times$ those seen by using the value of $T_{e:i}$ chosen in the previous

step. Using this criteria results in concentrations within reason, avoiding possibly unrealistic concentrations due to V_{maxat} . The value chosen for V_{maxat} is also used as V_{maxcmt1} since both represent saturable (Michaelis-Menten) terms in the extracellular-to-intracellular direction.

3.1.4.4 Range Finding for V_{maxcmt2} .

For this simulation, carrier mediated transport and diffusion are modeled as working in parallel between the extracellular and intracellular subcompartments. The goal here is to choose a value for V_{maxcmt2} that best keeps concentrations within $2\times$ those seen by using the value of $T_{\text{e:i}}$ chosen earlier. Using this criterial avoids possibly unrealistic concentrations in tissue due to V_{maxcmt2} .

3.1.5 Eigenvalue Analysis.

3.1.5.1 Eigenvalue Overview.

We use linear algebra to represent a system of differential equations by first deriving a square matrix, A , representing the physiological and transport parameters appearing in the concentration terms of the linear differential equations as described in Sections 3.1.1 to 3.1.2 on pages 33–36. The system is of the form:

$$\frac{d}{dt} \begin{bmatrix} C_1 \\ C_2 \\ C_a \end{bmatrix} = \text{Input} - \text{Output} + \text{Exchange} - \text{Loss} + \text{Source} \quad (12a)$$

$$= \begin{bmatrix} & & \\ & A & \\ & & \end{bmatrix} \begin{bmatrix} C_1 \\ C_2 \\ C_a \end{bmatrix} + \text{Source} \quad (12b)$$

This system can be rewritten in the form

$$\dot{\vec{c}} = A\vec{c} + \vec{s} \quad (12c)$$

where

$\dot{\vec{c}}$ = vector of time derivative concentrations, $\frac{dC}{dt}$

A = matrix of physiological and transport parameters

\vec{c} = vector of concentrations, with initial condition $\vec{c}(0) = 0$

\vec{s} = vector for the exposure source

Once in matrix form, the solution to the system can be found by determining the eigenvalues, λ , and the associated eigenvectors, \vec{v} , of the A-matrix. The equation $A\vec{v}=\lambda\vec{v}$ ($\vec{v} \neq 0$) characterizes the nature of the (λ, \vec{v}) pair. The eigenvalue satisfies the property that the determinant of $(A - \lambda I)=0$, where I =identity matrix. Explanations of eigenvalues and eigenvectors are shown below:

Explanation. An *eigenvalue* is a time scale indicating the rate of growth or decay for a given subcompartment.

Explanation. An *eigenvector* represents the distribution of the concentrations across subcompartment for a given time scale (eigenvalue).

Explanation. The *eigenstructure* is the set of paired eigenvalues and eigenvectors.

For this research, the eigenstructure for an A-matrix is displayed using a matrix with the eigenvalues in the top row and associated eigenvectors listed beneath the eigenvalues. See Figure 13. Terms comprising each eigenvector are normalized using the L1-norm, such that the sum of the absolute value of the terms equals one, i.e., $\sum_{i=1}^n |x_i| = 1$. By normalizing, the terms in an eigenvector represent fractional contributions of each subcompartment to the given time scale (i.e., eigenvalue).

$$\begin{bmatrix} \lambda_1 & \lambda_2 & \lambda_3 & \cdots & \lambda_{24} \\ \vec{v}_1 & \vec{v}_2 & \vec{v}_3 & \cdots & \vec{v}_{24} \end{bmatrix}$$

Figure 13. Eigenstructure format for full 24-subcompartment model

3.1.5.2 Writing the Solution to the Linear System.

Eigenvalues and eigenvectors are important as they can be used to write the solution to the non-homogenous linear system of the form $\mathbf{x}' = \mathbf{Ax} + \mathbf{g}(t)$. For this research, the system is written as shown in Equation 12c on page 52, given the initial condition $\vec{c}(0) = 0$.

The solution to the non-homogeneous linear system in Equation 12c can be written as shown in Equation 13. The number of terms to be summed, n , is defined by the number of subcompartments (i.e., state variables). As an example, if there are three subcompartments in the model (i.e., $n=3$), then the vector of concentrations, $\vec{c}(t)$, will be the summation of three terms related to three pairs of eigenvalues and eigenvectors, (λ_k, \vec{v}_k) . See Appendix E on page 167 or Boyce and DiPrima [7] for more details on development of the solution.

$$\vec{c}(t) = \sum_{k=1}^n \frac{f_k}{-\lambda_k} (1 - e^{\lambda_k t}) \vec{v}_k \quad (13)$$

where

f_k = the k^{th} term of the vector \vec{f} which is the

inverse of the eigenvector matrix \cdot source vector

λ_k = the k^{th} eigenvalue, λ , with $\lambda \neq 0$ and $k=1, 2, \dots, n$

\vec{v}_k = the k^{th} eigenvector, $k=1, 2, \dots, n$

As $t \rightarrow \infty$, the exponential terms in Equation 13 go to zero and the steady state solution is

$$\vec{c}_{ss} = \sum_{k=1}^n \frac{f_k}{-\lambda_k} \vec{v}_k. \quad (14)$$

Alternatively, the steady state solution can be found by setting $\dot{\vec{c}}=0$ in Equation 12c on page 52 and solving for \vec{c}_{ss} (steady state), i.e.,

$$\text{As } t \rightarrow \infty \quad \vec{c}(t) \approx \vec{c}_{ss} = -A^{-1}\vec{s} \quad (15)$$

3.1.5.3 Interpretation of the Eigenvalues.

Larger magnitude (negative) eigenvalues cause more rapid decay of the exponential terms, leading to a rapid approach to steady state concentrations (i.e., rapid buildup of nanoparticles). Conversely, small magnitude (negative) eigenvalues indicate a slower buildup/approach to steady state concentration [86, 85].

3.1.5.4 An Example of Eigenvalue Analysis.

Eigenvalue analysis can be applied on the entire model, but the example presented here focuses on a single organ. For this example, we first exclude all other organs, thus reducing the model to a system of three ordinary differential equations. The input source is ignored and the kidney output is looped around to become the kidney input. An assumption is that a fraction of nanoparticles, e.g., 20%, is excreted via urine. Here, the transfer coefficient governing the diffusion process between extracellular and intracellular subcompartments for the kidney is being varied. See Figure 14 on the following page.

Using the technique described in Section 3.1.1 on page 33, the ODEs for the three-subcompartment system can be written in matrix form with an A-matrix of physiological and transport parameters multiplied by a vector of concentrations, as shown in Equation 16 on the following page.

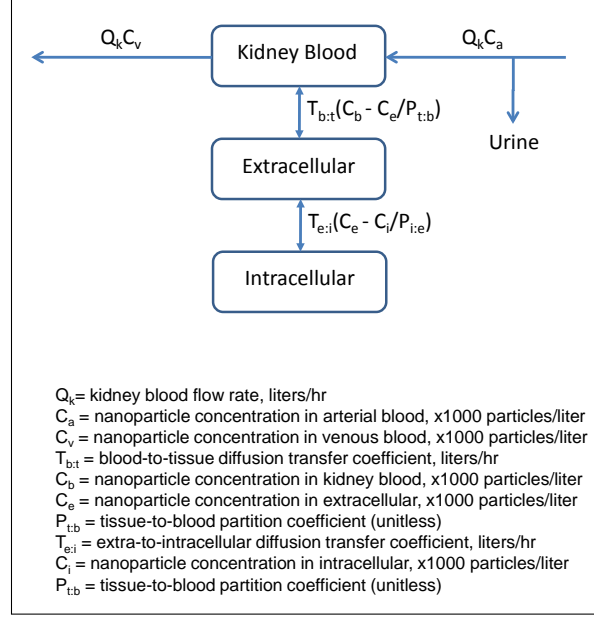


Figure 14. Subassemblies for the kidneys

$$A \cdot \vec{c} = \begin{bmatrix} \frac{-T_{b:t} - 0.2 \cdot Q_k}{V_b} & \frac{T_{b:t}}{P_{t:b} V_b} & 0 \\ \frac{T_{b:t}}{V_e} & -\frac{T_{b:t}}{P_{t:b} V_e} - \frac{T_{e:i}}{V_e} & \frac{T_{e:i}}{P_{i:e} V_e} \\ 0 & \frac{T_{e:i}}{V_i} & -\frac{T_{e:i}}{P_{i:e} V_i} \end{bmatrix} \begin{bmatrix} C_b \\ C_e \\ C_i \end{bmatrix} \quad (16)$$

Varying the transport parameters, such as during range finding, will yield a different A-matrix and, hence, a different eigenstructure. Therefore, we can recalculate the eigenvalues for subcompartments of the model to observe model behavior as a specific transport parameter is varied. Note that discerning the cause of behavior changes may be difficult if multiple parameters are changed simultaneously and, therefore, only one parameter is varied at a time. For a three-subcompartment model, the resulting eigenstructure has three eigenvalues with associated eigenvectors, as shown in Figure 15.

To demonstrate eigenvalue analysis, we can then increase the extracellular-to-intracellular diffusion transfer coefficient, $T_{e:i}$, and determine the resulting eigenstructures as shown in Figure 16 on the next page. As described earlier, the eigenvalues are

$$\begin{bmatrix} \lambda_1 & \lambda_2 & \lambda_3 \\ \hline \vec{v}_1 & \vec{v}_2 & \vec{v}_3 \end{bmatrix} \quad (17)$$

Figure 15. Eigenstructure format for kidney three-subcompartment model

in the first row, with corresponding eigenvectors below the eigenvalues. The eigenvectors of the matrices can be used to determine which eigenvalue (i.e., time scale) each subcompartment predominantly operates at. In Figures 16a to 16f on this page, the first eigenvector (under the eigenvalue in column 1) has the largest value in the first row, which corresponds to the blood subcompartment. The second column has its largest value in the second row, which corresponds to extracellular. Finally, the third column has its largest value in the third row, corresponding to intracellular.

$$\begin{bmatrix} \mathbf{-600.5} & \mathbf{-12.56} & \mathbf{-0.262} \\ \hline -0.9461 & -0.1177 & 0.002445 \\ 0.05389 & -0.8264 & 0.01753 \\ 0 & 0.05588 & 0.98 \end{bmatrix} \quad \begin{bmatrix} \mathbf{-600.6} & \mathbf{-15.5} & \mathbf{-1.061} \\ \hline -0.9459 & -0.09958 & 0.009981 \\ 0.05412 & -0.6958 & 0.07147 \\ 0 & 0.2046 & 0.9185 \end{bmatrix}$$

(a) $T_{e;i}=0.1$

(b) $T_{e;i}=0.5$

$$\begin{bmatrix} \mathbf{-600.6} & \mathbf{-19.56} & \mathbf{-1.682} \\ \hline -0.9449 & -0.08796 & 0.01592 \\ 0.05437 & -0.6102 & 0.1139 \\ -0.0007554 & 0.3018 & 0.8702 \end{bmatrix} \quad \begin{bmatrix} \mathbf{-600.8} & \mathbf{-55.71} & \mathbf{-2.952} \\ \hline -0.9393 & -0.07167 & 0.02828 \\ 0.05671 & -0.4661 & 0.2019 \\ -0.004012 & 0.4623 & 0.7698 \end{bmatrix}$$

(c) $T_{e;i}=1$

(d) $T_{e;i}=5$

$$\begin{bmatrix} \mathbf{-601.2} & \mathbf{-102.2} & \mathbf{-3.217} \\ \hline -0.9312 & -0.07368 & 0.03091 \\ 0.06008 & -0.4379 & 0.2205 \\ -0.008702 & 0.4884 & 0.7486 \end{bmatrix} \quad \begin{bmatrix} \mathbf{-612.4} & \mathbf{-467.2} & \mathbf{-3.453} \\ \hline -0.7276 & -0.2221 & 0.03325 \\ 0.1452 & -0.3438 & 0.2371 \\ -0.1272 & 0.4342 & 0.7296 \end{bmatrix}$$

(e) $T_{e;i}=10$

(f) $T_{e;i}=50$

Figure 16. Eigenvalues and associated eigenvectors as $T_{e;i}$ is varied

Knowing which eigenvalue (i.e., time scale) that a subcompartment predominantly operates at allows plotting of eigenvalues for analysis. Figure 17 shows a plot of the eigenvalues belonging to each subcompartment as $T_{e,i}$ is varied. As the plot is log-log based, it is important to note that sloped lines indicate large changes in eigenvalues.

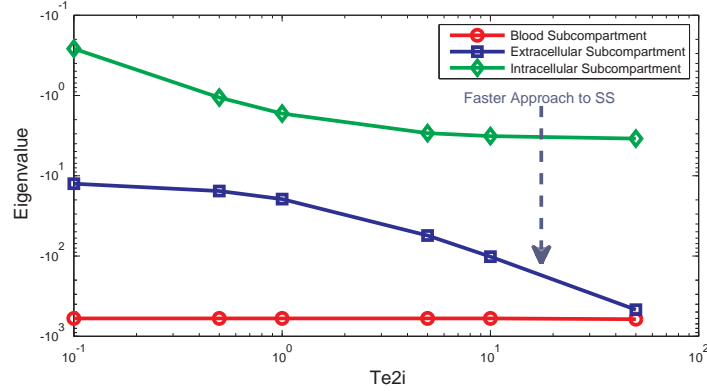


Figure 17. Example: log-log plot of the eigenvalues for the kidney as $T_{e,i}$ is varied

For the blood subcompartment (red line), the eigenvalue remains a relatively constant, large magnitude (negative) value, even as the transfer coefficient is varied. Rapid buildup of nanoparticles in the blood subcompartment occurs and it achieves steady state quickly, regardless of the value of $T_{e,i}$.

The blue line, representing kidney extracellular, shows that the magnitude of the eigenvalue increases exponentially as $T_{e,i}$ is increased, which indicates that it reaches steady state much faster at higher values of $T_{e,i}$. In contrast, the green line representing kidney intracellular shows the eigenvalue levels off as $T_{e,i}$ increases, which indicates the subcompartment reaches steady state at a slower rate and that this rate does not differ at higher levels of $T_{e,i}$. Therefore, increasing $T_{e,i}$ has the greatest effect on the extracellular subcompartment and has negligible effect on kidney blood and kidney intracellular.

Appendix E on page 167 provides further explanation on how the general- and steady state solutions can be derived using eigenvalues and eigenvectors. The ap-

pendix also extends the example shown in this section and details how the solution is comprised of contributions from separate exponential terms representing different time scales.

In summary, the eigenvalue analysis not only provides a pictorial representation of overall subcompartment behavior as a transport parameter is varied, but also can identify specific ranges where perturbations in rate parameters cause large increases in the eigenvalues. By identifying these ranges, future research can be focused and considerable resources saved by avoiding unnecessary in vitro and in vivo research.

3.2 Phase II: Inclusion of Physico-Chemical Properties

Now with the model complete, Phase II focuses on the effects of particle size, shape, and surface properties on model behavior. Shape, size, and surface properties can vary tremendously across nanoparticles and these properties are major determinants of the clearance kinetics, biodistribution, and toxicological impact of the particles [25, 72, 10]. Size influences many aspects of particle behavior, including degradation, flow properties, clearance, and uptake mechanisms [10]. Greater surface area per mass results in nanoparticles that are more biologically active than larger-sized particles of the same chemistry [57]. The focus of this research is not on the toxicological impact and, therefore nanoparticle properties such as surface area are not included.

In Phase I (see Section 3.1 on page 33), the baseline PBPK model was purposely developed without special consideration for particle size, shape, or surface properties as the goal was to simply create an operational, whole-body model. For Phase I, the general simplifying assumptions for the model included:

- (1) An inhalational exposure occurs and involves particles small enough to undergo interstitial translocation
- (2) A constant 50% of the exposure goes to alveolar air and 50% to mucosa
- (3) Each organ behaves similarly (e.g., same transport parameters apply across all organs)
- (4) Assume 20% of nanoparticles are excreted via urine in the kidney

To explore the impact of the physico-chemical parameters, key behaviors tied to particle size, shape, and surface characteristics were linked with the various transport parameters identified earlier in Section 2.2 on page 19. Whenever possible, specifics mentioned in the literature were used to generate piecewise linear functions to create modifying factors (“modifiers”) affecting nanoparticle transport. When specifics

were not available, qualitative zero-to-one linear modifiers were created to capture what interrelationships between particle size/shape/surface properties and transport behavior are mentioned in the literature. These modifiers are applied in appropriate points in the model to modify the transport parameters.

3.2.1 Size-Related Effects.

3.2.1.1 Size Effects on Lung Processes.

The biokinetics of nanoparticles is different than for larger particles as they are efficiently deposited in all three regions of the respiratory tract: the head airways, tracheobronchial, and alveolar regions. The head airways region includes the nose, mouth, pharynx, and larynx. The tracheobronchial region, also known as the lung airways region, includes the airways from the trachea to the terminal bronchioles. The alveolar region (deep lung) is where gas exchange occurs [26]. Figure 18 shows the three regions.

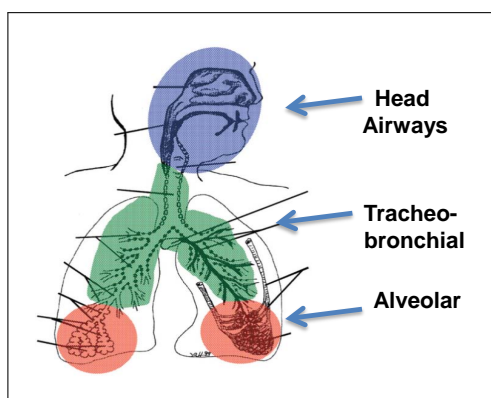


Figure 18. Regions of the respiratory tract (*adapted from Oberdörster, et al.*) [57]

Figure 19 on the following page shows the deposition fraction of particles in the three regions of the respiratory tract, based on particle diameter. Total deposition is simply the sum of the head-airways, tracheobronchial, and alveolar deposition fraction. The right-hand side of the figure shows that large particles, with aerodynamic

diameters $>1\ \mu\text{m}$ (or 1000 nm), are prone to deposition in the head airways [26]. This is due to inertial impaction, gravitational settling, and interception [57] and the relative effectiveness of the nasal hairs and bends in the airflow path through nasal passages [26].

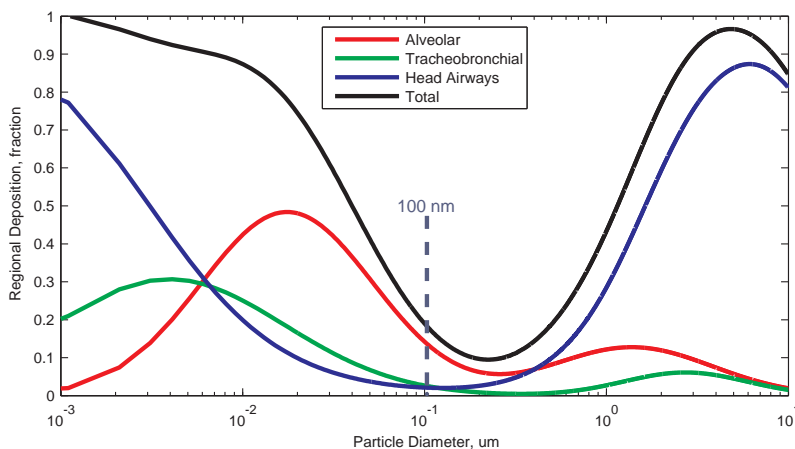


Figure 19. Deposition in the respiratory tract, based on particle size (*adapted from Hinds*) [26]

In contrast, diffusion dominates at smaller sizes and is the primary mechanism for deposition of inhaled nano-sized particles in the respiratory tract. Deposition at the smallest sizes (far left end of Figure 19) is predominantly in the head airways region, due to the effectiveness of the nasal structure. A dip in the deposition curves exists over the size range of 100 nm to $1\ \mu\text{m}$ represents a minimum in deposition probability [47], and is related to the transition from gravitational- to diffusion-dominated deposition. Coincidentally, the 100 nm size is notable also as *engineered* nanoparticles are commonly specified as being $<100\ \text{nm}$ in diameter.

The left-hand side of Figure 19 shows that for smaller particles ($<0.01\ \mu\text{m}$ or 10 nm), deposition in the head airways, especially the nasal region, is dominant (due to diffusion). This results in lower deposition rates in the tracheobronchial region (lung airways) and alveolar region for these sizes [26].

Differences between total deposition during nasal and oral breathing are minimal

for smaller particles [66]. For this research, an assumption of nose breathing is assumed, as it is the exposure scenario used to derive the deposition curves shown in Figure 19. Equations 18, 19, and 20 represent the curves and are estimates of the deposition fraction, DF, in the three respiratory system regions [26]. These equations can be used to more accurately specify the distribution of nano-sized particles to the three regions of the respiratory tract during Phase II, instead of relying on the assumptions in the baseline model listed in Section 3.2 on page 60.

$$\begin{aligned} \text{DF}_{\text{HA}} = & \left[1 - 0.5 \left(1 - \frac{1}{1 + 0.00076 d_p^{2.8}} \right) \right] \\ & \times \left[\frac{1}{1 + \exp(6.84 + 1.183 \ln d_p)} + \frac{1}{1 + \exp(0.924 - 1.1885 \ln d_p)} \right] \end{aligned} \quad (18)$$

$$\text{DF}_{\text{TB}} = \left(\frac{0.00352}{d_p} \right) [\exp(-0.234(\ln d_p + 3.4)^2) + 63.9 \exp(-0.819(\ln d_p - 1.61)^2)] \quad (19)$$

$$\text{DF}_{\text{ALV}} = \left(\frac{0.0155}{d_p} \right) [\exp(-0.416(\ln d_p + 2.84)^2) + 19.11 \exp(-0.482(\ln d_p - 1.362)^2)] \quad (20)$$

where

DF_{HA} = deposition fraction in head airways region

DF_{TB} = deposition fraction in tracheobronchial region

DF_{ALV} = deposition fraction in alveolar region

d_p = particle diameter, μm

Particle Clearance

Particles deposited in the head- and tracheobronchial regions are cleared primarily by the mucociliary escalator, in which the concerted action of cilia (hair-like structures) on the airway epithelial surface propels particles towards the larynx [38]. In addition, a large number of particles deposited in the alveolar region are phagocytized by macrophages [11], although literature suggests that effectiveness may be dependent on particle size. Phagocytosis will be discussed further in the following pages.

Interstitial Translocation

As mucociliary clearance and phagocytosis are not perfect defense mechanisms, particles not rapidly removed can translocate from the alveolar region into the interstitium (i.e., the tissue/space around the alveolar sacs) [57]. This is called *interstitial translocation*. Numerous studies have confirmed the existence of this translocation pathway across the alveolar epithelium and into the bloodstream. Research indicates that smaller particles (15 nm vs. 80 nm) had much higher interstitial translocation [63, 36]. A summary of various studies showed that uncoated particles up to at least 100 nm appear to undergo interstitial translocation [57].

For this research, a modifier called the interstitial translocation factor (ITF) was defined to specify a size range for which interstitial translocation occurs. A maximum size of 100 nm was used with a sloped line introduced between 100-150 nm to avoid discontinuity. See Figure 20 on the next page. ITF is multiplied by the translocation rate for diffusion between alveolar surface and alveolar blood.

3.2.1.2 Effects on Diffusion Between Blood and Tissue.

Nanoparticles traveling in systemic circulation must first exit through the endothelial walls of blood vessels to gain access to tissue, which is comprised of extracellular- and intracellular spaces (i.e., outside of- and within the cell, respectively). The endothelium is a thin layer of cells lining the interior of all blood vessels throughout the

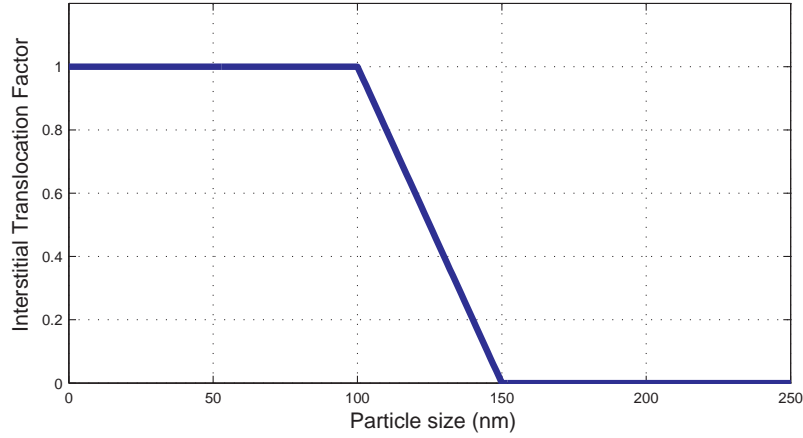


Figure 20. Interstitial translocation factor (ITF) (*inferred from [63, 36, 57]*)

body and forms a relatively smooth surface to facilitate blood flow. The endothelium is a type of *epithelial* tissue, which is one of four types of biological tissue found in animals (i.e., epithelial, connective, neural, and muscle tissue).

Most endothelium in the body is considered continuous, due to tight junctions between the endothelial cells and an underlying basement membrane. These tight junctions are gaps typically <2 nm wide, which serve as a physical barrier to impede passage of particles between endothelial cells (i.e., paracellular transport). However, the continuity of endothelial tissue varies from organ to organ, as demonstrated by the very tight junctions in the brain (i.e., blood-brain barrier) while the liver, which is fenestrated with pores of up to 100 nm, provides easier passage of material [8].

Figure 21 on the following page shows the hypothesized modifier called the “paracellular transport efficiency factor” (PTEF), which governs paracellular transport for diffusion between blood and tissue as shown in Equation 21 on page 67. It applies to all the organs in the model, except for liver and spleen which are fenestrated and will be discussed later.

PTEF is defined with ‘1’ representing maximum transport efficiency (i.e., nanoparticles are small enough to slip through the gaps) and ‘0’ representing large particles that cannot slip through gaps. A value of 2 nm was chosen as the threshold for the

PTEF modifier, based on the typical gap width discussed earlier. The PTEF modifier is assumed to be continuous, in order to acknowledge that the threshold size is not a precise value and that paracellular transport is not binary (i.e., completely on or completely off).

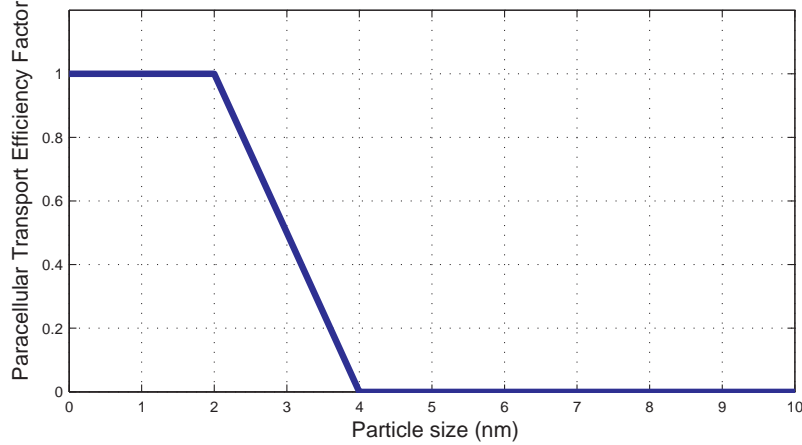


Figure 21. Paracellular transport efficiency factor (PTEF) (*inferred from [8]*)

Besides the paracellular route, particles can also pass *through* the cells via the transcellular route [18]. Transcytosis, which combines the processes of materials entering, transiting, and then exiting a cell, is believed to be size-dependent with smaller particles passing through the cell more easily than larger particles [20]. Few data exist describing the effect of particle size on overall transcytosis rates, but research suggests that nano-sized particles more readily enter cells and cellular organelles than larger particles [47].

Although there is a lack of quantitative information on the overall transcytosis process (i.e, entering + transiting + exiting a cell), the ‘entering’ portion of the process is fairly well-documented [22, 27, 35] and is known as endocytosis. Many articles conclude that particles <100 nm are necessary for endocytosis to occur efficiently, but more recent evidence by Garnett and Kallinteri concluded that sizes “in the hundreds” of nanometers range undergo efficient uptake into cells [20]. As the authors did not specify a discrete value for an upper threshold, a value of 500 nm was chosen to define

a modifier called a “transcytosis efficiency factor” (TEF). See Figure 22. Note that a sloped line was introduced between 500-600 nm to avoid discontinuity.

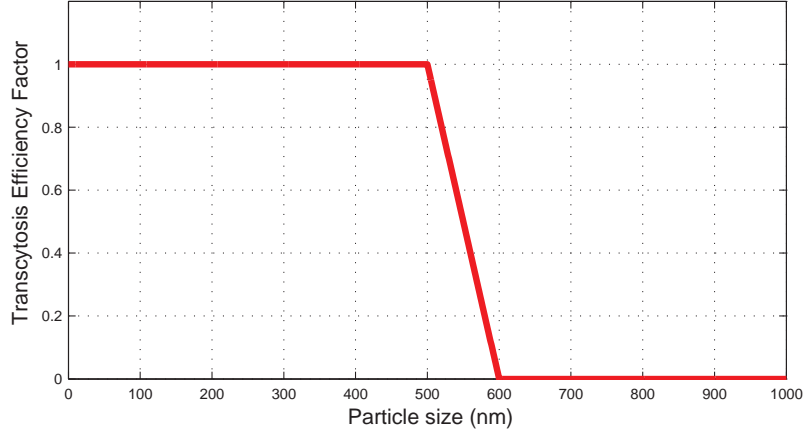


Figure 22. Transcytosis efficiency factor (TEF) (*inferred from [20]*)

For the purposes of blood-to-extracellular (i.e., blood-to-tissue) transport, we consider diffusion to be the combined effect of both the paracellular and transcytosis processes. The original diffusion equation presented in Section 2.2.1 on page 20 is rewritten to include both the paracellular and transcytosis modifiers, which modify the transfer coefficient, $T_{b:t}$. See Equation 21. At sizes <10 nm, both processes are in effect, thereby increasing diffusion. At sizes 10-600 nm, only transcytosis applies and above that size range diffusion of nanoparticles does not occur.

$$\text{Modified Blood:Tissue Diffusion Rate} = (\text{PTEF} + \text{TEF}) \cdot T_{b:t} \cdot \left(C_{\text{blood}} - \frac{C_{\text{extra}}}{P_{t:b}} \right) \quad (21)$$

where

P_{TEF} = paracellular transport efficiency factor (unitless)

TEF = transcytosis efficiency factor (unitless)

$T_{b:t}$ = transfer coefficient, blood-to-tissue (liters/hour)

C_{blood} = concentration in blood (#particles/liter)

C_{extra} = concentration in extracellular (#particles/liter)

$P_{t:b}$ = partition coefficient from tissue-to-blood (unitless)

Liver-Specific Phenomena

For diffusion between blood and tissue in any organ, it is assumed that paracellular transport (i.e., between cells) and transcellular transport (i.e., through cells) occur. But as discussed earlier, the continuity of blood vessel endothelium varies organ to organ. Both the liver and spleen have fenestrations (pores) which in theory, allow particles to cross out of blood and into tissue. See Figure 23. Research shows that the liver allows materials up to 100 nm to pass through the endothelial wall into extracellular space [20].

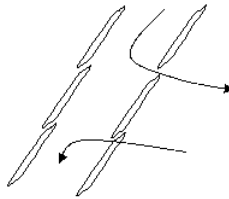


Figure 23. Diagram of fenestrations in blood vessels, (*adapted from Garnett*) [19]

Another unique feature involves the concept of “cell trapping”, in which particles that are large enough are sequestered in tissue. This mechanical filtration is not clearly explained in the literature but appears to be a function of organ construction

and microcirculation, with particles becoming trapped inside the tissue as blood must pass through the sinusoid walls to exit into venous bloodflow. Being “trapped” inside tissue appears to imply that foreign material is sequestered (i.e., prevented from transport away from the organ in venous blood) and subsequently faces phagocytosis. Because of organ construction, the spleen tends to be involved in clearance of larger particles (>250 nm diameter), while the liver clears smaller particles [18].

These two features are discussed in the literature as reasons why the liver (and spleen) are effective in removing nanoparticles from circulation, with most articles mentioning only one of the two possible explanations. This raises question on whether removal of particles from circulation by the liver (and the spleen) is governed by a maximum or minimum size limit [71]. Unlike most researchers, Stolnik et al., acknowledge *both* the filtration/cell trapping and fenestration theories and describes how there appears to be a narrow size range for prolonged circulation of a pharmaceutical drug carrier [71]. To model this effect, the maximum and minimum sizes must be specified. For the maximum size for escape through fenestrations, a value of 100 nm was chosen, based on Garnett and Kallinteri [20].

As no minimum size could be found in the literature, a value of 200 nm was chosen as it provides for the narrow size range phenomena described by Stolnik, et al. [71]. This value appropriately reflects that the liver is involved with clearing smaller particles than the spleen, which Garnett concluded will trap particles >250 nm [18]. Combining the two thresholds (i.e., 100 nm and 200 nm), a new modifier called the liver accumulation factor (LAF) was formed. See Figure 24 on the following page.

Note that in the narrow size range of 100-200 nm, the LAF plot suggests that nanoparticles have decreased accumulation. Conversely, at sizes below and above that range, particles will have increased accumulation in tissue (i.e., removal from systemic circulation). To avoid having points of discontinuity between y-values of 0

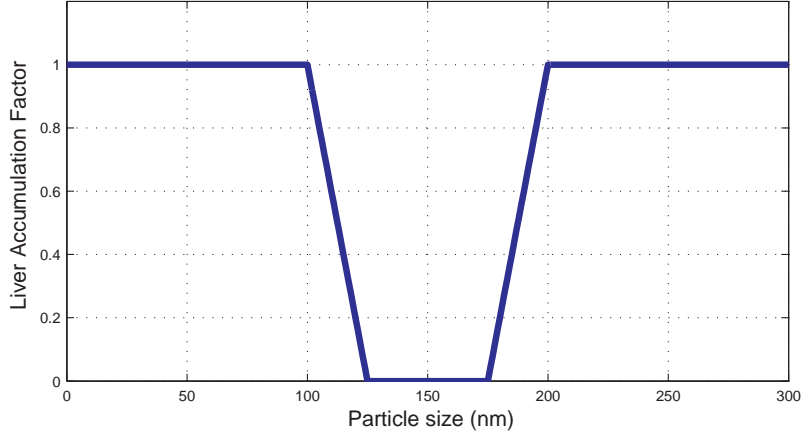


Figure 24. Liver accumulation factor (LAF) (*inferred from [71, 20]*)

and 1 (i.e., step-down and step-up functions), more gradual transitions (sloped lines) were inserted.

For the liver, LAF replaces the default paracellular modifier, PTEF, and is added to the transcytosis modifier, TEF, as shown in Equation 22. The result is that the fenestrations allow particles larger than the 2 nm threshold discussed earlier to leave blood and enter tissue. At sizes greater than >200 nm, trapping occurs which causes particle accumulation and decreased ability to return to blood (venous flow). Transcytosis occurs over a large range of particle sizes, up to the threshold of 500 nm.

$$\text{Modified Liver Diffusion Rate} = (\text{LAF} + \text{TEF}) \cdot T_{\text{b:t}} \cdot \left(C_{\text{blood}} - \frac{C_{\text{extra}}}{P_{\text{t:b}}} \right) \quad (22)$$

where

LAF = liver accumulation factor (unitless)

TEF = transcytosis efficiency factor (unitless)

$T_{b:t}$ = transfer coefficient, blood-to-tissue (liters/hour)

C_{blood} = concentration in blood (#particles/liter)

C_{extra} = concentration in extracellular (#particles/liter)

$P_{t:b}$ = partition coefficient from tissue-to-blood (unitless)

Spleen-Specific Phenomena

Similar to the liver, it is assumed that accumulation of nanoparticles in the spleen occurs above and below minimum and maximum size thresholds as the spleen also is fenestrated and has cell trapping. But compared to the liver, the spleen tends to clear larger particles from circulation as its discontinuous vascular endothelium has larger fenestrations, which allow even larger particles to pass through [20]. For a maximum size, Champion et al., defines a size threshold of 100 nm diameter, below which particles are able to exit blood vessels through fenestrations in the endothelial walls [10]. Conversely, Garnett concludes that particles >250 nm are effectively trapped [18] and this value serves as the minimum size threshold.

To accommodate the cell trapping and fenestration theories simultaneously, a spleen accumulation factor (SPAF) was defined using the two thresholds described above. See Figure 25 on the following page. This factor is applied between spleen blood and extracellular and replaces the paracellular modifier, PTEF. It is added to the transcytosis modifier, TEF. See Equation 31 on page 108. At sizes greater than >250 nm, particles tend to accumulate in extracellular and are, in theory, less likely to return to blood (venous flow).

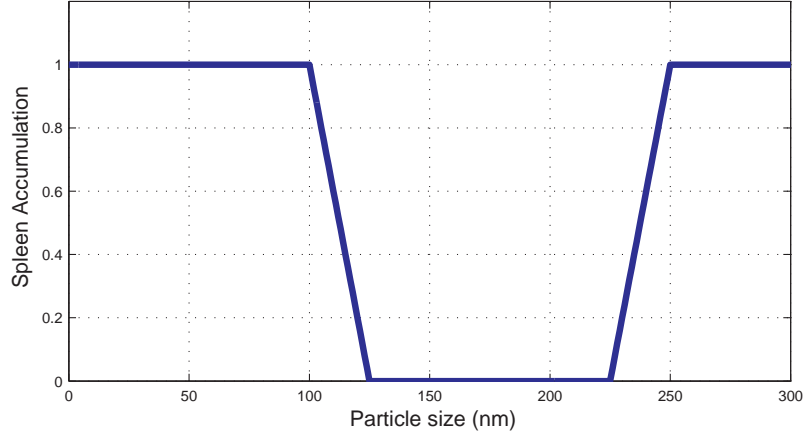


Figure 25. Spleen accumulation factor (SPAF) (*inferred from [10, 18]*)

$$\text{Modified Spleen Diffusion Rate} = (\text{SPAF} + \text{TEF}) \cdot T_{\text{b:t}} \cdot \left(C_{\text{blood}} - \frac{C_{\text{extra}}}{P_{\text{t:b}}} \right) \quad (23)$$

where

SPAF = spleen accumulation factor (unitless)

TEF = transcytosis efficiency factor (unitless)

$T_{\text{b:t}}$ = transfer coefficient, blood-to-tissue (liters/hour)

C_{blood} = concentration in blood (#particles/liter)

C_{extra} = concentration in extracellular (#particles/liter)

$P_{\text{t:b}}$ = partition coefficient from tissue-to-blood (unitless)

Kidney-Specific Phenomena

As described in Section 3.2 on page 60, a simplifying assumption used for the model derived in Phase I of the research was that 20% of nanoparticles in the blood entering the kidneys undergo glomerular filtration and renal clearance by excretion

via urine. This was based on the fact that approximately 20% of arterial blood flowing to the kidney undergoes glomerular filtration, with the remaining 80% returning to circulation [16].

However, glomerular filtration is highly selective with respect to particle size and has a size threshold of approximately 5-6 nm diameter [63]. For this phase of research, a modifier called the kidney filtration efficiency factor (KFEF) was defined, with a value of 6 nm used as the maximum size for nanoparticles to undergo glomerular filtration. A gradual transition (sloped line) was inserted between 6-8 nm to avoid having a discontinuity in the piecewise linear modifier. At or above 8 nm, it is assumed that no nanoparticles are removed via glomerular filtration, thereby eliminating renal clearance via urine. See Figure 26.

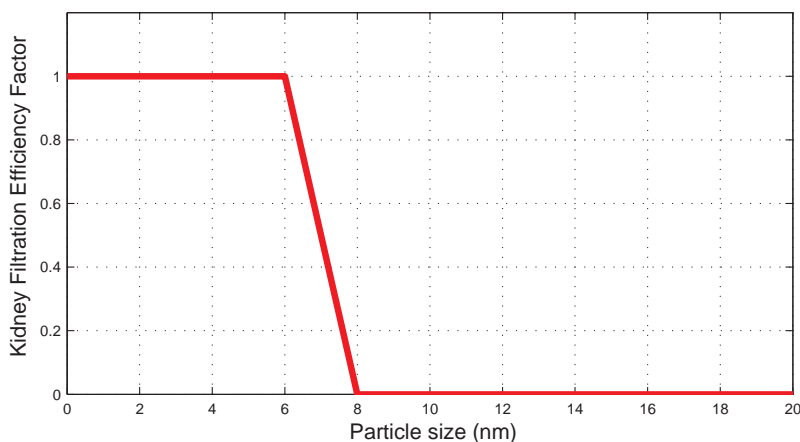


Figure 26. Kidney filtration efficiency factor (KFEF) (*inferred from [63]*)

Brain-Specific Phenomena

The blood-brain barrier controls the passage of various substances from systemic circulation into the central nervous system, CNS. Considerable literature exists that states in various terms that the brain has “very tight junctions” in its endothelium, effectively eliminating the paracellular route for the brain. However, few authors attempt to quantify the size of these tight junctions. Since it was stated previously that the gaps between endothelial cells in the other organs are approximately 2 nm

[8], then the premise that BBB junctions are more “tight” warrants assigning a small gap size, such as 1 nm. See Figure 27.

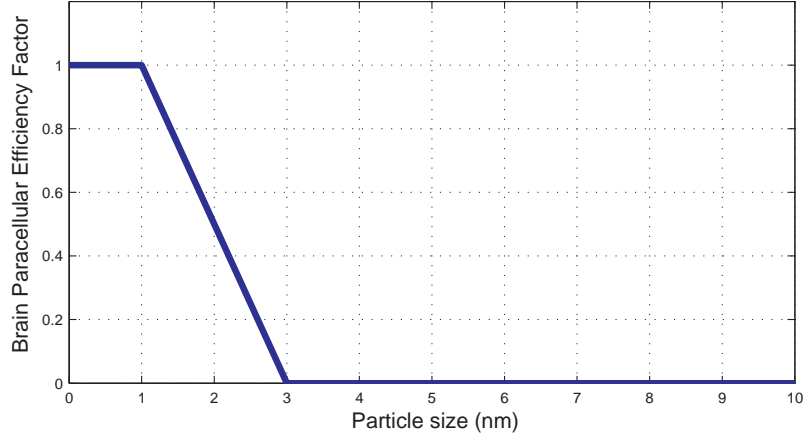


Figure 27. Brain paracellular efficiency factor (BPEF) (*inferred from [8]*)

For the brain transcellular route, it is assumed that the same biokinetics apply as described for the transcytosis efficiency factor (TEF). Substituting BPEF for PTEF, the diffusion rate for the brain (blood-to-tissue) can be rewritten as shown in Equation 24.

$$\text{Modified Brain Diffusion Rate} = (\text{BPEF} + \text{TEF}) \cdot T \cdot \left(C_{\text{blood}} - \frac{C_{\text{extra}}}{P_{\text{t:b}}} \right) \quad (24)$$

where

BPEF = brain paracellular efficiency factor (unitless)

TEF = transcytosis efficiency factor (unitless)

T = transfer coefficient (liters/hour)

C_{blood} = concentration in blood (#particles/liter)

C_{extra} = concentration in extracellular (#particles/liter)

$P_{\text{t:b}}$ = partition coefficient from tissue-to-blood (unitless)

Inflammation, either naturally occurring or due to properties of the nanoparticles, can cause “leaky” endothelium which allows materials into the tissue [18]. In addition, the manipulation of nanoparticle pharmaceuticals for specific targeting of the brain would likely present interesting results for the model. Both of these phenomena, although interesting, are beyond the scope of this research.

3.2.1.3 Effects on Phagocytosis.

The reticuloendothelial system, which includes the liver, spleen, and lymph nodes [63], contains high concentrations of phagocytic cells which can remove foreign material, including nanoparticles. As phagocytosis is part of the endocytosis family of cellular transport processes and due to the lack of additional data, the modifier used to describe transcytosis (which involves endocytosis) in Section 3.2.1.2 on page 64 was used. See Figure 28 on the next page. The modifier, relabeled as the phagocytosis size factor (PSF), is applied to the three sites for macrophages in the PBPK model (i.e., lungs, liver, and spleen).

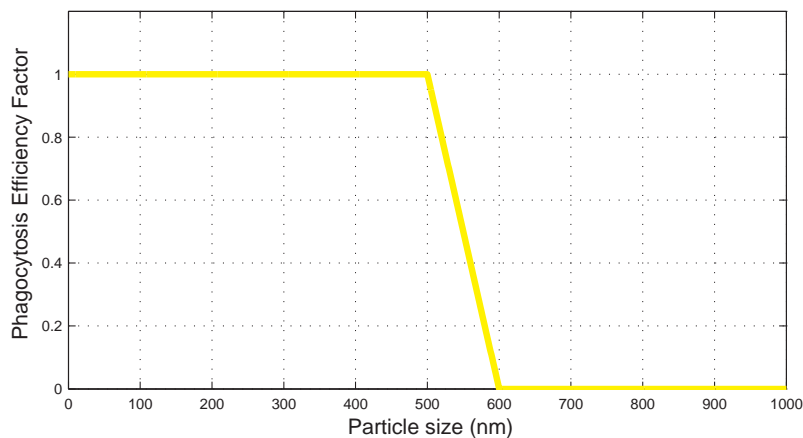


Figure 28. Phagocytosis size factor (PSF) (*inferred from [8]*)

3.2.1.4 Effects on Diffusion Between Extracellular and Intracellular.

Exiting the blood circulatory system implies that nanoparticles have entered the extracellular environment, where spaces between cells are filled with an aqueous gel-like material [20]. Once in the extracellular environment, particles may undergo uptake into cells through endocytic processes. As described earlier, recent evidence by Garnett and Kallinteri concluded that sizes “in the hundreds” of nanometers range undergo efficient uptake into cells [20]. As no upper threshold was specified, a value of 500 nm was chosen to define the threshold for a modifier called a “cellular uptake efficiency factor” (CUEF). See Figure 29 on the following page. CUEF is applied to $T_{e,i}$, $V_{\max at}$, $V_{\max cnt1}$, and $V_{\max cnt2}$ to modify the transport rates for diffusion, active transport, and carrier mediated transport.

3.2.2 Shape-Related Effects.

Although it seems likely that particle shape will affect deposition, toxicity, and fate of nanoparticles in the body, minimal research has been performed to describe such behavior [31]. However, it is believed that departing from spherical shapes

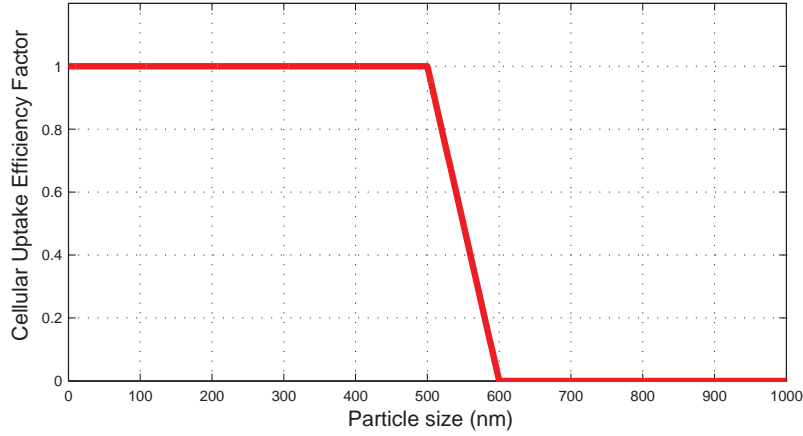


Figure 29. Cellular uptake efficiency factor (CUEF) (*inferred from [20]*)

usually leads to decreased internalization of the particles into the cell, hence increased biopersistence. A new modifier called the cellular uptake shape factor (CUSF) was defined, where a value of ‘1’ indicates the ideal shape, presumed to be spherical. See Figure 30.

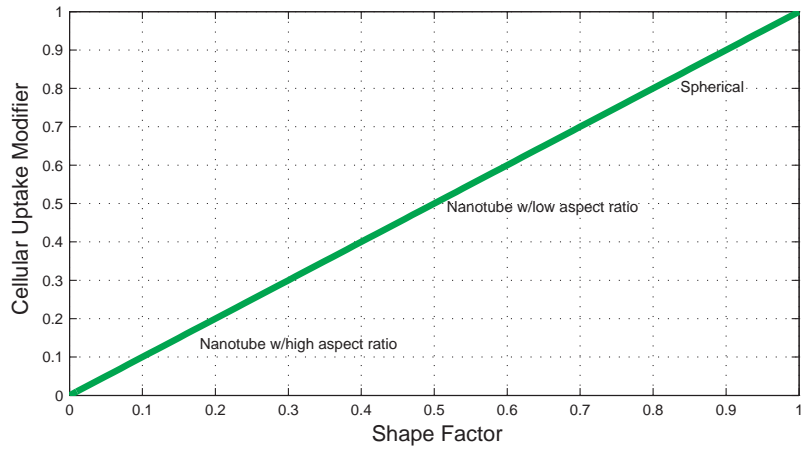


Figure 30. Cellular uptake shape factor (CUSF)

Although qualitative, the purpose of this modifier, which ranges from 0 to 1, is to explore how various shapes can affect model behavior due to inhibition of nanoparticle cellular uptake. CUSF is applied against $T_{b:t}$, $T_{e:i}$, V_{maxat} , $V_{maxcnt1}$, and $V_{maxcnt2}$, as it is assumed that shape can affect diffusion (e.g., how easily particles move through gaps), active transport, and carrier mediated transport. The various mathematical

equations representing these processes are therefore multiplied by the CUSF modifier to reflect diminished rates of transport when particle shape departs from the ideal case, which is assumed to be spherical.

Note that internalization is also dependent on particle orientation and mechanical stiffness. For example, red blood cells are flat and fairly large at 10 μm , but can fit between cells if oriented correctly and due to their relative flexibility. Similar to the discussion earlier on including knowledge from pharmaceutical interaction with the brain, these particle orientation/mechanical stiffness phenomena will likely provide interesting results, but are beyond the scope of this research.

3.2.3 Surface Coating Effects.

3.2.3.1 Effects on Phagocytosis.

Phagocytosis is governed by both particle size and surface treatments. In general, particles tend to have relatively hydrophobic surfaces and various blood proteins will bind strongly to those surfaces [18]. Uncoated hydrophobic particles are typically cleared from the bloodstream by the reticuloendothelial (i.e., phagocytic) system, while more hydrophilic particles remain in circulation longer [72, 49, 73].

Phagocytosis by the major organs of the reticuloendothelial system (RES) is regulated by the presence and balance between two groups of blood components (i.e., plasma proteins). The first component, opsonins, promote phagocytosis. The second component, dysopsonins, work to suppress the process. Opsonins are proteinaceous components of blood that adsorb onto particle surfaces or cells, effectively making foreign material more attractive to phagocytes [71]. Opsonins do not appear to be essential for phagocytosis to occur, but the process is significantly slower in their absence [18]. By the addition of specific hydrophilic coatings, the opsonin plasma proteins can be repelled which leaves the nanoparticles “invisible” to phagocytes [50].

The addition of surface coatings using polyethylene glycol (i.e., “pegylation”), or other hydrophilic surface coatings, to nanoparticles tends to increase the half-lives of nanoparticles in circulation [18]. Macrophages, such as those in the liver and spleen, are effective in removing opsonized particles, but coating particles with hydrophilic polymers such as polyethylene glycol (PEG) can reduce opsonization [20, 49]. This leads to reduced rates of phagocytosis and prolonged circulation in blood. Pharmaceutical research has long focused on developing hydrophilic, non-ionic polymers (i.e., coatings) for nano-sized drugs to suppress opsonins by preventing their adsorption onto particle surfaces [72], thus avoiding drug elimination by phagocytes and increasing the drug stability. For the pharmaceutical industry, premature removal of nano-sized drugs or carriers transporting drugs by macrophages is highly undesirable.

Changing the amount or characteristics of the surface coating layer can affect the biodistribution [18], e.g., a less dense PEG layer may provide less effective protection against phagocytosis. A modifier called the phagocytosis coating factor (PCF) representing the effects of coatings on phagocytosis was created. A value of ‘1’ indicates a lipophilic (i.e., hydrophobic) coating specially designed to allow nanoparticles to evade phagocytosis (e.g., PEG). Values less than ‘1’ indicates less-than-perfect evasion, such as other coatings providing decreased evasion capability, or less dense coatings. See Figure 31 on the following page. PCF is applied against the phagocytosis processes in the lungs, liver, and spleen.

3.2.4 Surface Charge Effects.

Research suggests that negative or neutrally charged small particles may undergo higher accumulation in the liver, spleen, or lung [63]. Evidence also suggests that negative charge on particles leads to increased interaction with the reticuloendothelial system (i.e., macrophages), thereby reducing the amount excreted in the kidneys [63].

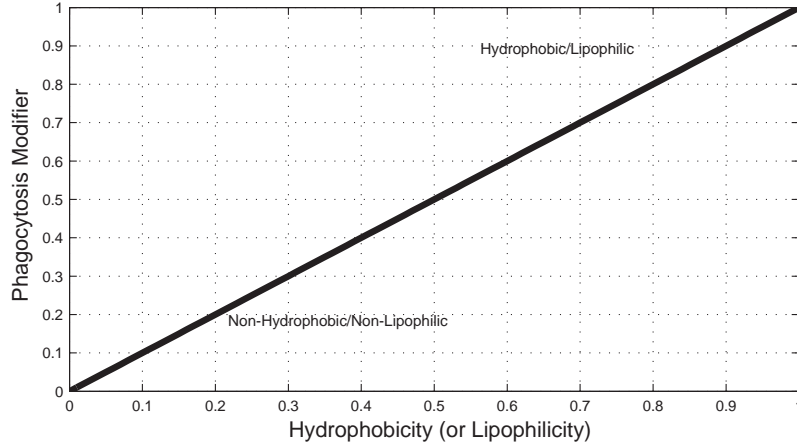


Figure 31. Phagocytosis coating factor (PCF) (*inferred from [18, 20, 49, 72]*)

Similarly, research suggests that neutral and low concentration anionic (negatively-charged) nanoparticles can translocate across the BBB, while cationic (positively-charged) particles do not [54].

In contrast, the kidney glomerular membrane favors *positively* charged molecules, which pass through the membrane more easily than uncharged molecules [80, 63]. Note that the glomerulus is both a size- and charge-selective filtration mechanism.

Without additional analysis available describing whether negative or positive charge is responsible for increased translocation/accumulation, it is hypothesized that zeta potential (a measure of *difference* in charge) is perhaps a more appropriate measure. Tabata, et al., concluded that surface charge of hydrophilic particles has a great effect on phagocytosis since particles with large zeta potential (i.e., high charge differences) exhibit enhanced phagocytosis [73].

Therefore, a charge-related modifier called the “surface charge factor” (SCF) was defined, as shown in Figure 32 on the next page. A value of ‘1’ indicates high zeta potential (i.e., more likely to undergo translocation and cellular uptake in the intracellular space) and ‘0’ indicates low zeta potential (i.e., less likely to undergo uptake in intracellular space). This modifier affects both the $T_{b:t}$ and $T_{e:i}$ transfer coefficients, which govern diffusion between blood/tissue and extracellular/intracellular,

respectively. It also affects the phagocytosis processes.

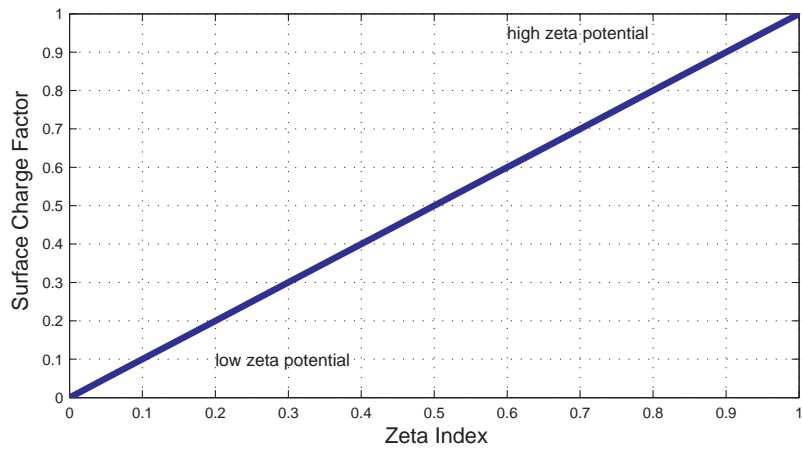


Figure 32. Surface charge factor (SCF) (*inferred from [63, 54, 80, 73]*)

3.3 Phase III: Defining a New Paradigm for Nano Risk Analysis

“At present, we lack a model to predict hazard or safety just based on the physicochemical characteristics of new nanomaterials that can be used for risk assessment or for safe product design.” - G. Oberdörster, et al. [58]

A 2008 North Atlantic Treaty Organization (NATO) workshop to evaluate the wide-scale implications (both positive and negative) of the use of nanomaterials on human health and the environment showed that attendees agreed that while existing chemical risk assessment may provide a starting point, the unique properties of nanomaterials adds considerable complexity to the issue [44]. With the impracticality of systematically determining individual dose-response curves for nanoparticles of every material, shape, size, coating, etc., a new paradigm is necessary for nanoparticle risk assessment.

As diffusion, settling, and agglomeration of particles is dependent on particle size, shape, and charge, so too is cellular dose [74]. Teeguarden et al., describes how the definition of dose for nanoparticles is a more dynamic, more complicated, and less comparable across particle types than it is for soluble chemicals [74]. More research is necessary to improve understanding on how these physico-chemical characteristics impacts dose. In addition, mounting evidence that these properties may impact dose is reason for the scientific community to consider possibly redefining the term ‘dose’ as it relates to risk assessment. This ‘new paradigm’ would likely deviate from the commonly used dose metric of mg/kg/day scaling on the x-axis of the dose-response curve, as it is more than simply the ‘amount’ (i.e., mass or # count, etc.) of nanomaterials that determines adverse effects (‘response’).

3.3.1 The Approach.

To begin defining the new paradigm, first recognize that risk analysis for nanoparticles is a multi-dimensional problem as nanomaterial dose is likely a function of size, shape, surface coating, and surface charge due to the recurring emphasis in the literature. Simulations which include the physico-chemical modifiers described in Phase II of research (Section 3.2 on page 60) are used to calculate the area under the curve (AUC) for arterial blood concentration vs. time. Arterial blood is an appropriate sub-compartment to study as it is the source of nanoparticles which flow to the various organs.

The First Mean Value Theorem for Integration states that the solution to integrating a function $f(t)$ over an interval $[a, b]$ is $f(c) \cdot (b - a)$, where $f(c)$ represents an average value of $f(t)$ over the interval [82]. In the context of this research, AUC equals the average concentration in the subcompartment multiplied by length of time. Dividing average concentration by volume of the subcompartment yields an average amount in the subcompartment, which is proportional to the dose to the subcompartment. Therefore, AUC is used as a surrogate of dose (i.e., total nanoparticle exposure to the subcompartment over a given time period). AUC is in units of concentration-time.

Mean Value Theorem for Integration: For all $t \in [a, b]$, there exists $c \in (a, b)$ such that:

$$\int_a^b f(t) dt = f(c)(b - a) \quad (25)$$

Afterwards, a multiple regression (actually, multiple *linear* regression) is performed on dose as the dependent (criterion) variable, with size, shape, surface coating, and surface charge as the independent (predictor) variables. Note that the source rate (i.e., inhalation rate of nanoparticles into the body) was kept constant at 500 (x1000

particles/liter). Varying the source rate was not part of this research, but increasing or decreasing the source will likely scale the concentration plots, although not necessarily in a linear manner due to the presence of the nonlinear Michaelis-Menten saturable processes.

Multiple regression differs from simple linear (bivariate) regression as there is more than one independent variable involved. It is assumed that all four independent variables are continuous, not categorical. The result of multiple regression is a *regression equation* of the form shown in Equation 26. The regression coefficients, β_i , indicate how the dependent variable, \hat{Y} , changes with each unit of change in an independent variable, x_i [42].

$$\hat{Y} = \alpha + \beta_1 x_1 + \beta_2 x_2 + \dots + \beta_n x_n \quad (26)$$

where

\hat{Y} = predicted value of the dependent (criterion) variable

α = intercept value (a constant)

β_i = multiple regression coefficient, corresponding to variable x_i

x_i = independent (predictor) variable

Usually ordinary least squares (OLS) or the maximum likelihood method is used to calculate the regression coefficients. OLS applies to the linear situation only (linear relationship between dependent and independent variables), while maximum likelihood can be used in either situation [42].

An adequately large sample size (i.e, number of simulations) is necessary so that the regression equation possesses sufficient statistical power to detect a significant

effect. A general rule of thumb frequently cited in research is to use $n > 50 + 8 \cdot m$, where n =sample size and m =# of independent (predictor) variables [24, 83]. For this research, $m=4$ which yields a recommended sample size of $n > 82$. As running additional ‘samples’ for this simulation-based research only adds a few minutes of computational time when using MATLAB[®], a randomized sample size of $n=3000$ was used.

3.3.1.1 Multiple Regression Assumptions.

Several key assumptions for multiple regression are listed below. Non-linear regression (e.g., logistic regression) is necessary when the linear regression does not meet these assumptions [42].

- A linear relationship between dependent and independent variables.[42]
- Normality: each independent (predictor) variable has a normal distribution [42]
- Homoscedasticity: variance is constant across all levels of the predicted (dependent or criterion) variable [42], i.e., the same level of relationship throughout the range of the independent variable

In general, it is possible for the number of independent variables to outnumber the number of predictors, but in this case, all four independent variables are used as predictors. Note that for larger sets of independent variables, various methods exist to identify the most relevant predictor variables that should be included in the regression equation (e.g., forward selection, backward elimination, stepwise selection) [42].

3.3.1.2 Specific Steps for Phase III.

The specific steps to be followed for Phase III of the research are:

- (1) Random distribution: Use random number generator in MATLAB[®] to randomize size, shape, surface coating, and surface charge to develop a list of simulations
- (2) Run these simulations through the MATLAB[®] model with diffusion in parallel with active- and carrier-mediated transport
- (3) Calculate concentration vs. time for the arterial blood subcompartment
- (4) Calculate AUC, using the trapezoidal rule, over the entire simulation time (i.e., t=200 hours).
- (5) Export size, shape, surface coating, surface charge, and AUC as an .xls file for import into SAS JMP[®]
- (6) Perform a multiple linear regression on AUC (i.e., a surrogate of dose or total exposure) as a function of size, shape, surface coating, and surface charge to derive the regression equation
- (7) Analyze goodness-of-fit and summary statistics

IV. Results and Analysis

“I have not failed. I’ve just found 10,000 ways that won’t work.”

- Thomas A. Edison

Clearly, improving our understanding of the biokinetics and distribution of nanoparticles in humans is essential to advancing risk assessment for nanoparticle exposures. The ultimate goal of the dissertation research is to determine one or more broad conclusions that will provide a significant contribution to the nanoparticle risk assessment field. This would include any conclusions drawn that would help form a new paradigm for risk assessment of nanoparticles, such as the impracticality of attempting to derive an all-encompassing set of dose-response curves to cover all types of nanoparticles, under all exposure scenarios.

Unlike chemicals, which are considered homogeneous for a given formulation, nanoparticles sharing the same core material (e.g., silver nanoparticles) can be of countless sizes, shapes, surface charge, surface areas, surface coatings, etc. These differences, however subtle, may have significant impact on toxicity.

Therefore, it seems obvious that the number of resulting dose-response curves would be staggering and unrealistic to attempt to gather. For this dissertation, there were three distinct phases of research: Model Formulation, Inclusion of Physico-Chemical Properties, and Defining a New Paradigm for Nano Risk Analysis. Results for the phases will be summarized in the paragraphs to follow.

4.1 Phase I: Model Formulation Results

The full PBPK model that resulted from Phase I is shown in Appendix B on page 126. This model was used for the range finding exercise described below and was also the basis for Phases II and III of the research. A listing of the ODEs that

comprise the PBPK model is in Appendix C on page 134.

4.1.1 Range Finding Results.

4.1.1.1 Summary of Range Finding Exercise.

Early in the research, it was decided that the most important parameters to focus range finding on were $T_{b:t}$, $T_{e:i}$, $V_{\max at}$, $V_{\max cmt1}$, and $V_{\max cmt2}$. These parameters govern transport between either blood and extracellular (i.e., tissue) or extracellular and intracellular space. Identifying *suitable* values for the key transport parameters in the model which govern cellular transport was the focus, not *precision*. It should be noted that the methodology followed does not avoid the need for future laboratory research on parameterization and perhaps the results presented in the dissertation underscore the importance of pursuing such research. Table 7 is a summary of the values selected from the range finding exercise described in Section 3.1.4 on page 48. A more detailed discussion of these findings follows.

Table 7. Range finding results

Physiological Parameter	Variable	Value Chosen (x1000 particles/hour)
Transfer Coefficient, blood-to-tissue	$T_{b:t}$	5
Transfer Coefficient, extra-to-intracellular	$T_{e:i}$	0.05
Active Transport, Max Rate of Transport	$V_{\max at}$	0.5
Carrier Mediated Transport, Max Rate of Transport1	$V_{\max cmt1}$	0.5
Carrier Mediated Transport, Max Rate of Transport2	$V_{\max cmt2}$	0.5

4.1.1.2 Instantaneous Equilibration Results.

For IE, a single compartment is used to represent the entire organ/tissue group. Tissue concentration is calculated by dividing the amount of nanoparticles in the compartment by organ volume. Then, the tissue concentration is divided by the tissue:blood partition coefficient to determine venous blood concentration. A simplifying assumption used for IE is that the tissue blood volume is considered negligible. Higher blood flow rates and smaller volumes tend to cause higher concentrations, with loss mechanisms affecting concentrations also. Figure 33 shows a summary of instantaneous equilibration. The nanoparticle concentrations in tissue (assuming IE) for the various organs are shown in Figure 34.

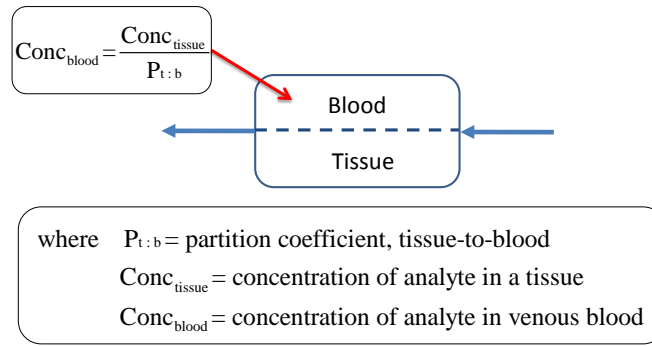


Figure 33. Instantaneous equilibration model

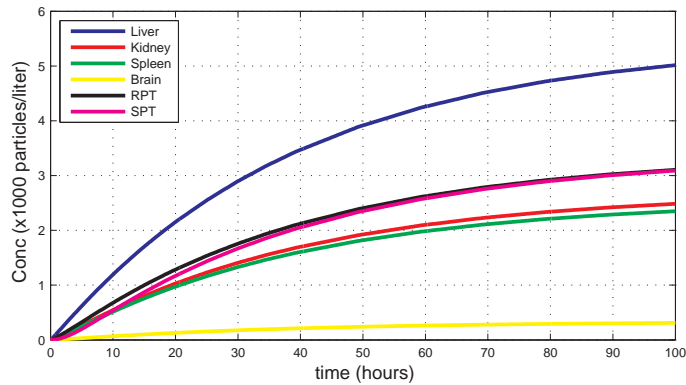


Figure 34. Nanoparticle concentrations for IE

The behavior seen in Figure 34, is primarily influenced by blood flow rates (Q),

organ volumes (V), and loss mechanisms. The order of the organs from largest to smallest fraction of cardiac output, Q_{frac} is: 1) Liver 2) Kidneys 3) RPT 4) GI 5) SPT 6) Brain 7) Spleen. The order from largest to smallest volume is: 1) SPT 2) Liver 3) RPT 4) Brain 5) Kidneys 6) Spleen.

The liver dominates primarily due to its large Q , as it receives inflow from both arterial blood and portal circulation (i.e., GI tract and the spleen). The kidney has similarly large Q , but much smaller V . This would tend to cause higher concentrations as concentration $\propto 1/\text{volume}$, but it has a significant loss mechanism to urine which serves to lower concentrations. The spleen has a very small volume, which leads to moderately high concentration. RPT and SPT have moderately high concentrations also, primarily due to the lack of loss mechanisms. Finally, the brain has relatively low concentration, due to low Q and high V , plus the assumed limiting factor of 10% transport across the blood-brain barrier.

4.1.1.3 Range Finding for $T_{\text{b:t}}$.

As described in Section 3.1.4.1 on page 49, the goal is to find a single value of $T_{\text{b:t}}$ that can be used across all organs. The baseline for the $T_{\text{b:t}}$ range finding is the nanoparticle concentration resulting from an assumption of instantaneous equilibration, as shown in Figure 34 on the previous page. Now, the single compartment representing an organ is split into two subcompartments (tissue and blood), with diffusion inserted between the two subcompartments. See Figure 35.

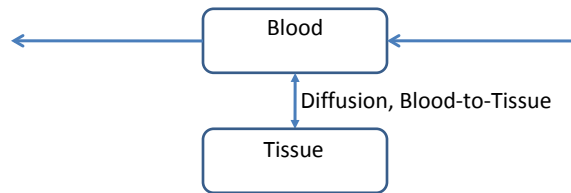


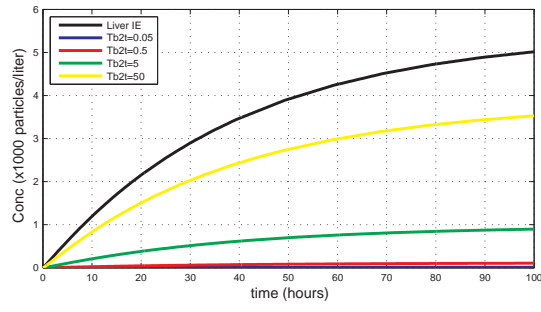
Figure 35. Two-subcompartment model for $T_{\text{b:t}}$ range-finding

Figure 36 on the next page shows the baseline concentrations using IE (black lines) and the new concentrations as $T_{b:t}$ is varied from 0.05 to 50 for each organ. The liver, spleen, brain, and RPT demonstrate similar behavior, with concentration increasing as $T_{b:t}$ increases. Differences between the plots are attributable to differences in blood flow rates, tissue volumes, and loss mechanisms. Note that the total tissue concentration *is not* the arithmetic sum of extra- and intracellular concentrations. Instead, it equals the sum of the amounts divided by total volume, $(\text{amount}_{\text{extra}} + \text{amount}_{\text{intra}})/(V_{\text{extra}} + V_{\text{intra}})$.

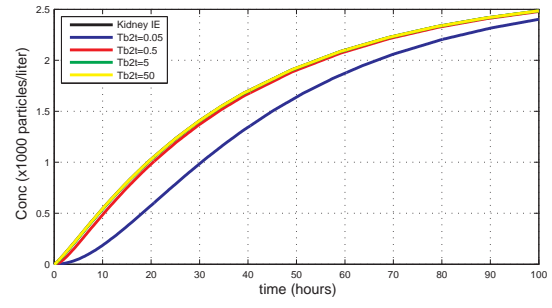
As shown in Figure 36b on the following page, the kidney presents slightly different behavior than the other organs. At $T_{b:t} \geq 0.5$, the nanoparticle concentration in kidney tissue approaches that for IE. This rapid approach to steady state is likely influenced by the modeling assumption that a considerable fraction of nanoparticles goes to urine (20%) and 80% of blood bypasses the glomerular filtration process of the kidney nephrons. The larger magnitude for kidney concentration is likely due to the kidney having a relatively small volume (0.3 liters) and concentration $\propto 1/\text{volume}$.

Slowly perfused tissue also presents different behavior. See Figure 36f on the next page. Concentration in SPT does not rise significantly as $T_{b:t}$ is increased as seen in the other organs, due to the extremely large tissue volume (64 liters) which is an order of magnitude greater than the next largest organ.

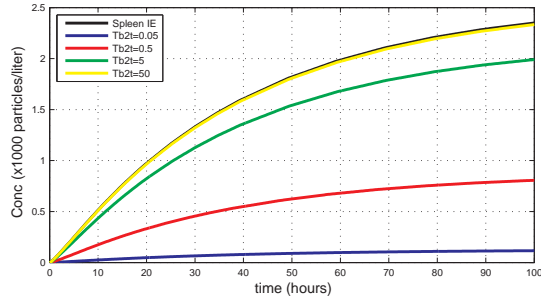
After reviewing these plots, it is clear that any value for $T_{b:t}$ on the range of 0.5 to 50 keeps the organ concentrations bounded by IE. Therefore, the value chosen for $T_{b:t}$ was 5, which keeps four of the six organs approximately midrange between the upper bound of IE and zero. Figure 37 shows the resulting concentrations for the organs when $T_{b:t}=5$ is inserted into the model.



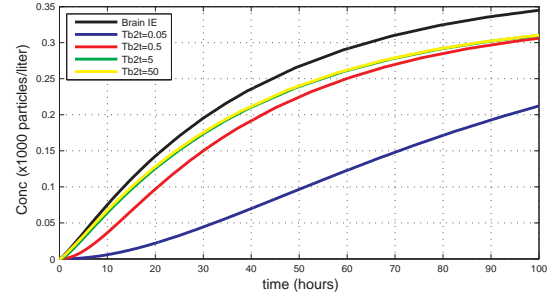
(a) Liver



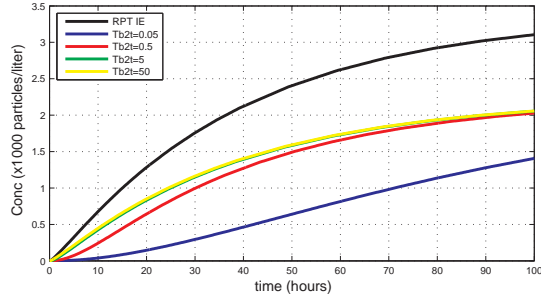
(b) Kidneys



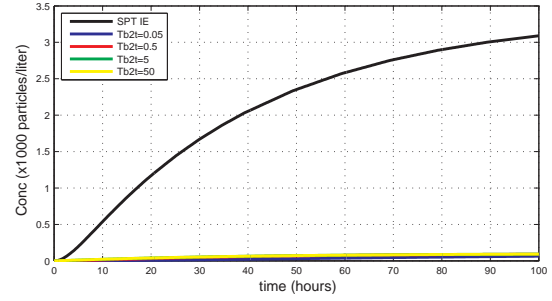
(c) Spleen



(d) Brain



(e) Richly Perfused



(f) Slowly Perfused

Figure 36. Nanoparticle concentrations for $T_{b:t}$ range finding

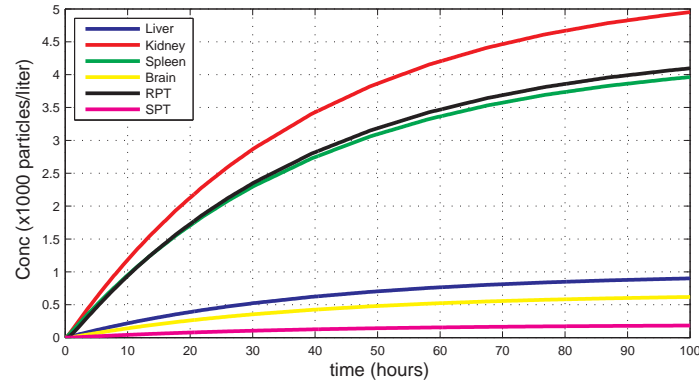


Figure 37. Tissue nanoparticle concentrations for $T_{b:t}=5$

4.1.1.4 Range Finding for $T_{e:i}$.

Range finding for $T_{e:i}$ is conducted by using the three-subcompartment representation shown in Figure 38 with the tissue portion of each organ now split into extracellular and intracellular subcompartments.

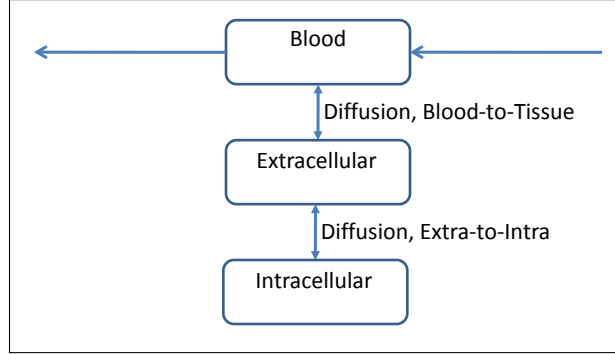
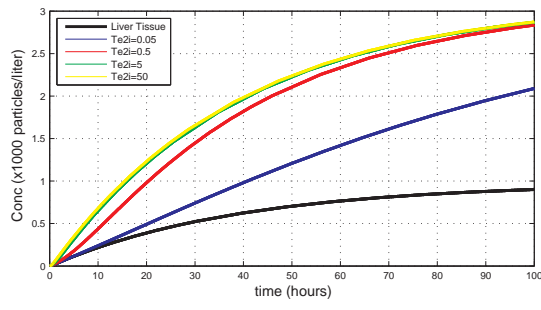


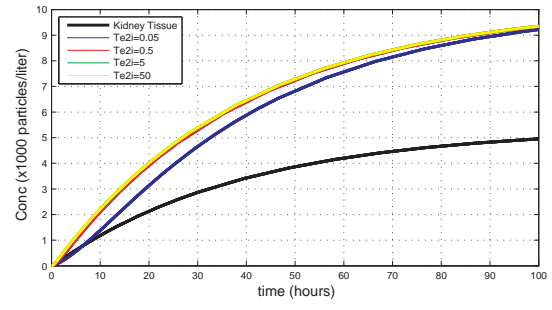
Figure 38. Three-subcompartment model for $T_{e:i}$ range-finding

The range finding results showed that the different organs all behave similarly in response to varying $T_{e:i}$ over the range 0.05 to 50. Larger values of $T_{e:i}$ lead to a faster approach to steady state. A value of $T_{e:i}=0.05$ was chosen as this best keeps the resulting tissue concentrations across the organs to within $2\times$ the tissue concentrations determined using $T_{b:t}$.

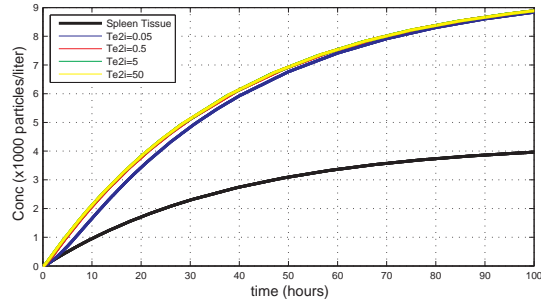
The resulting plot of concentrations for the organs when $T_{e:i} = 0.05$ is inserted into the model is shown in Figure 40.



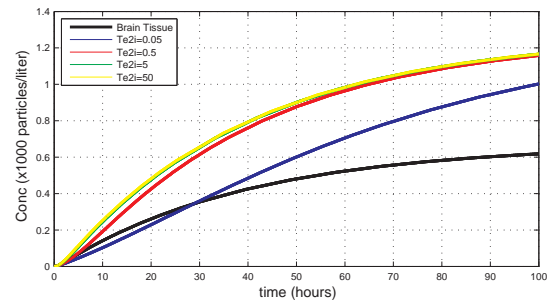
(a) Liver



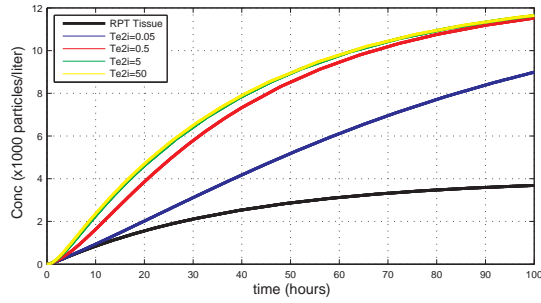
(b) Kidneys



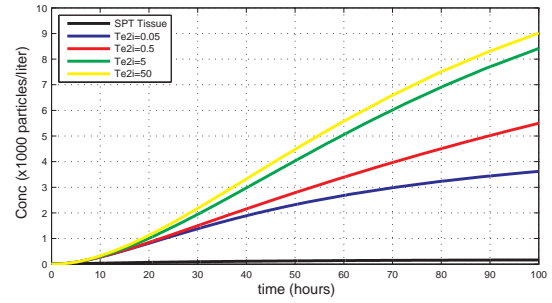
(c) Spleen



(d) Brain



(e) Richly Perfused



(f) Slowly Perfused

Figure 39. Nanoparticle concentrations for $T_{e,i}$ range finding

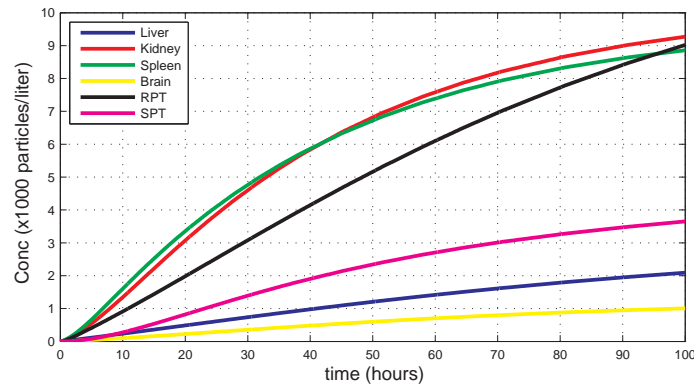


Figure 40. Tissue nanoparticle concentrations for $T_{e,i}=0.05$

4.1.1.5 Range Finding for V_{maxat} .

To determine the value for V_{maxat} , which is the Michaelis-Menten maximum rate for active transport between extracellular and intracellular, we use the results from the $T_{\text{e;i}}$ range-finding (i.e., diffusion between extra- and intracellular) as the baseline. This method relies on a three-subcompartment representation for each organ. For this simulation, active transport and diffusion work in parallel between extra- and intracellular subcompartments as shown in Figure 41.

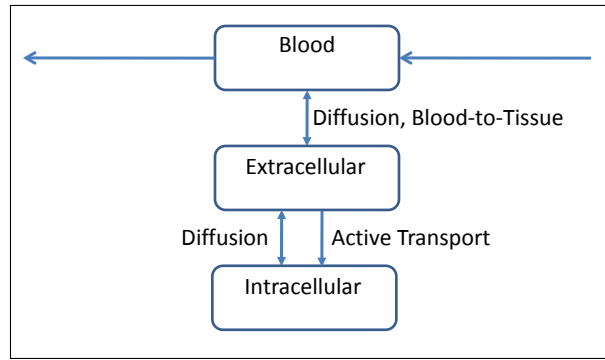


Figure 41. Three-subcompartment model for V_{maxat} range-finding

Figure 42 on the following page shows the baseline of tissue concentrations using $T_{\text{e;i}}$ (black lines) with new concentrations as V_{maxat} is varied from 0.05 to 50 for each organ. Results indicate that diffusion operating in parallel with the uni-directional active transport process appears to allow organ concentrations to approach steady state. Recall that without diffusion operating in parallel, there was a limitless buildup of nanoparticles in the intracellular subcompartment, as no loss/exit mechanism existed for the intracellular subcompartment. Such a limitless buildup is not realistic.

The various plots in Figure 42 on the next page indicate that $V_{\text{maxat}}=50$ leads to extremely high concentrations that are an order of magnitude larger than previously seen. Although diffusion is operating in parallel with active transport (between extracellular and intracellular), it appears that extremely high values for V_{maxat} allows the active transport portion to dominate (overcome) the effects of diffusion and much

higher accumulation in extracellular and intracellular occurs.

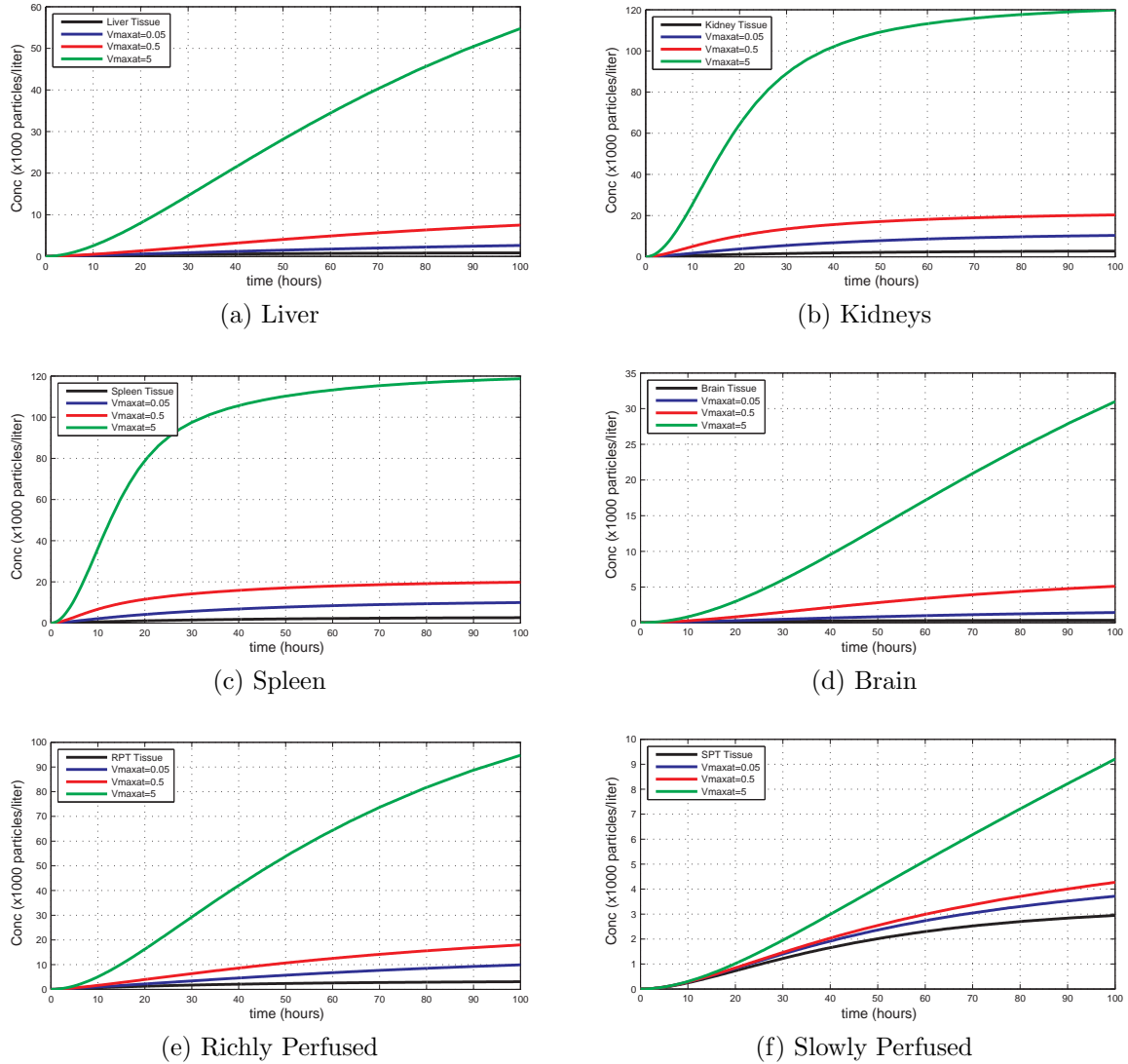


Figure 42. Nanoparticle concentrations for $V_{\max at}$ range finding

A value of 0.5 was chosen as it best keeps $V_{\max at}$ within $2\times$ the tissue concentrations using $T_{e,i}$, which is shown as the black line in Figure 42. The resulting plot of concentrations for the organs when $V_{\max at} = 0.5$ is inserted into the model is shown in Figure 43. This same value for $V_{\max at}$ is used as $V_{\max cnt1}$, as both represent saturable (Michaelis-Menten) terms in the extracellular-to-intracellular direction.

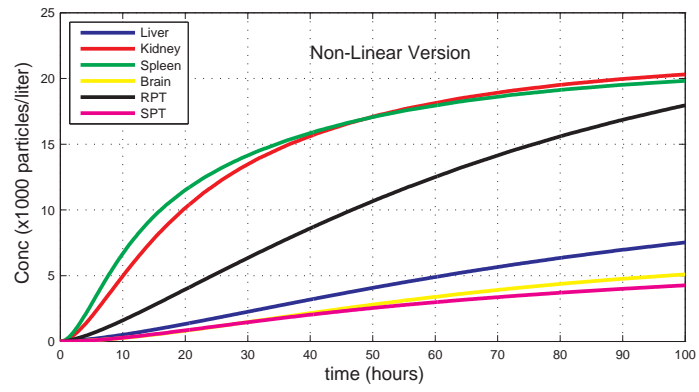


Figure 43. Tissue nanoparticle concentrations for $V_{\max at}=0.5$

4.1.1.6 Range Finding for V_{maxcmt2}

In the previous section (Section 4.1.1.5 on page 95), V_{max} for active transport, which goes from extra- to intracellular, was determined. Carrier mediated transport, however, is modeled using *two* sets of Michaelis-Menten constants (extra- to intracellular and intra- to extracellular), as shown in Equation 4 on page 23. The V_{max} determined for active transport is also used as V_{maxcmt1} , as both apply to the extra-to-intracellular direction. Therefore, range-finding is necessary only for V_{maxcmt2} , which is for the intra-to-extracellular (i.e., reverse) direction.

This method relies on a three-subcompartment representation for each organ, as shown in Figure 44, with carrier mediated transport and diffusion working in parallel between extra- and intracellular subcompartments.

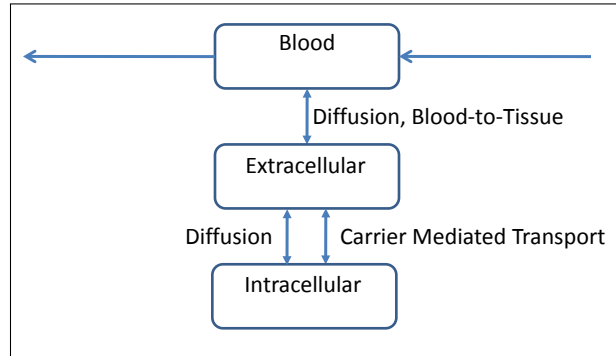
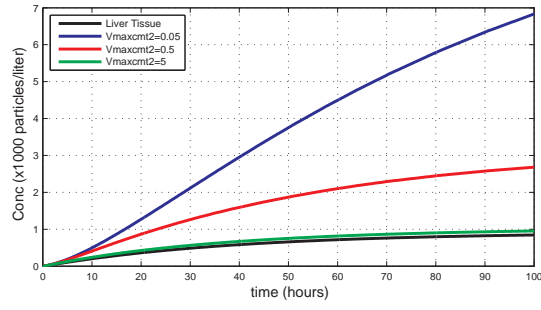


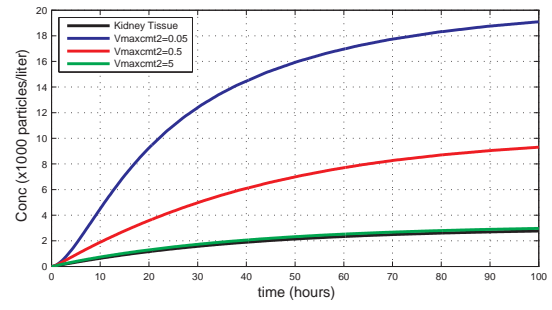
Figure 44. Three-subcompartment model for V_{maxcmt2} range-finding

Figure 45 on the following page shows the baseline with new concentrations as V_{maxcmt2} is varied from 0.05 to 5 for each organ. The plot behavior is very similar to that seen during V_{maxat} range finding. A value of 0.5 best keeps V_{maxcmt2} within $2\times$ the concentrations realized using T_{ei} .

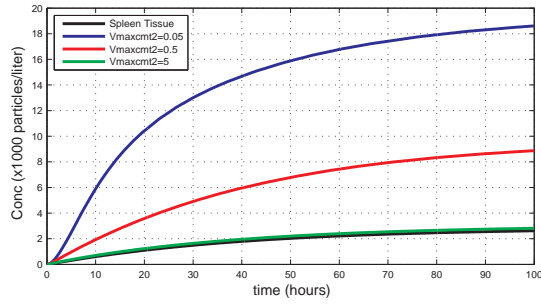
The resulting plot of concentrations for the organs when $V_{\text{maxcmt2}} = 0.5$ is inserted into the model is shown in Figure 46.



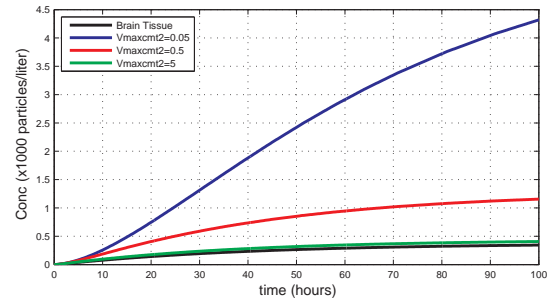
(a) Liver



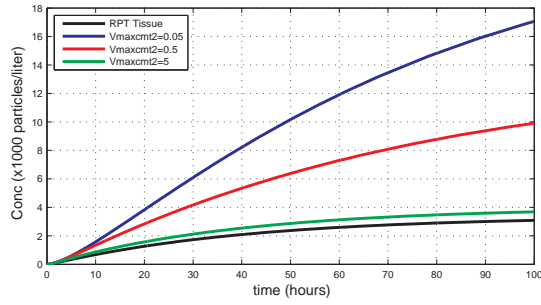
(b) Kidneys



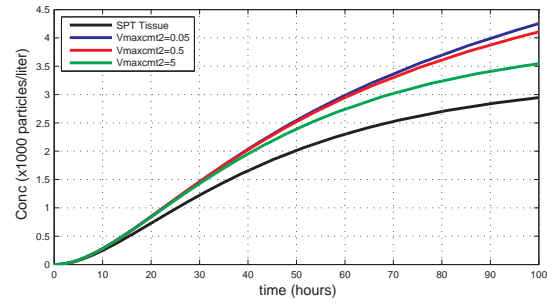
(c) Spleen



(d) Brain



(e) Richly Perfused



(f) Slowly Perfused

Figure 45. Nanoparticle concentrations for $V_{\max\text{cmt}2}$ range finding

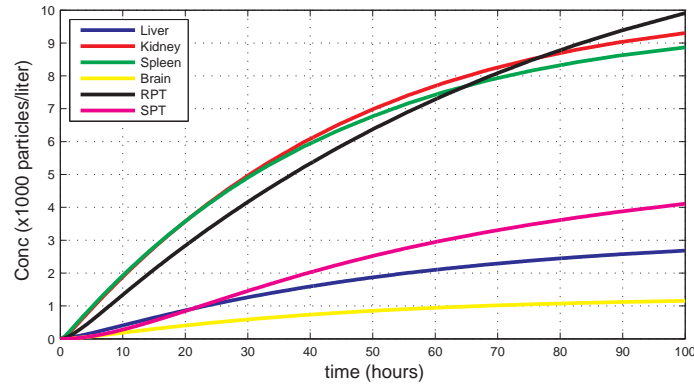
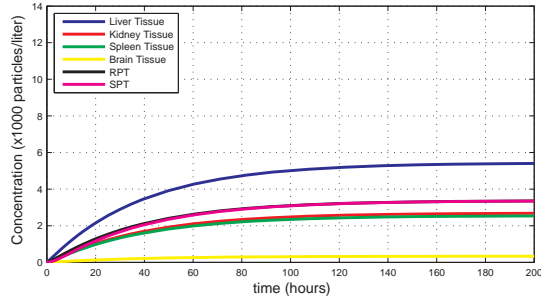


Figure 46. Tissue nanoparticle concentrations for $V_{\max\text{cmt}2}=0.5$

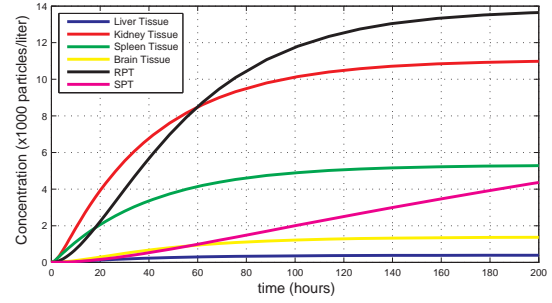
4.1.2 Comparison of Plots for Transport Processes.

After completing the range finding exercise in the previous section, the next step was to re-run the MATLAB[®] model to investigate how assumptions of active transport and carrier mediated transport affect nanoparticle concentrations in the organs, as compared to the traditional assumption of instantaneous equilibration. Note that both active- and carrier mediated transport operate between extracellular and intracellular, and both processes are assumed to operate with diffusion in parallel, as shown in Figures 41 on page 95 and 44 on page 98. Figure 47 on the next page shows the nanoparticle concentrations under various transport assumptions.

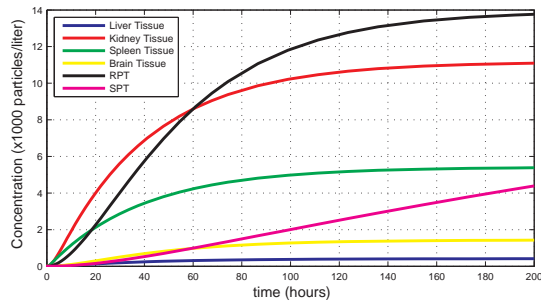
Figure 47b shows the concentration curves for the organs when diffusion is the process between extracellular and intracellular. In comparison, Figures 47c, 47d, and 47e show the concentrations if active+diffusion, carrier mediated+diffusion, or active+carrier+diffusion had been used. These three plots are nearly identical in appearance to the diffusion-only plot in Figure 47b, which indicates that diffusion likely dominates between extracellular and intracellular. Figure 47e is important to note, as this represents the final model formulation with diffusion operating in parallel with active transport and carrier mediated transport, as shown in Figure 48 on page 102.



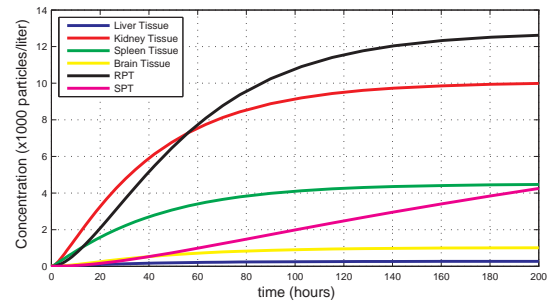
(a) Instantaneous equilibration



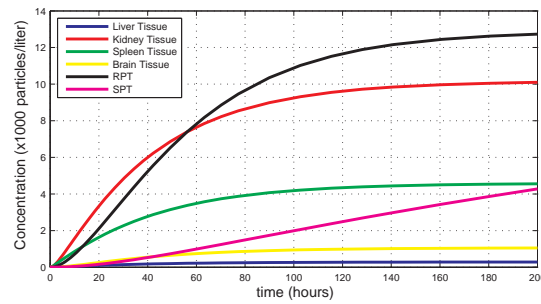
(b) Diffusion



(c) Active + Diffusion



(d) Carrier Med. + Diffusion



(e) Active + Carrier + Diffusion

Figure 47. Nanoparticle concentrations under various transport assumptions

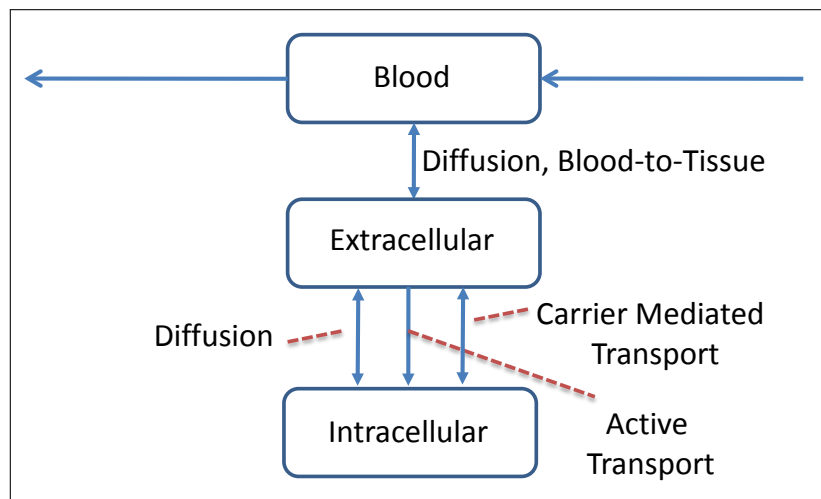


Figure 48. Example: final operational concept with diffusion in parallel with active and carrier mediated transport

4.1.3 Eigenvalue Analysis Results.

Eigenvalue analysis can be used to characterize the behavior of tissues as transport parameters are varied and provide powerful insight on how rapidly nanoparticle concentrations reach steady state. Large magnitude (negative) eigenvalues indicate fast buildup and small magnitude eigenvalues indicate slow buildup. As slow buildup implies slow decay, this may be of toxicological significance as this would lengthen the recovery time necessary between exposures. In the simulations presented here, eigenvalue analysis allows conclusions defining future research over a small number of simulations when it would otherwise take many simulations to reach the same conclusions.

Note that the representation of active- and carrier mediated transport using Michaelis-Menten kinetics prevents eigenvalue analysis from being conducted as there are nonlinear terms (i.e., concentration appears also in the denominator). See Equation 27. A simple solution to linearize the nonlinear Michaelis-Menten terms is to rewrite the equation into either the first order or zero-order approximations shown in Equation 28 on the following page.

$$\text{Active Transport Rate} = \frac{V_{\max} \cdot C}{K_m + C} \text{ (#particles/hour)} \quad (27)$$

where

$$V_{\max} = \text{max rate of transport (\#particles/hour)}$$

$$C = \text{concentration (\#particles/liter)}$$

$$K_m = \text{Michaelis-Menten constant (\#particles/liter)}$$

$$\text{Active Transport Rate} \approx \begin{cases} \frac{V_{\max} \cdot C}{K_m}, & C \ll K_m \\ V_{\max}, & K_m \ll C \end{cases} \quad (28)$$

For the first-order approximation, choosing a slope of V_{\max}/K_m is a good approximation at low concentrations, $C \ll K_m$, but is a poor approximation at higher concentrations. A better choice of slope is $V_{\max}/2/K_m$, which is the slope through the point with coordinates concentration= K_m and rate= $V_{\max}/2$, where K_m is defined as the concentration at $V_{\max}/2$. See Figure 49. The zero-order approximation is simply V_{\max} , which is the asymptote for the curve as it approaches steady state.

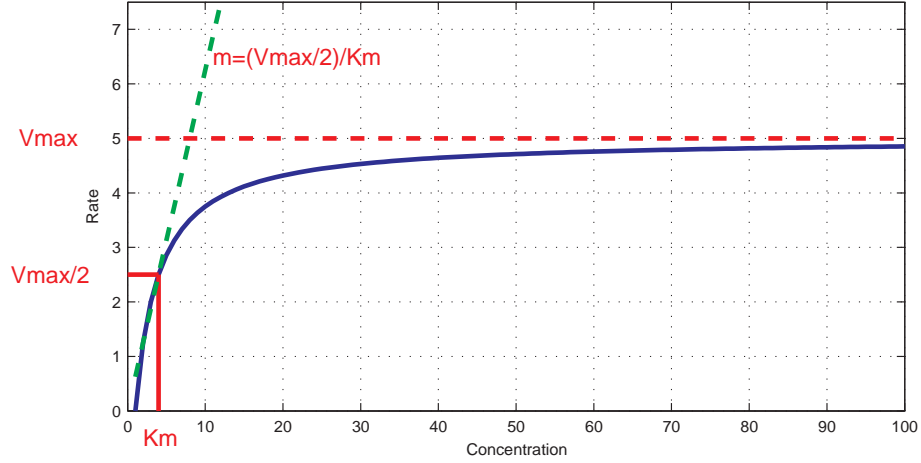


Figure 49. Example: first-order approximation of Michaelis-Menten kinetics

Figure 50a on the following page shows that linearizing the model using a first-order approximation of $V_{\max}/2/K_m$ and a zero-order approximation of V_{\max} provides results nearly identical to the nonlinear model shown in Figure 50b. This demonstrates how a nonlinear model, such as one with Michaelis-Menten saturable processes, can be linearized in order to enable eigenvalue analysis.

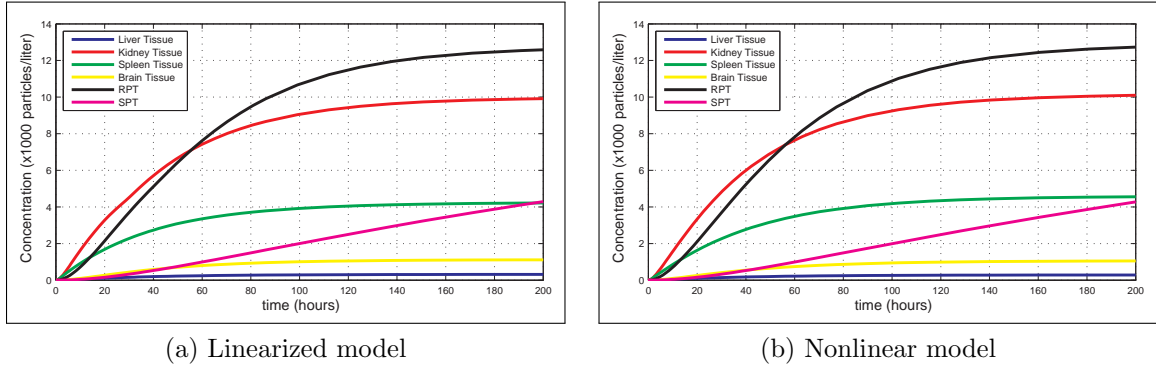


Figure 50. Comparison of the linearized and non-linear results

4.1.3.1 Eigenvalue Analysis of $T_{e:i}$.

The goal of this portion of the research is to demonstrate the concept of eigenvalue analysis. In the previous section, it was shown that linearizing the model using zero-order and first-order approximations provide results nearly identical to the nonlinear results. This, in theory, allows eigenvalue analysis of the nonlinear model by linearizing via either of these approximations. However, to demonstrate eigenvalue analysis $T_{e:i}$ was selected.

The matrices shown in Appendix F on page 176 represent the eigenstructure of the model as the transfer coefficient $T_{e:i}$ is varied. An index showing which rows correspond with each subcompartment is shown in Figure 81 on page 176. Each eigenstructure matrix has the eigenvalues listed in the top row above their associated eigenvectors. The columns have been sorted with the largest magnitude eigenvalues to the left side of the matrix. In the matrices that follow, any small terms in the eigenvectors (< 0.05) are shown as '0'. Each eigenvector was then normalized to the 1-norm format (L1-norm), where the sum of absolute values of the terms equals 1. This allows us to see the fractional contributions of specific organs to the various time scales (decay rates), represented by the eigenvalues, λ .

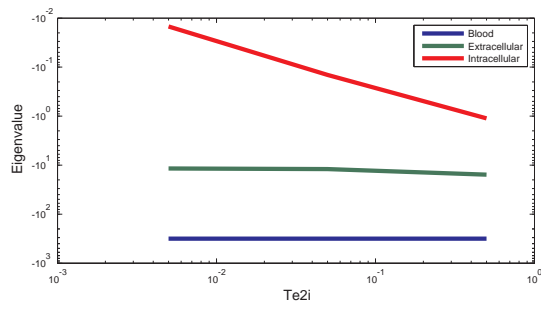
It was previously stated that eigenvalues can be linked to specific subcompartment-

ments. Doing so can be challenging, as a given subcompartment can contribute to multiple time scales (eigenvalues) which is indicated by more than one non-zero entry in a given row of the eigenstructure. In addition, contributions to a single time scale (eigenvalue) from different subcompartments can change as a parameter is varied. Because of these phenomena, it is necessary to study the set of eigenstructures as a parameter is varied, in order to deduce which eigenvalue corresponds to which subcompartment.

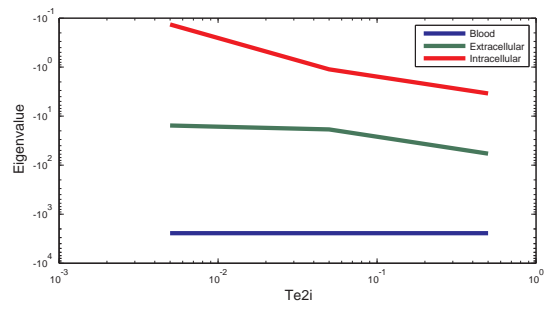
As a parameter is varied, some subcompartments display changes in their eigenvalues. Others may have relatively steady eigenvalues. A display of such behavior can be seen in Figure 51 on the next page. It is important to note that these plots are log-log scale, so sloped lines indicate rapidly (i.e., exponentially) changing eigenvalues.

Figure 51 shows that the blood subcompartments of the various organs (blue lines) show a rapid approach to steady state, as indicated by the large magnitude (negative) eigenvalues. The eigenvalues for the blood subcompartments remain relatively constant as the transport parameter $T_{e,i}$ is varied through the range 0.005 to 0.5. The extracellular subcompartments (green lines) show downward sloping behavior at the higher values of $T_{e,i}$, indicating a faster approach to steady state. Intracellular subcompartments (red lines) appear to respond to changes in eigenvalue behavior for extracellular. One conclusion that could be made is that fine-tuning the value of the diffusion transfer coefficient may be important, as eigenvalues can change greatly depending on $T_{e,i}$, which can lead to widely varying concentration results.

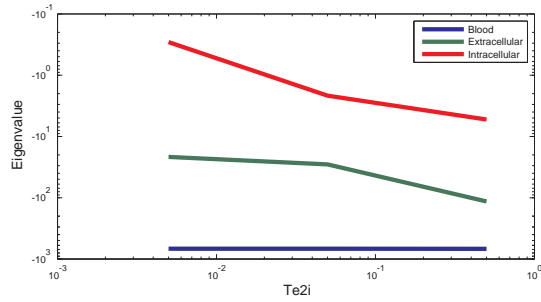
In Figure 52 on the following page, the eigenvalues for the lungs and GI tract subcompartments are unresponsive to variations in the transport parameter $T_{e,i}$ over the range 0.005 to 0.5. This indicates that pursuing precise values for $T_{e,i}$ will likely not affect behavior significantly in the lungs and GI tract and efforts may be better spent fine-tuning other transport parameters to further examine those organs.



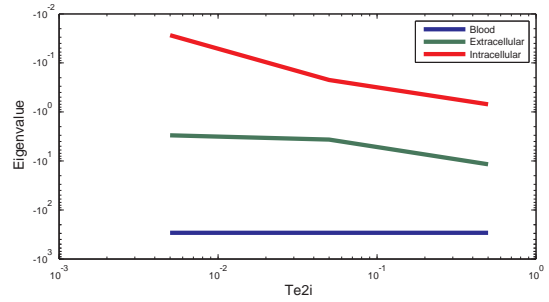
(a) Liver



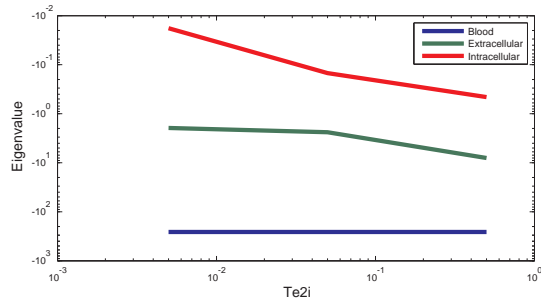
(b) Kidneys



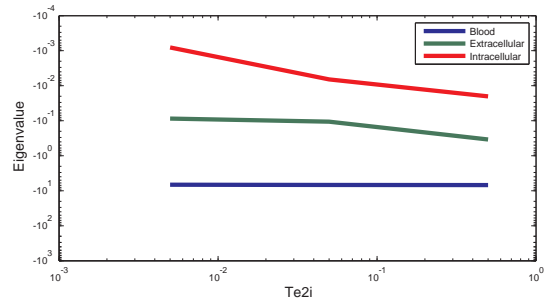
(c) Spleen



(d) Brain

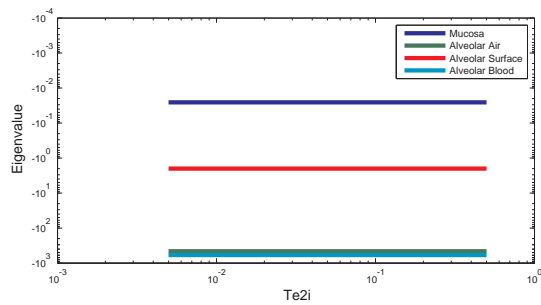


(e) Richly Perfused

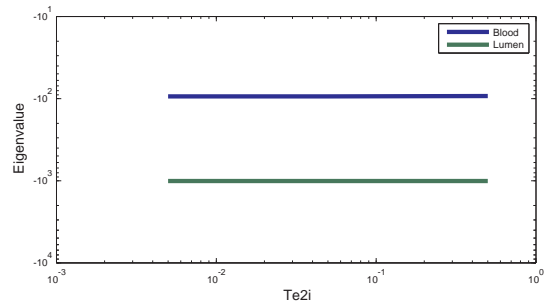


(f) Slowly Perfused

Figure 51. Eigenplots for the various organs



(a) Lungs



(b) GI Tract

Figure 52. Eigenplots for the lungs and GI tract

4.2 Phase II: Physico-Chemical Properties Results

4.2.1 Final Transport Equations.

Shown below are the key transport equations with the physico-chemical modifiers inserted. The MATLAB[®] code was modified to include these equations.

$$\text{B:T Diffusion Rate} = (\text{PTEF} + \text{TEF}) \cdot \text{SCF} \cdot \text{CUSF} \cdot T_{\text{b:t}} \cdot \left(C_{\text{blood}} - \frac{C_{\text{extra}}}{P_{\text{t:b}}} \right) \quad (29)$$

$$\text{Liver Diffusion Rate} = (\text{LAF} + \text{TEF}) \cdot \text{SCF} \cdot \text{CUSF} \cdot T_{\text{b:t}} \cdot \left(C_{\text{blood}} - \frac{C_{\text{extra}}}{P_{\text{t:b}}} \right) \quad (30)$$

$$\text{Spleen Diffusion Rate} = (\text{SPAF} + \text{TEF}) \cdot \text{SCF} \cdot \text{CUSF} \cdot T_{\text{b:t}} \cdot \left(C_{\text{blood}} - \frac{C_{\text{extra}}}{P_{\text{t:b}}} \right) \quad (31)$$

$$\text{Brain Diffusion Rate} = (\text{BPEF} + \text{TEF}) \cdot \text{SCF} \cdot \text{CUSF} \cdot T_{\text{b:t}} \cdot \left(C_{\text{blood}} - \frac{C_{\text{extra}}}{P_{\text{t:b}}} \right) \quad (32)$$

$$\text{E:I Diffusion Rate} = (\text{CUEF} \cdot \text{CUSF} \cdot \text{SCF}) \cdot T_{\text{b:t}} \cdot \left(C_{\text{blood}} - \frac{C_{\text{extra}}}{P_{\text{t:b}}} \right) \quad (33)$$

$$\text{Active Transport Rate} = \text{CUEF} \cdot \text{CUSF} \cdot \frac{V_{\text{maxat}} \cdot C_{\text{extra}}}{K_{\text{m}} + C_{\text{extra}}} \quad (34)$$

$$\text{Carrier Mediated Rate} = \text{CUEF} \cdot \text{CUSF} \cdot \left(\frac{V_{\text{maxcmt1}} \cdot C_{\text{extra}}}{K_{\text{mcmt1}} + C_{\text{extra}}} - \frac{V_{\text{maxcmt2}} \cdot C_{\text{intra}}}{K_{\text{mcmt2}} + C_{\text{intra}}} \right) \quad (35)$$

where

PTEF = paracellular transport efficiency factor (unitless)

TEF = transcytosis efficiency factor (unitless)

SCF = surface charge factor (unitless)

CUSF = cellular uptake shape factor (unitless)

LAF = liver accumulation factor (unitless)

SPAF = spleen accumulation factor (unitless)

BPEF = brain paracellular efficiency factor (unitless)

CUEF = cellular uptake efficiency factor (unitless)

$T_{b:t}$ = transfer coefficient, blood-to-tissue (liters/hour)

C_{blood} = concentration in blood (#particles/liter)

C_{extra} = concentration in extracellular (#particles/liter)

$P_{t:b}$ = partition coefficient from tissue-to-blood (unitless)

V_{max} = max rate of transport (#particles/hour)

K_m = Michaelis-Menten constant (#particles/liter)

Besides the transport equations listed above, the three locations of phagocytosis (i.e., lungs, liver, and spleen) also are affected by the addition of physico-chemical properties. Specifically, PCF and SCF are multiplied to the first-order rate constant to determine the surface coating- and charge-dependent rate of phagocytosis, as shown

in Equations 36, 37, and 38.

$$\text{Lung Phagocytosis Rate} = (\text{AM rate const} \cdot C) \cdot \text{PSF} \cdot \text{PCF} \cdot \text{SCF} \quad (36)$$

$$\text{Liver Phagocytosis Rate} = (\text{phagocytosis rate const} \cdot C) \cdot \text{PSF} \cdot \text{PCF} \cdot \text{SCF} \quad (37)$$

$$\text{Spleen Phagocytosis Rate} = (\text{phagocytosis rate const} \cdot C) \cdot \text{PSF} \cdot \text{PCF} \cdot \text{SCF} \quad (38)$$

where

AM =alveolar macrophage

C =concentration (#particles/liter)

PSF =phagocytosis size factor

PCF =phagocytosis coating factor

SCF =surface charge factor

4.2.2 Physico-Chemical Simulations.

Using the MATLAB[®] code which contains the modified transport equations that account for the physico-chemical properties, a set of simulations was conducted in order to calculate concentration vs. time and to support Phase III New Paradigm as discussed in Section 3.3.1 on page 83. 3000 simulations were conducted, with each simulation consisting of a combination of randomly-generated sizes, shapes, surface coatings, and surface charges using the ranges shown in Table 8 on the following page.

Table 8. Phase III physico-chemical properties simulations

Physico-Chemical Property	Range	Notes
Size	0 - 500 nm	extended beyond <i>engineered</i> nanoparticle range of <100 nm
Shape	0 - 1	‘1’= spherical
Surface Coating	0 - 1	‘1’= ideal coating
Surface Charge	0 - 1	‘1’= high zeta potential

Using MATLAB[®], area under the curve (AUC) was calculated for the arterial blood concentration after each simulation. A scatter plot showing area under the arterial blood concentration curve for each of the 3000 simulations is shown in Figure 53. Note that the majority of data points occur at area under the curve <100 (x1000 particles/liter×hours), with occasional values exceeding 600 (x1000 particles/liter×hours).

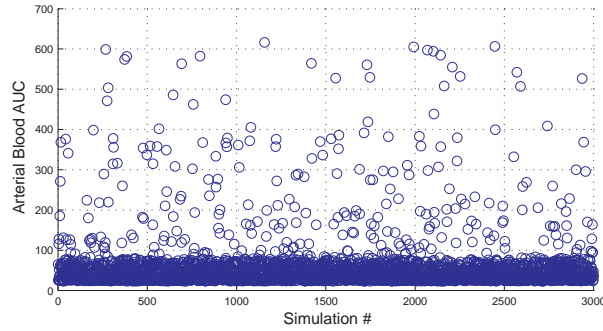


Figure 53. Scatter plot showing area under the curve (AUC) for the simulations

4.3 Phase III: New Paradigm Results

4.3.1 Multiple Regression Analysis.

After exporting the data to JMP[®], a regression equation was determined and is shown in Equation 39. Following the nomenclature described in Equation 26 on page 84, $\alpha=101.32$ is the intercept value and represents the predicted area under the arterial blood concentration curve when the independent variables are equal to zero. The β (regression) coefficients (rounded to -0.15, -10.87, +4.18, -2.74) represent the contributions of each independent parameter (size, shape, surface coating, surface charge, respectively) towards the predicted area under the curve. For example, $\beta_1=-0.15$ implies that a one-unit increase in ‘size’ is associated with a 0.15 decrease in area under the curve for arterial blood.

$$\begin{aligned} \text{AUC} = & 101.32 - 0.15 \cdot (\text{size}) - 10.87 \cdot (\text{shape}) + 4.18 \cdot (\text{surface coating}) \\ & - 2.74 \cdot (\text{surface charge}) \end{aligned} \quad (39)$$

where

AUC = predicted area under the curve (#particles/liter · hours)

size = nanoparticle size (range 0-500 nm)

shape = particle shape factor (range 0-1, unitless)

surface coating = surface coating factor (range 0-1, unitless)

surface charge = surface charge factor (range 0-1, unitless)

4.3.1.1 Goodness of Fit.

Diagnostic tests were run using the SAS JMP® statistical software to check the goodness of fit of the regression model to actual data. An $R^2=0.092$ indicates that only a very small portion of the variation of area under the arterial blood concentration curve (9.2%) is explained by variation in the independent variables [17]. A low R^2 implies that the model is poor at predicting the outcome variable, which is area under the arterial blood concentration curve. Clearly, using a linear regression model does not provide the best fit.

To further investigate the fitted equation, Figure 54 shows two different perspectives of a 3-dimensional scatter plot showing area under the curve, as size and shape are varied. Results indicate that area under the arterial blood concentration curve is dependent primarily on size, as indicated by the L-shaped behavior in Figure 54b. Shape has minimal influence on behavior as it simply extends the L-shaped behavior in the y-direction (i.e., “into the paper”), as shown in Figure 54a.

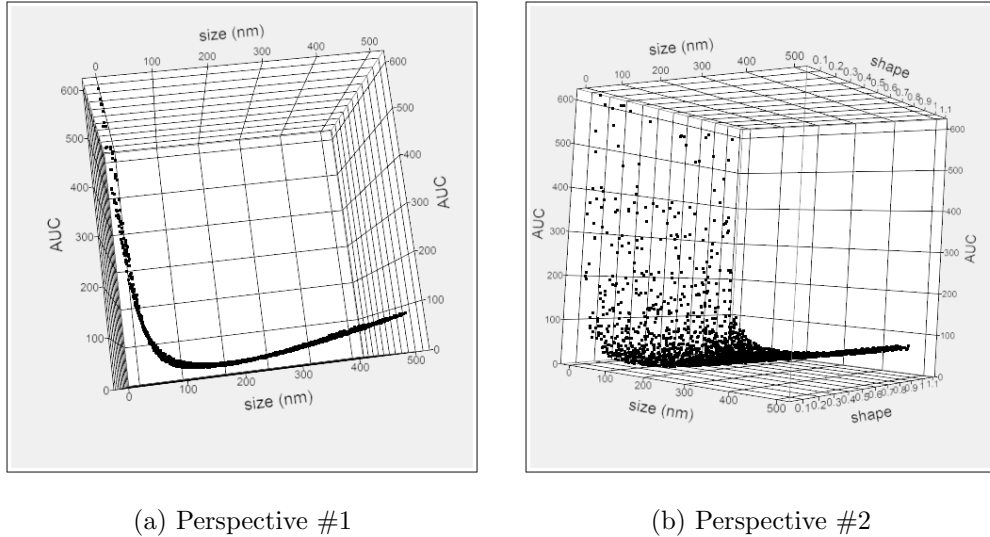
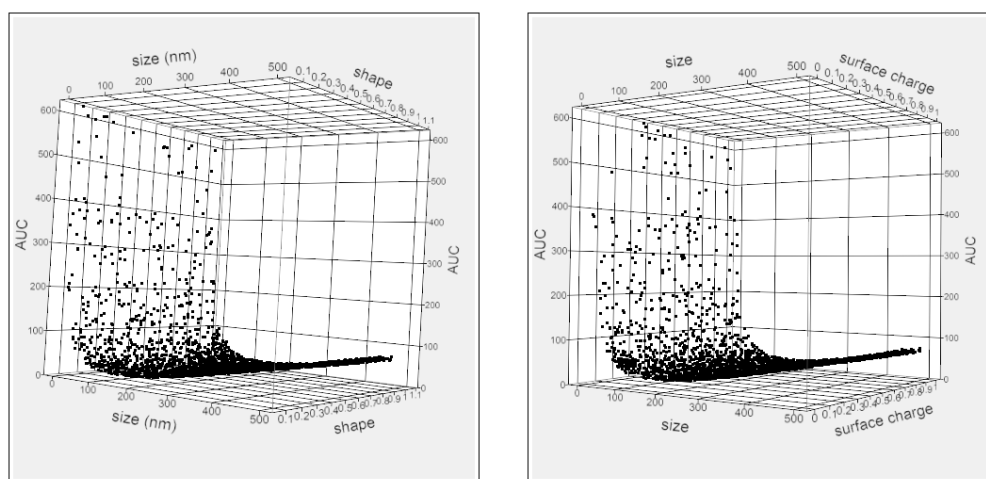


Figure 54. 3-d scatterplot of AUC vs. size vs. shape

This same size-only dependency (i.e., L-shaped behavior) can be seen when surface

coating and surface charge are substituted for shape and become the y-axis variable (“into the paper”) as shown in Figure 55. In Section 3.3.1 on page 83, an assumption of linearity was stated as a necessary condition for linear regression, but performing the bivariate scatter plots for each of the independent variables versus the dependent variable reveals that curvature (non-linearity) occurs for area under the curve vs. size. See Figure 54 on the preceding page and Figure 55. Therefore, the assumption of linearity is incorrect.



(a) AUC vs. size vs. surface coating

(b) AUC vs. size vs. surface charge

Figure 55. 3-d scatterplot of AUC vs. size vs. surface coating and surface charge

To understand why area under the arterial blood concentration curve is mainly a function of size, recall that the majority of physico-chemical modifiers were size-related and were distributed in numerous sites in the PBPK model. For example, size determines lung deposition, interstitial translocation, and is critical to all the transport processes, etc. Shape is also prevalent, whereas surface coating and charge are not. In fact, surface coating is only a factor for the three sites of phagocytosis.

In Figure 56 on the following page, the actual size vs. area under the arterial blood concentration curve is plotted in blue with the multiple linear regression equation

(Equation 39 on page 112) shown in red. This plot clearly shows that trying to a straight line to the L-shaped curve is problematic and led to the low R^2 for goodness-of-fit.

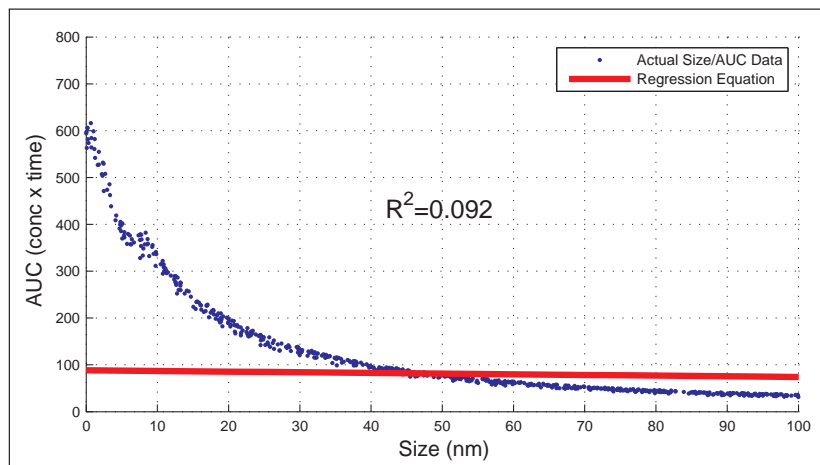


Figure 56. Plot of the regression equation vs. actual data

4.3.1.2 Statistical Significance.

Figure 57 on the following page shows the estimates for the coefficients of the regression equation shown in Equation 39 on page 112. It also summarizes the statistical significance information for the model, which can be checked using an F-test for overall fit and additional t-tests for testing the hypotheses about the individual parameters [17]. The F value of 76.08 is used to test the null hypothesis $H_o: \beta_1=\beta_2=\beta_3=\beta_4=0$. The p-value, <0.0001 , leads to the rejection of the null hypothesis, indicating that at least one of the regression coefficients is not zero [17].

The t-statistic for each independent variable compares the fit of the full model with all four independent variables to the reduced model with the independent variable corresponding to the t-statistic removed. The t-statistic for size in Figure 57 on the following page is -17.27, which is for testing the null hypothesis $H_o: \beta_1=0$ (i.e., there is no effect due to size) to compare the full- vs. reduced model. It helps show whether

the full model (4 independent variables) fits the data better than the reduced model (3 independent variables) [17].

In this case, the p-value for the test is < 0.0001 and the null hypothesis is rejected (based on a significance level $\alpha=0.05$), indicating that there *likely is* variation in area under the arterial blood concentration curve due to size that is not due to shape, surface coating, or surface charge. The p-value for shape also shows statistical significance for a significance level of $\alpha=0.05$. This indicates that there likely is variation in area under the arterial blood concentration curve due to shape that is not due to size, surface coating, or surface charge.

In comparison, the p-values for surface coating and surface charge do not allow rejection of the null hypothesis and we cannot conclude whether variations in area under the curve for arterial blood concentration are due to the independent variable exclusively, or due to the other three independent variables.

Parameter Estimates				
Term	Estimate	Std Error	t Ratio	Prob> t
Intercept	101.31779	4.419275	22.93	<.0001*
size	-0.146723	0.008496	-17.27	<.0001*
shape	-10.86543	4.226406	-2.57	0.0102*
surface coating	4.1789123	4.228018	0.99	0.3230
surface charge	-2.738099	4.282392	-0.64	0.5226

Figure 57. Parameter estimates for n=3000 simulations

4.3.2 An Alternative to Linear Regression.

As Figure 56 on the previous page and the low R^2 indicate the poor fit of the multiple linear regression model to actual data, an alternative to linear regression is necessary. Deriving a *nonlinear* regression model is more challenging as an approximate form of the regression equation must be identified. In Figure 54b on page 113, the left side of the L-shaped plot shows significant decrease in the area under the arterial blood concentration curve as size increases. At larger sizes, the area under

the curve increases in a near-linear manner.

After experimentation with numerous forms, an equation of the form $y = a - b \log(\text{size}) + \text{size}/c$ was finally identified as being a likely good fit for the area under the arterial blood concentration curve vs. size data. This equation was used in the MATLAB[®] function *nlinfit* to determine the coefficients. The first two terms of the equation help define the steeply downward sloping portion to the left side of the plot, while the third term provides the linear, upward-sloping behavior seen to the right side of the plot. See Figure 58. An R^2 of 0.943 was realized, indicating a relatively good fit between actual area under the arterial blood concentration curve data and the fitted equation.

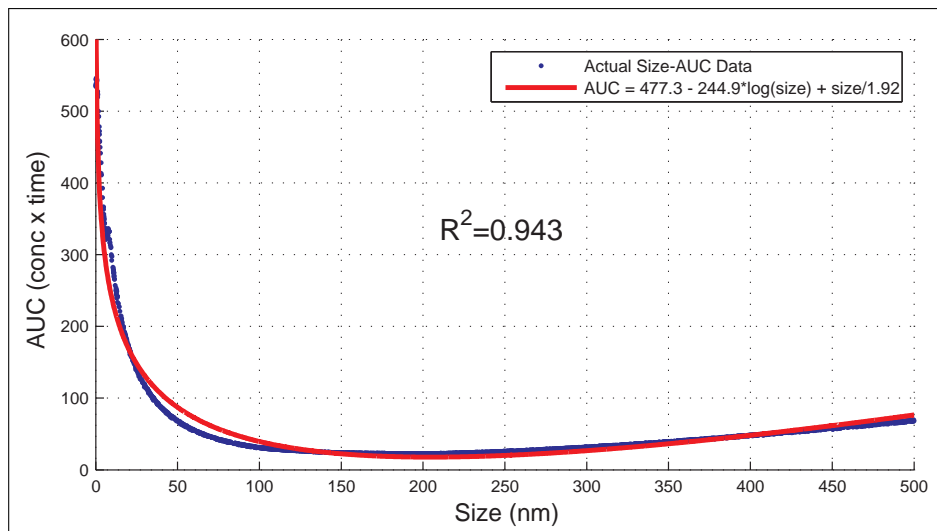


Figure 58. Fitted equation

The equation displayed in Figure 58 provides a tool to estimate the area under the arterial blood concentration curve, which is a surrogate of dose for a given compartment. Note that this equation applies to the exposure scenario of $C_{\text{inhalation}}=500$ ($\times 1000$ particles/liter). In this research, the equation was determined for arterial blood and analysis in Section 4.3.1.1 determined that size was the critical factor. For the model used in this research, the other physico-chemical properties (i.e., shape, sur-

face coating, and surface charge) can be eliminated as independent variables affecting the area under the arterial blood concentration curve. Other subcompartments can be analyzed instead, but arterial blood was chosen as it is central to the distribution of nanoparticles throughout the body.

4.3.2.1 Relating Area Under the Curve to Risk.

The current paradigm for risk analysis involves the use of in vivo testing, in which animals such as rats are exposed to external doses of a given chemical. Internal dose and the resulting adverse response (e.g., cell death, percent responding, etc.) at specific target tissues can be measured. This is repeated at various dosages, yielding a dose-response curve which can be used to assess risk for a given exposure scenario and to assist in establishing exposure limits based on risk.

In addition, a PBPK model can be created to simulate exactly what happened to the rat, thus recreating the external-to-internal dose relationship determined from in vivo research. Such models are useful for studying the time-course behavior of the chemical. PBPK models can also be used to extrapolate from high to low external dose and from animal to human.

For nanoparticle risk analysis, the PBPK model presented in this research can be allometrically-scaled for the rat to recreate in vivo results. Running the rat-specific PBPK model will generate concentration plots from which area under the curve can be calculated. Assuming that area under the curve for the rat equals area under the curve for the human, and the toxicological responses are the same, the human-specific version of this model can be used to determine the external exposure to the human, by working backwards from area under the curve. More specifically, once area under the curve is known then concentration can be determined as $\text{area under the curve} \div \text{concentration} \times \text{time}$. The source term (i.e., external exposure) can be

determined since

$$\vec{c}_{ss} = -A^{-1}\vec{s} \Rightarrow \vec{s} = -A\vec{c}_{ss} \quad (40)$$

The results of this research is the defining of a new paradigm in which we use the traditional methodology of in vitro and in vivo research combined with PBPK modeling, but use area under the curve as surrogate of dose which bridges rat to human. By bridging, the dose-response curves specific to the animal can be used to establish equivalent human dose-response curves. More importantly, we can use area under the curve and the mathematics presented here to back-calculate and find the external exposure to the human which generates an equivalent response to that seen in the animal. Knowing these external exposure values then assists toxicologists and policy makers in assessing risk and setting appropriate exposure limits.

V. Conclusion

“A better understanding is needed about the interplay of factors contributing and affecting uptake and disposition from deposits in the respiratory tract or from other portals of entry.” - Günter Oberdörster, et al. [58]

This work here begins the exploration of mathematical representations of cellular transport processes and how they may provide insight for nanoparticle exposures. Using the traditional assumption of instantaneous equilibration can provide vastly different nanoparticle concentrations when compared to other transport processes. It is important that future research focus on further exploring which transport processes are applicable to nanoparticles and determining appropriate values or ranges for transport parameters governing nanoparticle pharmacokinetics. Further refinement of the mathematical representations of the cellular transport processes will help improve the predictive ability of the model.

Physico-chemical property-related phenomena of nanoparticles cause considerable differences in the biokinetics. Engineering the particles to take on certain qualities (e.g., size, shape, surface coatings, surface charge) can help defeat, whether intentionally or unintentionally, various tissue barriers and loss mechanisms (e.g., phagocytosis). Refining the model to include these qualities is important and in vitro and in vivo research are critical to improving this PBPK model, which is perhaps the first of its kind to extensively explore the alternate transport processes.

Redefining nanoparticle risk assessment is not simply important, rather it is *necessary*. The current methodology of performing toxicity testing on each possible variant of nanoparticles is impractical and perhaps impossible as new variants occur daily and quality control challenges with producing homogeneous nanoparticles suggest that toxicity may change depending on the batch.

5.1 Addressing the Research Questions

Section 1.2 on page 2 listed three research questions fundamental to this dissertation. The following is a synopsis of the findings related to those questions:

- **Question #1: For nanoparticle PBPK modeling, what are the implications of these different processes on tissue concentrations, as compared to an assumption of instantaneous equilibration?** Section 4.1 on page 87 shows that deviating from the traditional assumption of instantaneous equilibration leads to very different concentrations. Instantaneous equilibration relies on first calculating tissue concentrations, from which venous blood concentrations are calculated using a partition coefficient. By inserting mathematical representations for diffusion, active transport, and carrier mediated transport (and by expanding to three subcompartments per organ), we see various behaviors emerge. Such behaviors include delays to approach steady state, tissue accumulation, and the dominance of diffusion. Although more research is necessary on the applicability of active transport, it is evident that it could lead to considerable accumulation in tissue as it operates, by definition, independent of concentration. Simply expanding the model to three subcompartments per organ, allowed more accurate placement of loss mechanisms such as phagocytosis, urine, etc.
- **Question #2: How can these implications guide the direction of nanotoxicity research, particularly in determining parameter values for transport processes elucidated to be important?** Section 4.1 on page 87 shows the differences in concentrations presented when the transport processes are changed. The range finding technique described in this research was critical to the subsequent phases of research that followed it, but does not replace future research on parameterization. The eigenvalue analysis technique provides a new tool for the

nanotoxicity community, which can provide a rapid summary of model behavior using a small set of simulations. It can narrow the range of concern for a certain parameter or perhaps identify parameters which do not significantly affect concentrations in organs, thus avoiding unnecessary research. The physico-chemical modifiers were an important first step in defining size/shape/surface-specific transport behavior, which often varies organ-to-organ. More research is necessary to identify a more complete set of variables that affect dose to the organ. More research is necessary on how these physico-chemical properties interact with each other, e.g., how do special coatings extend the size range of nanoparticles that can cross a tissue barrier, etc.

- **Question #3: How will these findings suggest a possible new paradigm for nanoparticle risk analysis, particularly in the area of dose-response assessment?** PBPK is beneficial as it can estimate internal dose given an external dose, but the approach presented here improves on that capability, due to inclusion of physico-chemical properties. Section 4.3 on page 112 shows that there is strong reason to believe that size truly is the most important physico-chemical property that affects the biokinetics of nanoparticles. By fitting an equation, AUC can be estimated at various toxic endpoints based on knowledge of nanoparticle size only. Toxicologists have already performed, and continue to perform, extensive in vitro and in vivo research on nanoparticle exposures. Their knowledge of which tissues show considerable adverse response, when combined with simulation modeling that can help estimate dose to the organ, could offer a better alternative than the current risk assessment tools available to occupational health practitioners. The new paradigm established by this research allows traditional in vitro, in vivo, and PBPK modeling to be used, but substitutes area under the curve as a surrogate of dose. By doing so, animal testing results can be bridged to the hu-

man, after which the corresponding external exposure to the human necessary to generate the toxicological response can be calculated. This new paradigm allows toxicologists and policymakers to then assess risk to a given exposure and assist in setting appropriate exposure limits for nanoparticles.

5.2 Recommendations for the Future

Without question, nanotechnology will have a considerable impact on the world, primarily from a consumer standpoint and likely from a health and environmental perspective, also. The burgeoning field of nanotoxicology will undoubtedly continue to grow as the prevalence of nanomaterials grows, as it is clear that nano-sized particles present new exposure risks not seen by larger particles of the same material. Research needs to build on the foundation set by ultrafine particle research, but clearly more information is needed in order to properly conduct risk assessment on nanoparticle exposures. Comprehensive modeling of exposure levels to humans is necessary, especially in the absence of exposure limits and guidelines.

In closing, there are several ideas on how the PBPK model can be further improved, in order to advance the capabilities to estimate dose and assess risk due to nanoparticle exposures:

- Use the new paradigm as a potential screening strategy and refine it as in vitro and in vivo research evolve.
- Add the lymph system as it is the parallel transport system to blood circulation. Phagocytosis is not an elimination process. Instead, include the dynamics associated with macrophage populations (i.e., any capacity limits, effective life, etc.). Lymph nodes might also be toxicological endpoints and lymph re-enters circulation.
- Expand the lung model to include variations in deposition and transport which

depart from assumptions of uniformity.

- Expand the kidney portion of the model to include the complexities associated with secretion and reabsorption.
- Expand the ingestion route of entry to address whether nanoparticles entrapped in swallowed fluid can actually be re-entrained and enter circulation via the GI tract and portal circulation
- Coagulation and agglomeration should be addressed. An assumption of monodisperse, singlet particles may overstate organ exposure and accumulation.
- Qualitative factors for shape, surface coatings, and surface charge need thorough research.
- Exploit data from pharmaceutical research, such as the extensive work on targeting the brain and defeating the blood-brain barrier to treat brain-related diseases. Such pharmaceutical insight can guide toxicological research.
- Refine the mathematical representations of transport processes by calibrating to in vitro and in vivo results, as they become available.

Appendix A. Research Assumptions

General assumptions used for the dissertation research:

Model should focus on inhalational exposures. However, ingestion will be included with respect to swallowing of nanoparticles cleared from the respiratory tract by the mucociliary escalator. Literature does not support dermal exposures as being a confirmed, major exposure pathway, and therefore it will not be covered in dissertation research.

Deposition of particles in the respiratory tract will include simplifying assumptions that deposition and subsequent absorption/clearance is uniform within a given region of the respiratory tract (i.e., nasopharyngeal, tracheobronchial, and alveolar). More complex deposition models exist, but are not of primary importance for this dissertation as general behavior, not precise concentrations, are the focus. Alveolar deposition will be the primary focus, but nasopharyngeal deposition will be included as part of the nose-to-brain translocation pathway. The overloading phenomena which leads to possible interstitial translocation is not included in the model.

Translocation between the alveolar and interstitial regions of the lungs is a critical part of this model and most likely warrants expanding the lung compartment accordingly. A major difference between traditional particle toxicology and nanoparticle toxicology is this interstitial translocation capability.

Inhalational pathway does not include modeling of the nose-to-brain translocation pathway, which is separate from the BBB translocation pathway. Even if it results in a minor exposure pathway, nose-to-brain translocation is of considerable interest to the pharmaceutical industry, especially regarding administration of drugs for treatment of brain-related diseases (e.g., Parkinson's, Alzheimer's, etc.).

Appendix B. Full PBPK Model in STELLA®

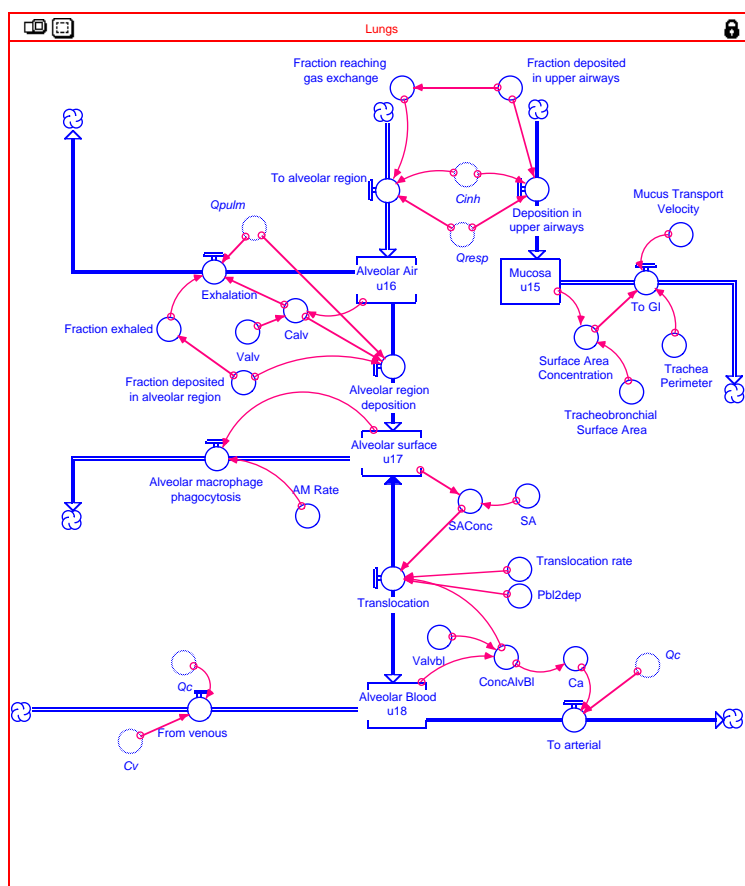
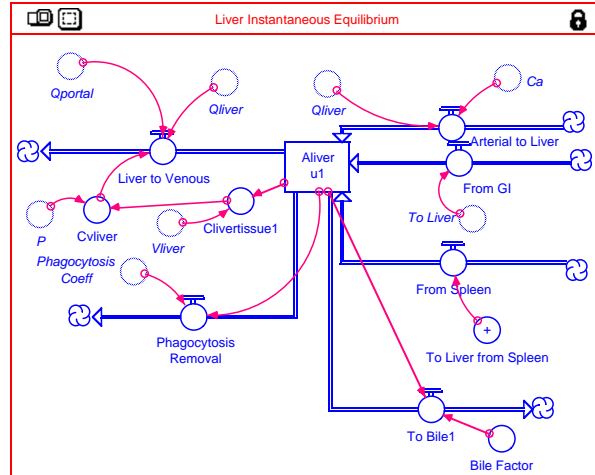
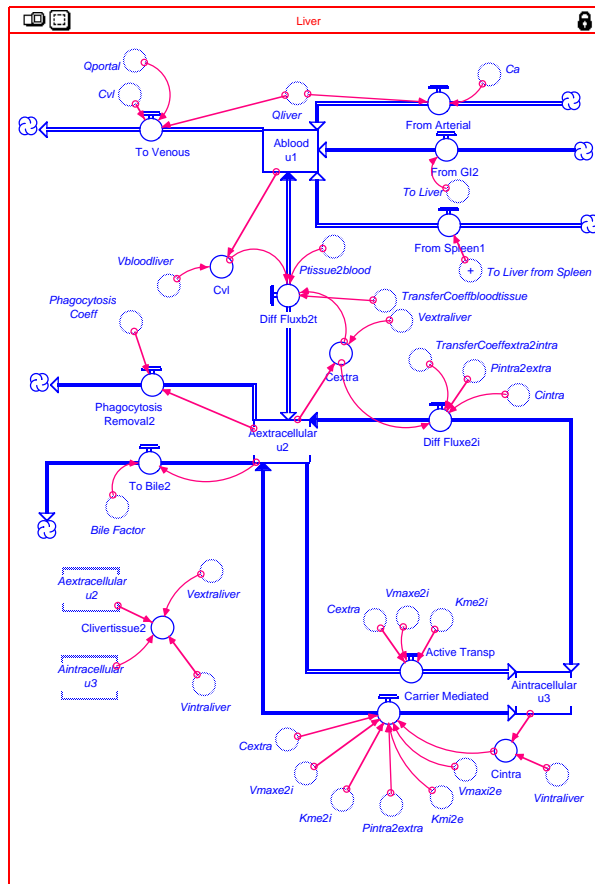


Figure 59. Lung representation in STELLA®

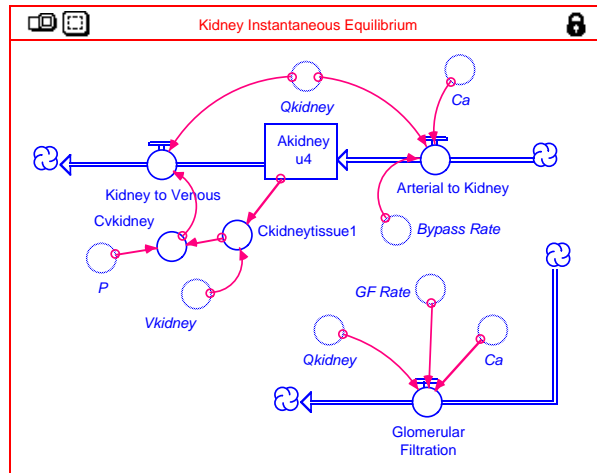


(a) Instantaneous equilibration

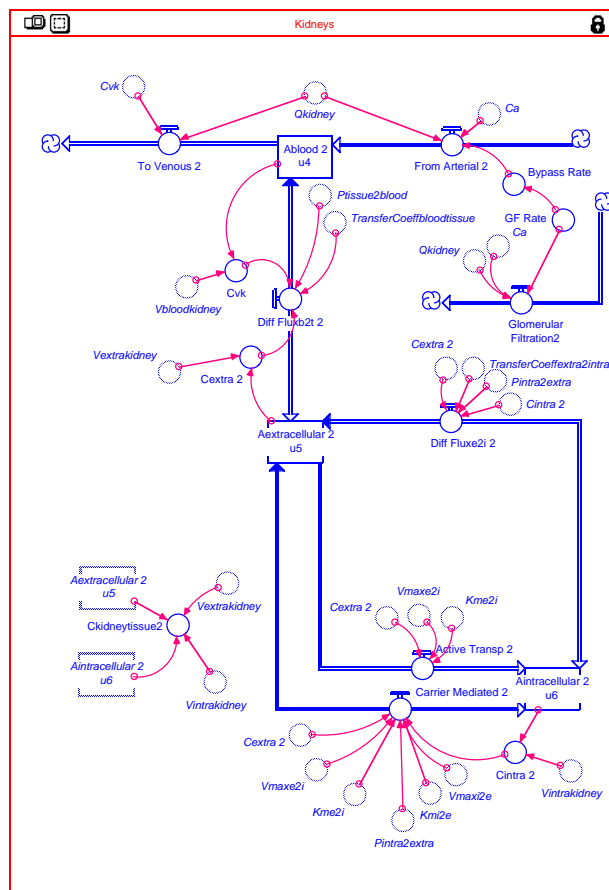


(b) Expanded model

Figure 60. Liver representation in STELLA®

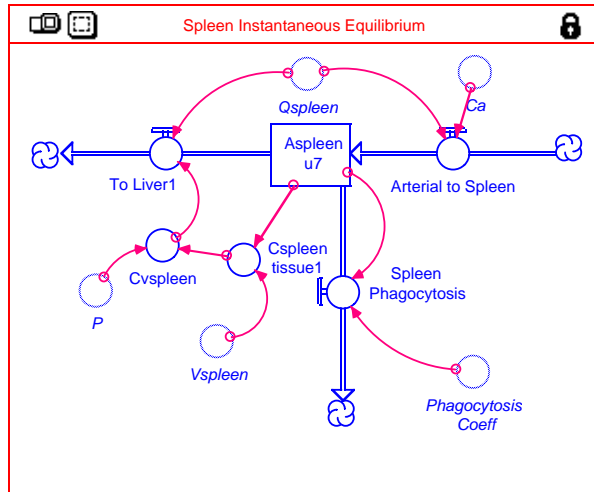


(a) Instantaneous equilibration

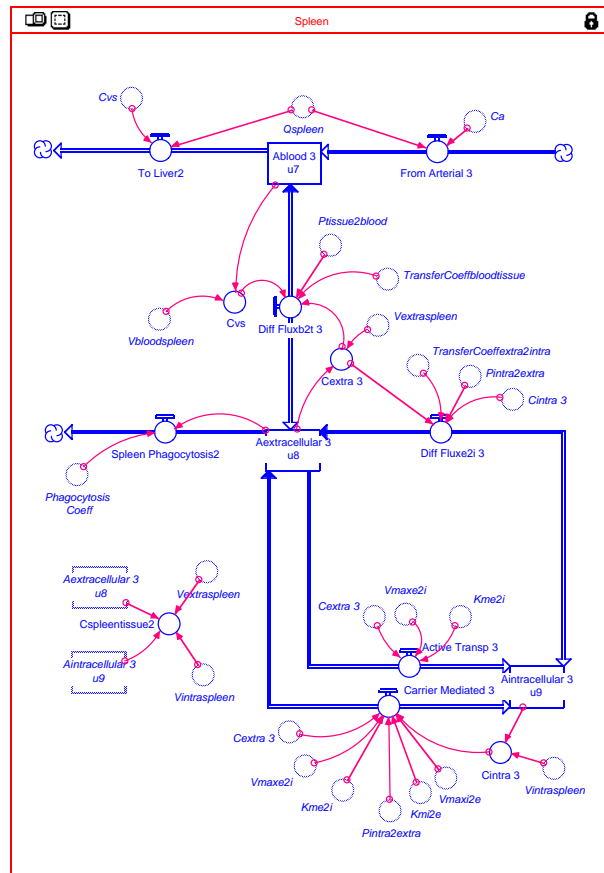


(b) Expanded model

Figure 61. Kidney representation in STELLA®

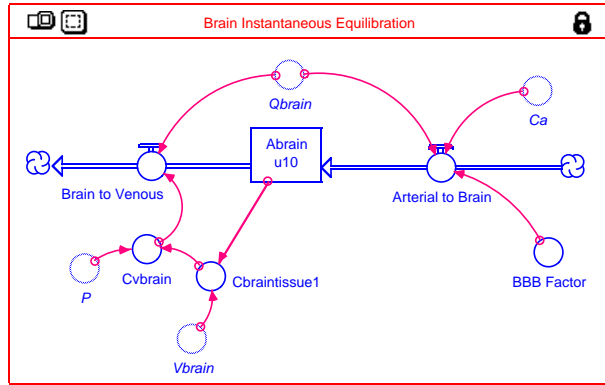


(a) Instantaneous equilibration

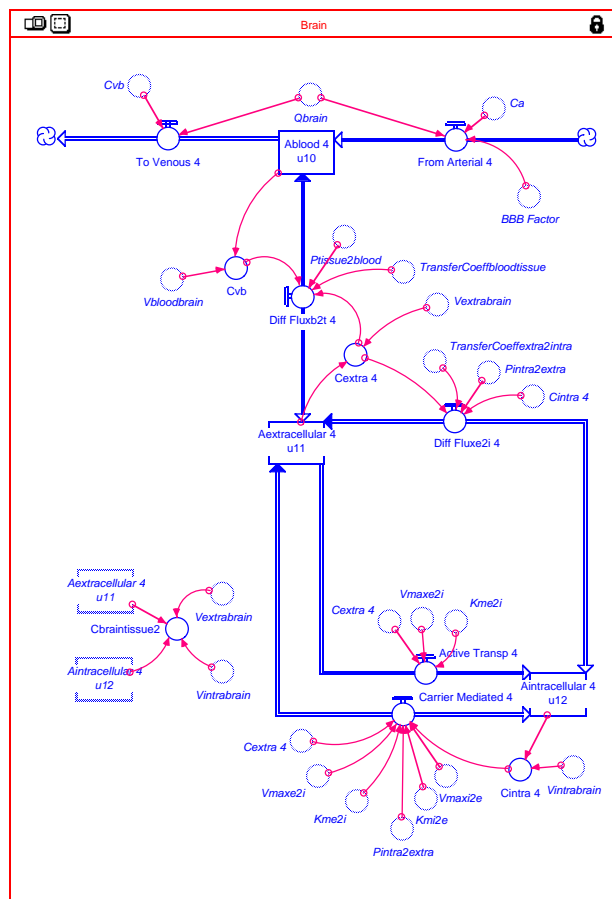


(b) Expanded model

Figure 62. Spleen representation in STELLA®

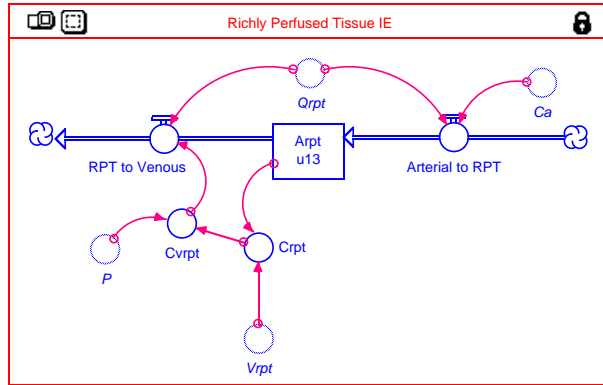


(a) Instantaneous equilibration

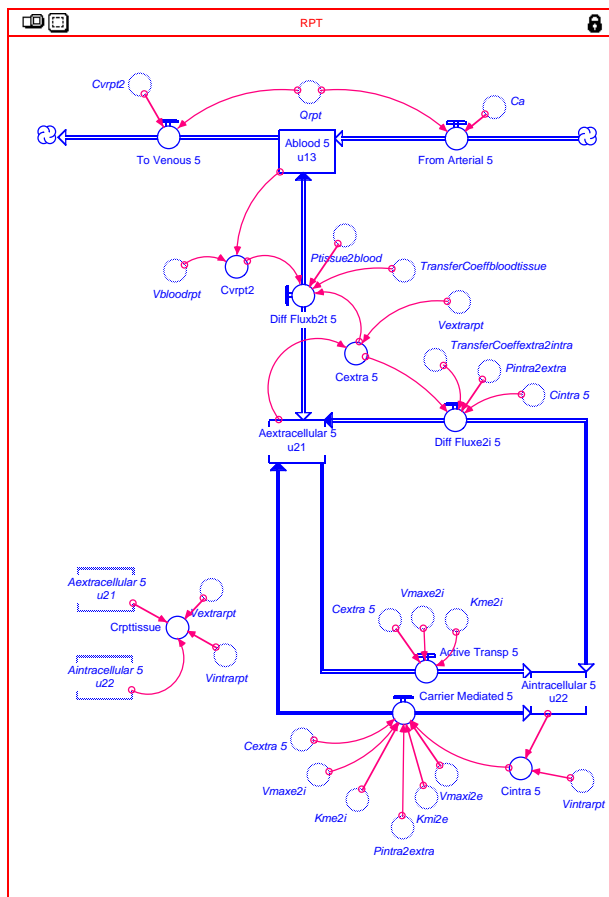


(b) Expanded model

Figure 63. Brain representation in STELLA®

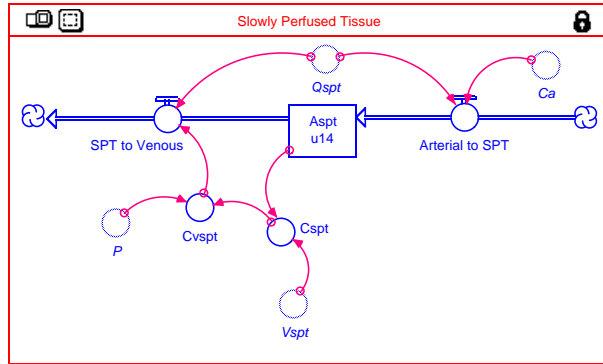


(a) Instantaneous equilibration

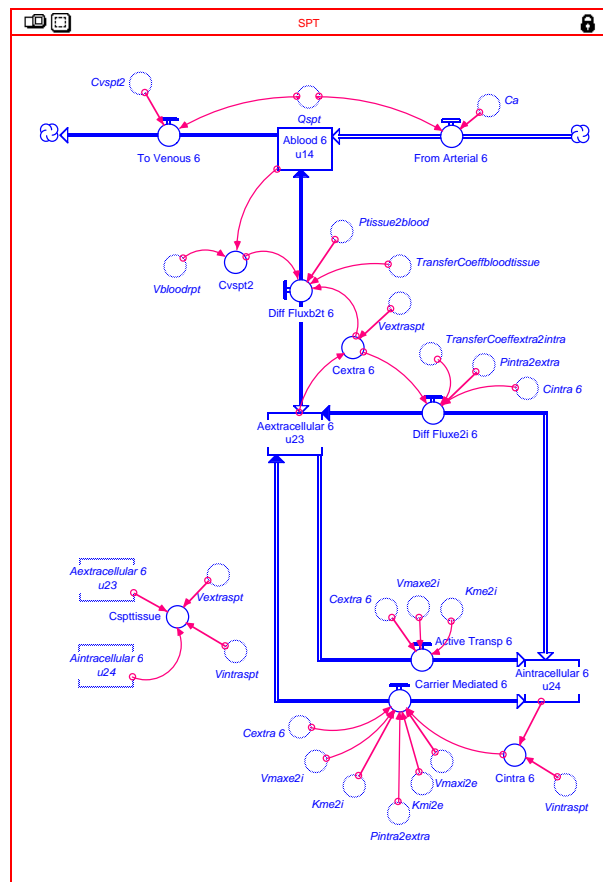


(b) Expanded model

Figure 64. Richly perfused tissue representation in STELLA®



(a) Instantaneous equilibration



(b) Expanded model

Figure 65. Slowly perfused tissue representation in STELLA®

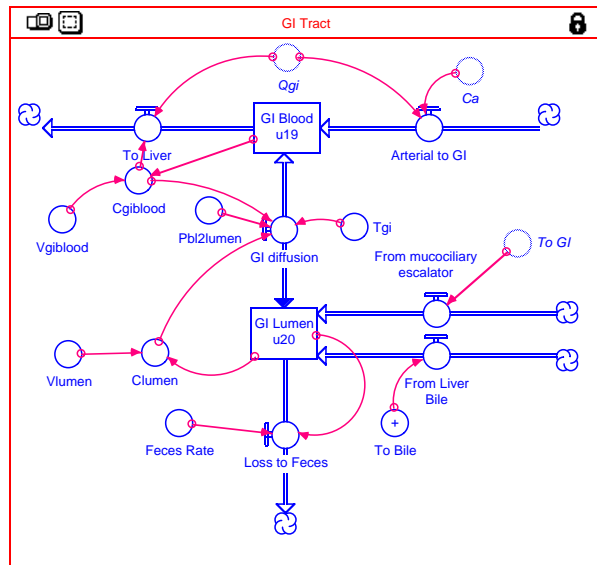


Figure 66. GI tract representation in STELLA®

Fraction reaching gas exchange = 1 – Fraction deposited in upper airways

$$\frac{d(\text{Alveolar Blood } u18)}{dt} = \text{Translocation} + \text{From venous} - \text{To arterial} \quad (42)$$

where

$$\text{Translocation} = \text{Translocation rate} \times \text{SAConc} - \text{ConcAlvBl}/\text{Pbl2dep}$$

$$\text{From venous} = Q_c \times C_v$$

$$\text{To arterial} = Q_c \times C_a$$

$$\text{ConcAlvBl} = \text{Alveolar Blood } u18 / \text{Valvbl}$$

$$C_a = \text{ConcAlvBl}$$

$$\text{SAConc} = \text{Alveolar surface } u17 / \text{SA}$$

$$\begin{aligned} \frac{d(\text{Alveolar surface } u17)}{dt} = & \text{Alveolar region deposition} - \text{Translocation} \\ & - \text{Alveolar macrophage phagocytosis} \end{aligned} \quad (43)$$

where

$$\text{Alveolar region deposition} = Q_{\text{pulm}} \times C_{\text{alv}} \times \text{Fraction deposited in alveolar region}$$

$$\text{Translocation} = \text{Translocation rate} \times (\text{SAConc} - \text{ConcAlvBl}/\text{Pbl2dep})$$

$$\text{Alveolar macrophage phagocytosis} = \text{Alveolar surface } u17 \times \text{AM Rate}$$

$$\frac{d(\text{Mucosa } u15)}{dt} = \text{Deposition in upper airways} - \text{To GI} \quad (44)$$

where

Deposition in upper airways = $Q_{resp} \times C_{inh} \times \text{Fraction deposited in upper airways}$

To GI = Surface Area Concentration \times Mucus Transport Velocity
 \times Trachea Perimeter

Surface Area Concentration = Mucosa u15 / Tracheobronchial Surface Area

Liver ODEs

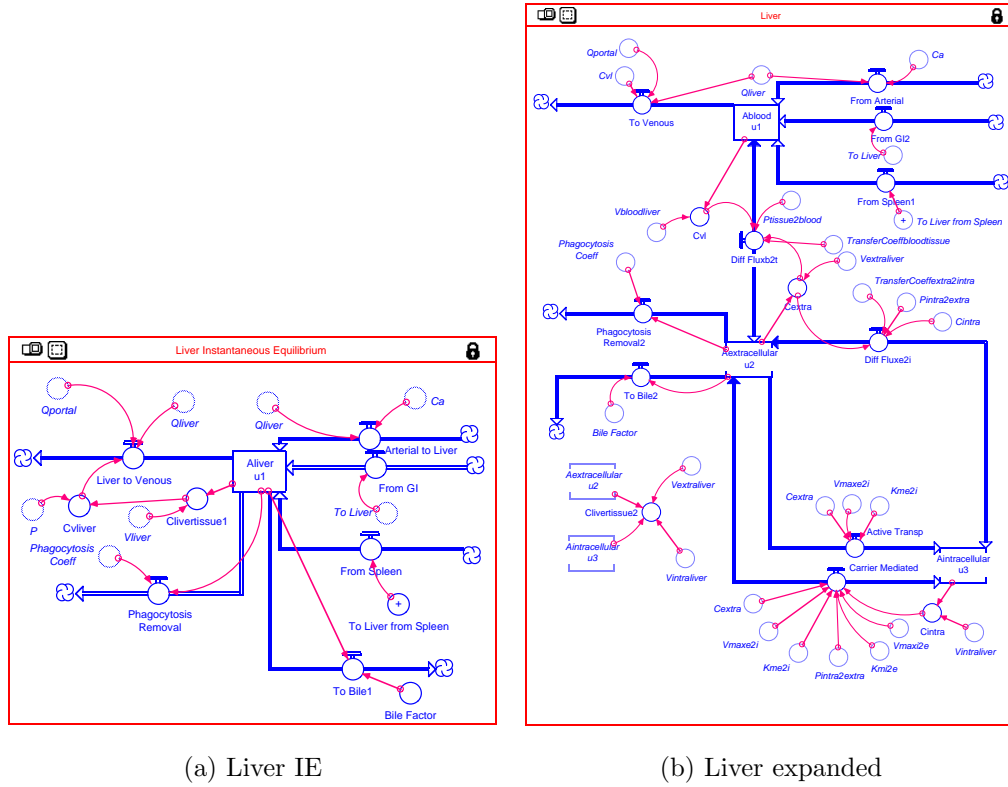


Figure 68. Liver IE and expanded models in STELLA®

Liver IE.

$$\begin{aligned} \frac{d(\text{Aliver } u1)}{dt} = & \text{From GI} + \text{Arterial to Liver} + \text{From Spleen} \\ & - \text{Liver to Venous} - \text{Phagocytosis Removal} - \text{To Bile} \end{aligned} \quad (45)$$

where

$$\text{From GI} = \text{To Liver}$$

$$\text{Arterial to Liver} = Q_{\text{liver}} \times C_a$$

$$\text{From Spleen} = \text{To Liver from Spleen}$$

$$\text{Liver to Venous} = (Q_{\text{liver}} + Q_{\text{portal}}) \times C_{\text{vliver}}$$

$$\text{Phagocytosis Removal} = A_{\text{liver}} u_1 \times \text{Phagocytosis Coeff}$$

$$\text{To Bile1} = A_{\text{liver}} u_1 \times \text{Bile Factor}$$

$$C_{\text{livertissue1}} = A_{\text{liver}} u_1 / V_{\text{liver}}$$

$$C_{\text{vliver}} = C_{\text{livertissue1}} / P$$

$$\text{To Liver from Spleen} = \text{To Liver1} + \text{To Liver2}$$

Liver (Expanded).

$$\begin{aligned} \frac{d(\text{Ablood } u_1)}{dt} = & \text{From Arterial} + \text{From GI2} + \text{From Spleen1} \\ & - \text{To Venous} - \text{Diff Fluxb2t} \end{aligned} \quad (46)$$

where

$$\text{From Arterial} = Q_{\text{liver}} \times C_a$$

$$\text{From GI2} = \text{To Liver}$$

$$\text{From Spleen1} = \text{To Liver from Spleen}$$

$$\text{To Venous} = (Q_{\text{liver}} + Q_{\text{portal}}) \times C_{\text{vl}}$$

$$\text{Diff Fluxb2t} = \text{TransferCoeffbloodtissue} \times (C_{\text{vl}} - C_{\text{extra}}/P_{\text{tissue2blood}})$$

$$C_{\text{vl}} = \text{Ablood } u_1 / V_{\text{bloodliver}}$$

$$\begin{aligned} \frac{d(\text{Aextracellular } u_2)}{dt} = & \text{Diff Fluxb2t} - \text{Carrier Mediated} - \text{Diff Fluxe2i} \\ & - \text{Active Transp} - \text{To Bile2} - \text{Phagocytosis Removal2} \end{aligned} \quad (47)$$

where

$$\begin{aligned} \text{Diff Fluxb2t} &= \text{TransferCoeffbloodtissue} \times (\text{Cv1} - \text{Cextra}/\text{Ptissue2blood}) \\ \text{Carrier Mediated} &= \text{Vmaxe2i} \times \text{Cextra}/(\text{Kme2i} + \text{Cextra}) \\ &\quad - \text{Vmaxi2e} \times (\text{Cintra}/\text{Pintra2extra})/(\text{Kmi2e} + \text{Cintra}/\text{Pintra2extra}) \\ \text{Diff Fluxe2i} &= \text{TransferCoeffextra2intra} \times (\text{Cextra} - \text{Cintra}/\text{Pintra2extra}) \\ \text{Active Transp} &= \text{Vmaxe2i} \times \text{Cextra} / (\text{Kme2i} + \text{Cextra}) \\ \text{To Bile2} &= \text{Bile Factor} \times \text{Aextracellular } u_2 \\ \text{Phagocytosis Removal2} &= \text{Aextracellular } u_2 \times \text{Phagocytosis Coeff} \\ \text{Cextra} &= \text{Aextracellular } u_2 / \text{Vextraliver} \\ \text{Cintra} &= \text{Aintracellular } u_3 / \text{Vintraliver} \end{aligned}$$

$$\frac{d(\text{Aintracellular } u_3)}{dt} = \text{Carrier Mediated} + \text{Diff Fluxe2i} + \text{Active Transp} \quad (48)$$

where

$$\begin{aligned} \text{Carrier Mediated} &= \text{Vmaxe2i} \times \text{Cextra}/(\text{Kme2i} + \text{Cextra}) - \text{Vmaxi2e} \\ &\quad \times (\text{Cintra}/\text{Pintra2extra})/(\text{Kmi2e} + \text{Cintra}/\text{Pintra2extra}) \\ \text{Diff Fluxe2i} &= \text{TransferCoeffextra2intra} \times (\text{Cextra} - \text{Cintra}/\text{Pintra2extra}) \\ \text{Active Transp} &= \text{Vmaxe2i} \times \text{Cextra} / (\text{Kme2i} + \text{Cextra}) \end{aligned}$$

GI ODEs

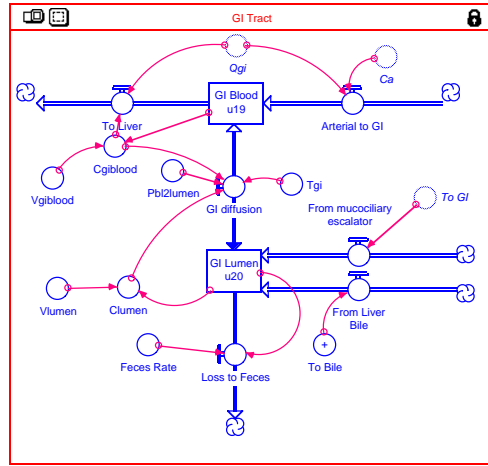


Figure 69. GI model in STELLA®

$$\frac{d(\text{GI Blood u19})}{dt} = \text{Arterial to GI} + \text{GI diffusion} - \text{To Liver} \quad (49)$$

where

$$\text{Arterial to GI} = Q_{gi} \times Ca$$

$$\text{GI diffusion} = T_{gi} \times (Clumen - Cgiblood / Pbl2lumen)$$

$$\text{To Liver} = Q_{gi} \times Cgiblood$$

$$Cgiblood = \text{GI Blood u19} / Vgiblood$$

$$Clumen = \text{GI Lumen u20} / Vlumen$$

$$\begin{aligned} \frac{d(\text{GI Lumen u20})}{dt} = & \text{From mucociliary escalator} + \text{From Liver Bile} \\ & - \text{Loss to Feces} - \text{GI diffusion} \end{aligned} \quad (50)$$

where

From mucociliary escalator = To GI

From Liver Bile = To Bile

Loss to Feces = GI Lumen \times Feces Rate

GI diffusion = $T_{gi} \times (C_{lumen} - C_{giblood} / P_{bl2lumen})$

Kidney ODEs

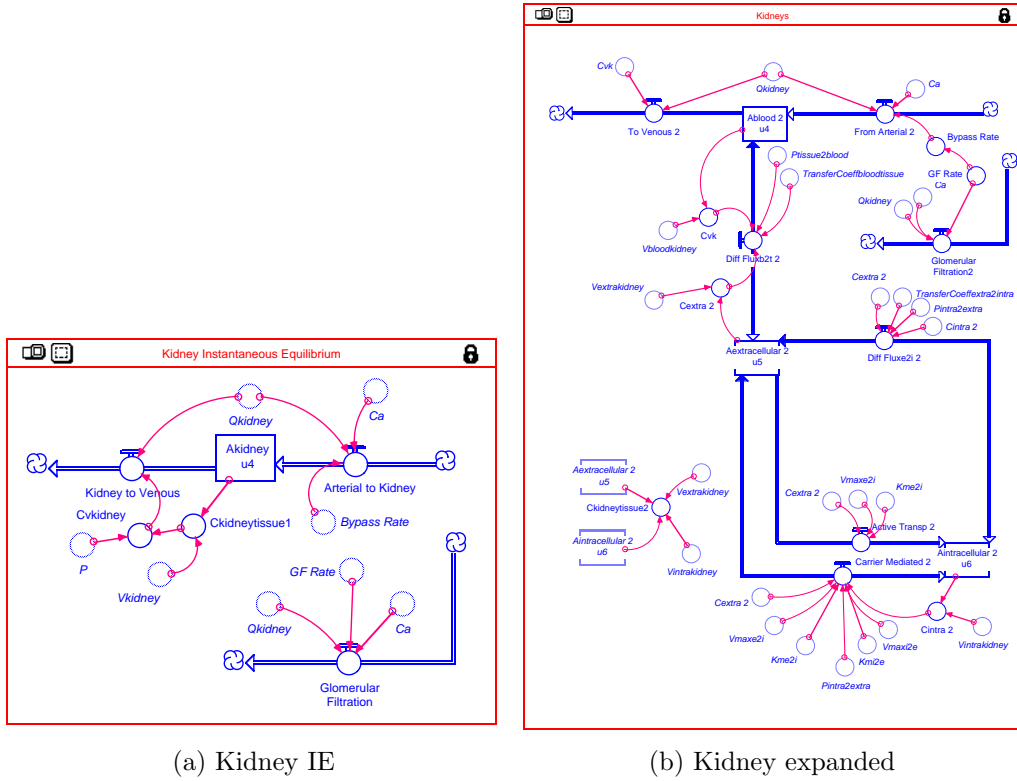


Figure 70. Kidney IE and expanded models in STELLA®

Kidney IE.

$$\text{Glomerular Filtration} = \text{GF Rate} \times Q_{\text{kidney}} \times Ca \quad (51a)$$

$$\frac{d(\text{Akidney } u4)}{dt} = \text{Arterial to Kidney} - \text{Kidney to Venous} \quad (51b)$$

where

$$\text{Arterial to Kidney} = \text{Bypass Rate} \times Q_{\text{kidney}} \times C_a$$

$$\text{Kidney to Venous} = Q_{\text{kidney}} \times C_{v\text{kidney}}$$

$$C_{\text{kidneytissue1}} = A_{\text{kidney}} u_4 / V_{\text{kidney}}$$

$$C_{v\text{kidney}} = C_{\text{kidneytissue1}} / P$$

Kidney (Expanded).

$$\text{Glomerular Filtration2} = Q_{\text{kidney}} \times C_a \times \text{GF Rate} \quad (52a)$$

$$\frac{d(\text{Ablood 2 } u_4)}{dt} = \text{From Arterial 2} - \text{To Venous 2} - \text{Diff Fluxb2t 2} \quad (52b)$$

where

$$\text{From Arterial 2} = Q_{\text{kidney}} \times C_a \times \text{Bypass Rate}$$

$$\text{To Venous 2} = Q_{\text{kidney}} \times C_{vk}$$

$$\text{Diff Fluxb2t 2} = \text{TransferCoeffbloodtissue} \times (C_{vk} - C_{\text{extra 2}} / P_{\text{tissue2blood}})$$

$$\text{Bypass Rate} = 1 - \text{GF Rate}$$

$$C_{vk} = \text{Ablood 2 } u_4 / V_{\text{bloodkidney}}$$

$$\begin{aligned} \frac{d(\text{Aextracellular 2 } u_5)}{dt} = & \text{Diff Fluxb2t 2} - \text{Carrier Mediated 2} \\ & - \text{Diff Fluxe2i 2} - \text{Active Transp 2} \end{aligned} \quad (53)$$

where

$$\text{Diff Flux}_{b2t} = \text{TransferCoeff}_{\text{bloodtissue}} \times (C_{vk} - C_{\text{extra}2}/P_{\text{tissue}2\text{blood}})$$

$$\text{Carrier Mediated} = V_{\text{maxe}2i} \times C_{\text{extra}2} / (K_{\text{me}2i} + C_{\text{extra}2})$$

$$- V_{\text{maxi}2e} \times (C_{\text{intra}2}/P_{\text{intra}2\text{extra}}) / (K_{\text{mi}2e} + C_{\text{intra}2}/P_{\text{intra}2\text{extra}})$$

$$\text{Diff Flux}_{e2i} = \text{TransferCoeff}_{\text{extra}2\text{intra}} \times (C_{\text{extra}2} - C_{\text{intra}2}/P_{\text{intra}2\text{extra}})$$

$$\text{Active Transp} = V_{\text{maxe}2i} \times C_{\text{extra}2} / (K_{\text{me}2i} + C_{\text{extra}2})$$

$$C_{\text{extra}2} = A_{\text{extracellular}2} u5 / V_{\text{extrakidney}}$$

$$C_{\text{intra}2} = A_{\text{intracellular}2} u6 / V_{\text{intrakidney}}$$

$$\frac{d(A_{\text{intracellular}2} u6)}{dt} = \text{Carrier Mediated} + \text{Diff Flux}_{e2i} + \text{Active Transp} \quad (54)$$

where

$$\text{Carrier Mediated} = V_{\text{maxe}2i} \times C_{\text{extra}2} / (K_{\text{me}2i} + C_{\text{extra}2})$$

$$- (V_{\text{maxi}2e} \times (C_{\text{intra}2}/P_{\text{intra}2\text{extra}}) / (K_{\text{mi}2e} + C_{\text{intra}2}/P_{\text{intra}2\text{extra}}))$$

$$\text{Diff Flux}_{e2i} = \text{TransferCoeff}_{\text{extra}2\text{intra}} \times (C_{\text{extra}2} - C_{\text{intra}2}/P_{\text{intra}2\text{extra}})$$

$$\text{Active Transp} = V_{\text{maxe}2i} \times C_{\text{extra}2} / (K_{\text{me}2i} + C_{\text{extra}2})$$

Spleen ODEs

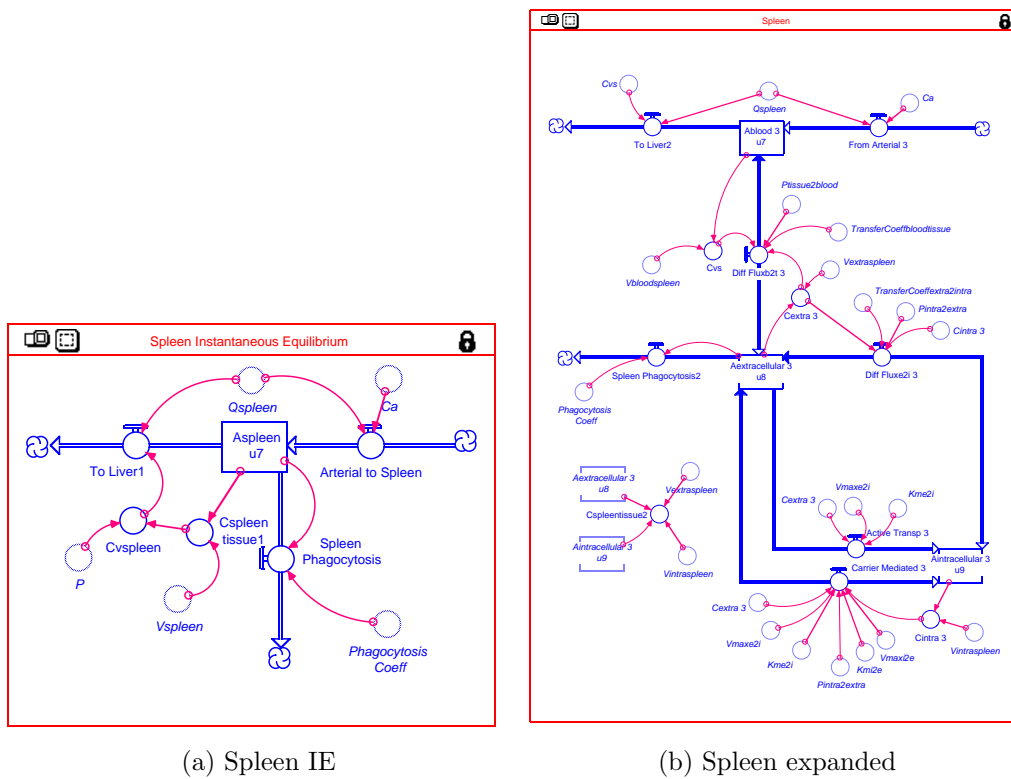


Figure 71. Spleen IE and expanded models in STELLA®

Spleen IE.

$$\frac{d(\text{Aspleen u7})}{dt} = \text{Arterial to Spleen} - \text{To Liver1} - \text{Spleen Phagocytosis} \quad (55)$$

where

$$\text{Arterial to Spleen} = Q_{\text{spleen}} \times C_a$$

$$\text{To Liver1} = Q_{\text{spleen}} \times C_{\text{vspleen}}$$

$$\text{Spleen Phagocytosis} = \text{Aspleen u7} \times \text{Phagocytosis Coeff}$$

$$C_{\text{spleen tissue1}} = A_{\text{spleen u7}} / V_{\text{spleen}}$$

$$C_{\text{vspleen}} = C_{\text{spleen tissue1}} / P$$

Spleen (Expanded).

$$\frac{d(\text{Ablood 3 u7})}{dt} = \text{From Arterial 3} - \text{To Liver2} - \text{Diff Fluxb2t 3} \quad (56)$$

where

$$\text{From Arterial 3} = Q_{\text{spleen}} \times C_a$$

$$\text{To Liver2} = Q_{\text{spleen}} \times C_{\text{vs}}$$

$$\text{Diff Fluxb2t 3} = \text{TransferCoeffbloodtissue} \times (C_{\text{vs}} - C_{\text{extra 3}}/P_{\text{tissue2blood}})$$

$$C_{\text{vs}} = \text{Ablood 3 u7} / V_{\text{bloodspleen}}$$

$$\begin{aligned} \frac{d(\text{Aextracellular 3 u8})}{dt} = & \text{Diff Fluxb2t 3} - \text{Carrier Mediated 3} - \text{Diff Fluxe2i 3} \\ & - \text{Active Transp 3} - \text{Spleen Phagocytosis2} \end{aligned} \quad (57)$$

where

$$\text{Diff Fluxb2t 3} = \text{TransferCoeffbloodtissue} \times (C_{\text{vs}} - C_{\text{extra 3}}/P_{\text{tissue2blood}})$$

$$\text{Carrier Mediated 3} = V_{\text{maxe2i}} \times C_{\text{extra 3}} / (K_{\text{me2i}} + C_{\text{extra 3}})$$

$$- V_{\text{maxi2e}} \times (C_{\text{intra 3}}/P_{\text{intra2extra}}) / (K_{\text{mi2e}} + C_{\text{intra 3}}/P_{\text{intra2extra}})$$

$$\text{Diff Fluxe2i 3} = \text{TransferCoeffextra2intra} \times (C_{\text{extra 3}}$$

$$- \text{Cintra } 3 / \text{Pintra2extra})$$

$$\text{Active Transp } 3 = \text{Vmaxe2i} \times \text{Cextra } 3 / (\text{Kme2i} + \text{Cextra } 3)$$

$$\text{Spleen Phagocytosis2} = \text{Aextracellular } 3 \text{ u8} \times \text{Phagocytosis Coeff}$$

$$\text{Cextra } 3 = \text{Aextracellular } 3 \text{ u8} / \text{Vextraspleen}$$

$$\text{Cintra } 3 = \text{Aintracellular } 3 \text{ u9} / \text{Vintraspleen}$$

$$\frac{d(\text{Aintracellular } 3 \text{ u9})}{dt} = \text{Carrier Mediated } 3 + \text{Diff Fluxe2i } 3 + \text{Active Transp } 3 \quad (58)$$

where

$$\text{Carrier Mediated } 3 = \text{Vmaxe2i} \times \text{Cextra } 3 / (\text{Kme2i} + \text{Cextra } 3)$$

$$- \text{Vmaxi2e} \times (\text{Cintra } 3 / \text{Pintra2extra}) / (\text{Kmi2e} + \text{Cintra } 3 / \text{Pintra2extra})$$

$$\text{Diff Fluxe2i } 3 = \text{TransferCoeffextra2intra} \times (\text{Cextra } 3 - \text{Cintra } 3 / \text{Pintra2extra})$$

$$\text{Active Transp } 3 = \text{Vmaxe2i} \times \text{Cextra } 3 / (\text{Kme2i} + \text{Cextra } 3)$$

Brain ODEs

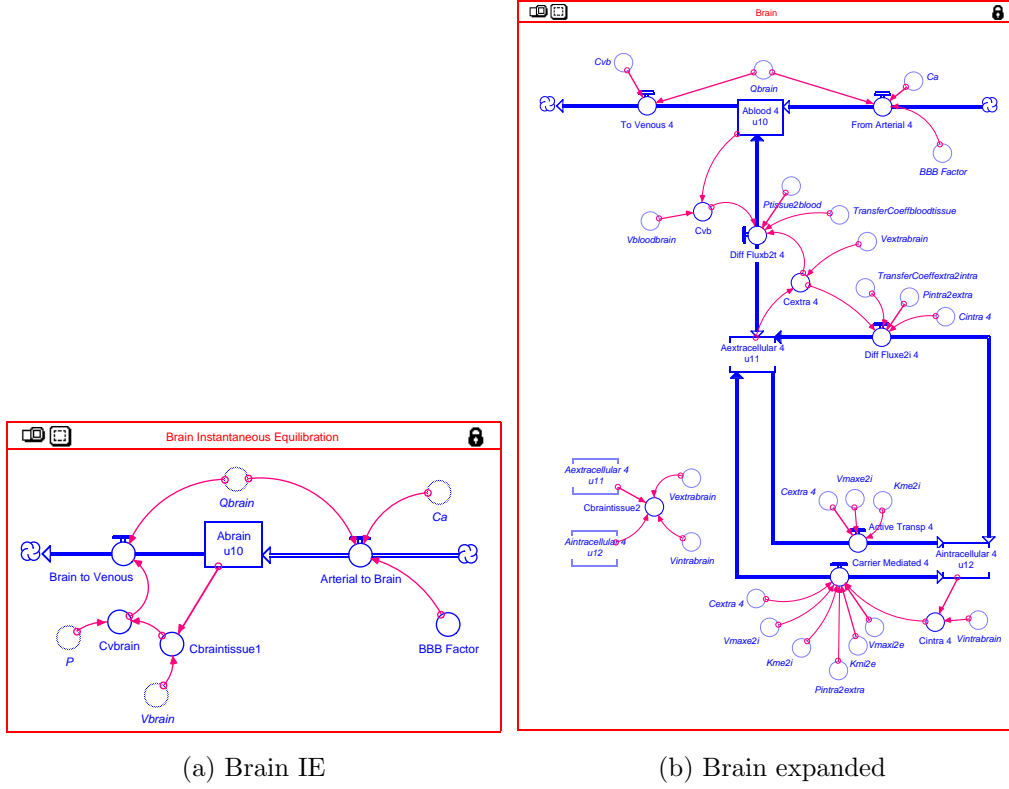


Figure 72. Brain IE and expanded models in STELLA®

Brain IE.

$$\frac{d(\text{Abrain } u10)}{dt} = \text{Arterial to Brain} - \text{Brain to Venous} \quad (59)$$

where

$$\text{Arterial to Brain} = Q_{\text{brain}} \times Ca \times \text{BBB Factor}$$

$$\text{Brain to Venous} = Q_{\text{brain}} \times Cv_{\text{brain}}$$

$$C_{\text{braintissue1}} = A_{\text{brain}} u_{10} / V_{\text{brain}}$$

$$C_{\text{vbrain}} = C_{\text{braintissue1}} / P$$

Brain (Expanded).

$$\frac{d(A_{\text{blood}} u_{10})}{dt} = \text{From Arterial} - \text{To Venous} - \text{Diff Flux}_{b2t} \quad (60)$$

where

$$\text{From Arterial} = \text{BBB Factor} \times Q_{\text{brain}} \times C_a$$

$$\text{To Venous} = Q_{\text{brain}} \times C_{\text{vb}}$$

$$\text{Diff Flux}_{b2t} = \text{TransferCoeff}_{\text{bloodtissue}} \times (C_{\text{vb}} - C_{\text{extra}} / P_{\text{tissue2blood}})$$

$$C_{\text{vb}} = A_{\text{blood}} u_{10} / V_{\text{bloodbrain}}$$

$$\begin{aligned} \frac{d(A_{\text{extracellular}} u_{11})}{dt} = & \text{Diff Flux}_{b2t} - \text{Carrier Mediated} \\ & - \text{Diff Flux}_{e2i} - \text{Active Transp} \end{aligned} \quad (61)$$

where

$$\text{Diff Flux}_{b2t} = \text{TransferCoeff}_{\text{bloodtissue}} \times (C_{\text{vb}} - C_{\text{extra}} / P_{\text{tissue2blood}})$$

$$\text{Carrier Mediated} = (V_{\text{maxe2i}} \times C_{\text{extra}} / (K_{\text{me2i}} + C_{\text{extra}}))$$

$$- V_{\text{maxi2e}} \times (C_{\text{intra}} / P_{\text{intra2extra}}) / (K_{\text{mi2e}} + C_{\text{intra}} / P_{\text{intra2extra}})$$

$$\text{Diff Flux}_{e2i} = \text{TransferCoeff}_{\text{extra2intra}} \times (C_{\text{extra}} - C_{\text{intra}} / P_{\text{intra2extra}})$$

$$\text{Active Transp } 4 = V_{\text{maxe2i}} \times C_{\text{extra } 4} / (K_{\text{me2i}} + C_{\text{extra } 4})$$

$$C_{\text{extra } 4} = A_{\text{extracellular } 4} u_{11} / V_{\text{extrabrain}}$$

$$C_{\text{intra } 4} = A_{\text{intracellular } 4} u_{12} / V_{\text{intrabrain}}$$

$$\frac{d(A_{\text{intracellular } 4} u_{12})}{dt} = \text{Carrier Mediated } 4 + \text{Diff Fluxe2i } 4 + \text{Active Transp } 4 \quad (62)$$

where

$$\text{Carrier Mediated } 4 = (V_{\text{maxe2i}} \times C_{\text{extra } 4} / (K_{\text{me2i}} + C_{\text{extra } 4})$$

$$- V_{\text{maxi2e}} \times (C_{\text{intra } 4} / P_{\text{intra2extra}}) / (K_{\text{mi2e}} + C_{\text{intra } 4} / P_{\text{intra2extra}})$$

$$\text{Diff Fluxe2i } 4 = \text{TransferCoeffextra2intra} \times (C_{\text{extra } 4} - C_{\text{intra } 4} / P_{\text{intra2extra}})$$

$$\text{Active Transp } 4 = V_{\text{maxe2i}} \times C_{\text{extra } 4} / (K_{\text{me2i}} + C_{\text{extra } 4})$$

RPT ODEs

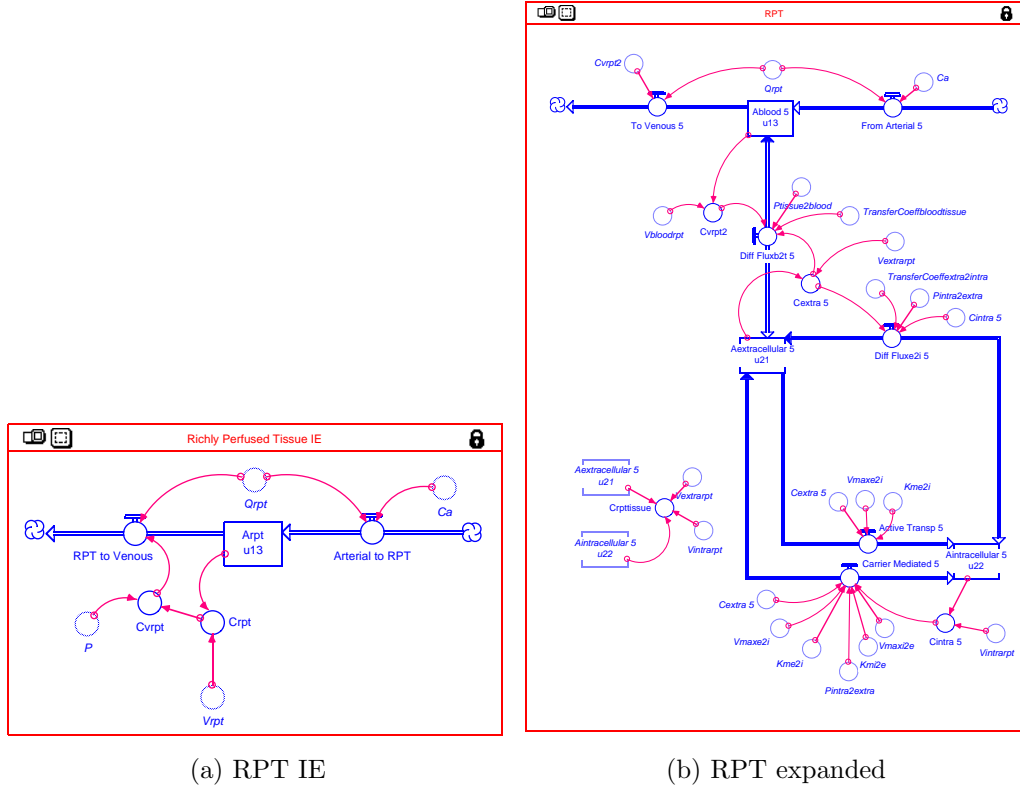


Figure 73. RPT IE and expanded models in STELLA®

RPT IE.

$$\frac{d(\text{Arpt } u13)}{dt} = \text{Arterial to RPT} - \text{RPT to Venous} \quad (63)$$

where

$$\text{Arterial to RPT} = Q_{rpt} \times Ca$$

$$\text{RPT to Venous} = Q_{rpt} \times C_{vrpt}$$

$$C_{rpt} = A_{rpt} u_{13} / V_{rpt}$$

$$C_{vrpt} = C_{rpt} / P$$

RPT (Expanded).

$$\frac{d(A_{blood} u_{13})}{dt} = \text{From Arterial } 5 - \text{To Venous } 5 - \text{Diff Flux}_{b2t} 5 \quad (64)$$

where

$$\text{From Arterial } 5 = Q_{rpt} \times C_a$$

$$\text{To Venous } 5 = Q_{rpt} \times C_{vrpt2}$$

$$\text{Diff Flux}_{b2t} 5 = \text{TransferCoeff}_{bloodtissue} \times (C_{vrpt2} - C_{extra} 5 / P_{tissue2blood})$$

$$C_{vrpt2} = A_{blood} u_{13} / V_{bloodrpt}$$

$$\begin{aligned} \frac{d(A_{extracellular} u_{21})}{dt} = & \text{Diff Flux}_{b2t} 5 - \text{Carrier Mediated } 5 \\ & - \text{Diff Flux}_{e2i} 5 - \text{Active Transp } 5 \end{aligned} \quad (65)$$

where

$$\text{Diff Flux}_{b2t} 5 = \text{TransferCoeff}_{bloodtissue} \times (C_{vrpt2} - C_{extra} 5 / P_{tissue2blood})$$

$$\text{Carrier Mediated } 5 = V_{maxe2i} \times C_{extra} 5 / (K_{me2i} + C_{extra} 5)$$

$$- V_{maxi2e} \times (C_{intra} 5 / P_{intra2extra}) / (K_{mi2e} + C_{intra} 5 / P_{intra2extra})$$

$$\text{Diff Flux}_{e2i} 5 = \text{TransferCoeff}_{extra2intra} \times (C_{extra} 5 - C_{intra} 5 / P_{intra2extra})$$

$$\text{Active Transp } 5 = V_{\text{maxe2i}} \times C_{\text{extra } 5} / (K_{\text{me2i}} + C_{\text{extra } 5})$$

$$C_{\text{extra } 5} = A_{\text{extracellular } 5} u_{21} / V_{\text{extrarpt}}$$

$$C_{\text{intra } 5} = A_{\text{intracellular } 5} u_{22} / V_{\text{intrarpt}}$$

$$\frac{d(A_{\text{intracellular } 5} u_{22})}{dt} = \text{Carrier Mediated } 5 + \text{Diff Fluxe2i } 5 + \text{Active Transp } 5 \quad (66)$$

where

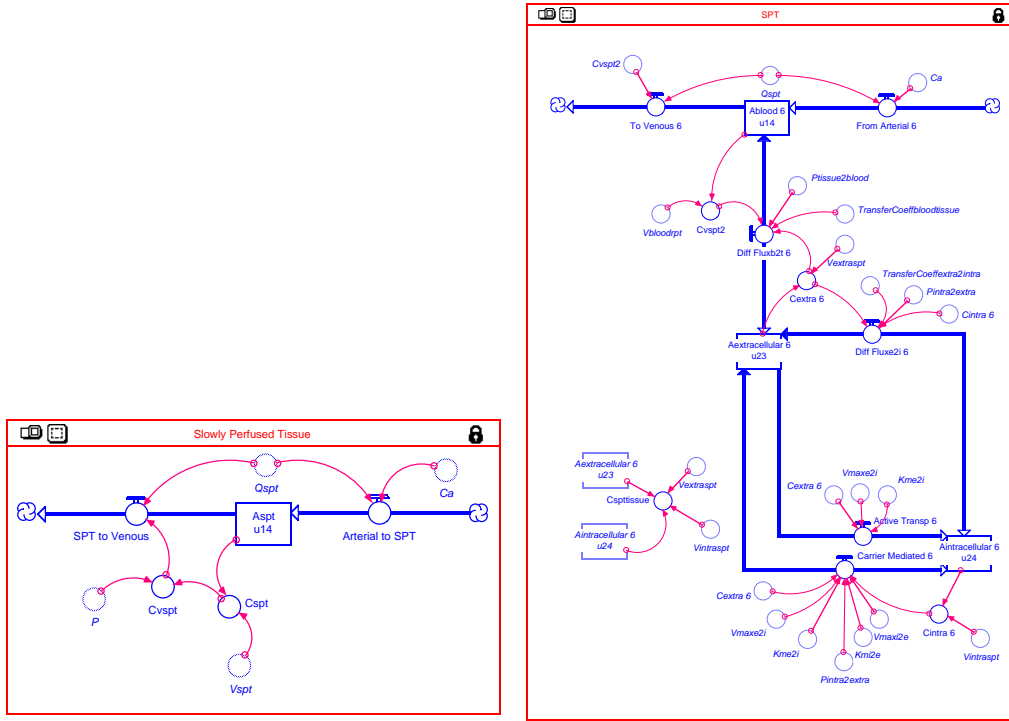
$$\text{Carrier Mediated } 5 = V_{\text{maxe2i}} \times C_{\text{extra } 5} / (K_{\text{me2i}} + C_{\text{extra } 5})$$

$$- V_{\text{maxi2e}} \times (C_{\text{intra } 5} / P_{\text{intra2extra}}) / (K_{\text{mi2e}} + C_{\text{intra } 5} / P_{\text{intra2extra}})$$

$$\text{Diff Fluxe2i } 5 = \text{TransferCoeffextra2intra} \times (C_{\text{extra } 5} - C_{\text{intra } 5} / P_{\text{intra2extra}})$$

$$\text{Active Transp } 5 = V_{\text{maxe2i}} \times C_{\text{extra } 5} / (K_{\text{me2i}} + C_{\text{extra } 5})$$

SPT ODEs



(a) SPT IE

(b) SPT expanded

Figure 74. SPT IE and expanded models in STELLA®

SPT IE.

$$\frac{d(\text{Aspt } u14)}{dt} = \text{Arterial to SPT} - \text{SPT to Venous} \quad (67)$$

where

$$\text{Arterial to SPT} = Q_{spt} \times Ca$$

$$\text{SPT to Venous} = Q_{spt} \times C_{vspt}$$

$$C_{spt} = A_{spt} u_{14} / V_{spt}$$

$$C_{vspt} = C_{spt} / P$$

SPT (Expanded).

$$\frac{d(\text{Ablood } 6 \text{ } u_{14})}{dt} = \text{From Arterial } 6 - \text{To Venous } 6 - \text{Diff Fluxb2t } 6 \quad (68)$$

where

$$\text{From Arterial } 6 = Q_{spt} \times C_a$$

$$\text{To Venous } 6 = Q_{spt} \times C_{vspt2}$$

$$\text{Diff Fluxb2t } 6 = \text{TransferCoeffbloodtissue} \times (C_{vspt2} - C_{extra} 6 / P_{tissue2blood})$$

$$C_{vspt2} = \text{Ablood } 6 \text{ } u_{14} / V_{bloodrpt}$$

$$\begin{aligned} \frac{d(\text{Aextracellular } 6 \text{ } u_{23})}{dt} = & \text{Diff Fluxb2t } 6 - \text{Carrie Mediated } 6 \\ & - \text{Diff Fluxe2i } 6 - \text{Active Transp } 6 \end{aligned} \quad (69)$$

where

$$\text{Diff Fluxb2t } 6 = \text{TransferCoeffbloodtissue} \times (C_{vspt2} - C_{extra} 6 / P_{tissue2blood})$$

$$\text{Carrier Mediated } 6 = V_{maxe2i} \times C_{extra} 6 / (K_{me2i} + C_{extra} 6)$$

$$- V_{maxi2e} \times (C_{intra} 6 / P_{intra2extra}) / (K_{mi2e} + C_{intra} 6 / P_{intra2extra})$$

$$\text{Diff Fluxe2i } 6 = \text{TransferCoeffextra2intra} \times (C_{extra} 6 - C_{intra} 6 / P_{intra2extra})$$

$$\text{Active Transp } 6 = V_{\text{maxe}2i} \times C_{\text{extra } 6} / (K_{\text{me}2i} + C_{\text{extra } 6})$$

$$C_{\text{extra } 6} = A_{\text{extracellular } 6} \cdot u_{23} / V_{\text{extraspt}}$$

$$C_{\text{intra } 6} = A_{\text{intracellular } 6} \cdot u_{24} / V_{\text{intraspt}}$$

$$\frac{d(A_{\text{intracellular } 6} \cdot u_{24})}{dt} = \text{Carrier Mediated } 6 + \text{Diff Fluxe}2i \ 6 + \text{Active Transp } 6 \quad (70)$$

where

$$\text{Carrier Mediated } 6 = V_{\text{maxe}2i} \times C_{\text{extra } 6} / (K_{\text{me}2i} + C_{\text{extra } 6})$$

$$- V_{\text{maxi}2e} \times (C_{\text{intra } 6} / P_{\text{intra}2\text{extra}}) / (K_{\text{mi}2e} + C_{\text{intra } 6} / P_{\text{intra}2\text{extra}})$$

$$\text{Diff Fluxe}2i \ 6 = \text{TransferCoeffextra}2\text{intra} \times (C_{\text{extra } 6} - C_{\text{intra } 6} / P_{\text{intra}2\text{extra}})$$

$$\text{Active Transp } 6 = V_{\text{maxe}2i} \times C_{\text{extra } 6} / (K_{\text{me}2i} + C_{\text{extra } 6})$$

Venous Blood Calculation

To maintain mass balance, we assume $\sum_{i=1}^n Q_i = Q_c$, where Q_c is cardiac output. Concentration in mixed venous blood, C_v , is taken as the weighted average of the concentrations from each organ.

$$\begin{aligned} C_v = & [(Q_{\text{portal}} + Q_{\text{liver}}) \times C_{\text{liver}} + Q_{\text{kidney}} \times C_{\text{kidney}} \\ & + Q_{\text{brain}} \times C_{\text{brain}} + Q_{\text{rpt}} \times C_{\text{rpt}} + Q_{\text{spt}} \times C_{\text{spt}}] / Q_c \end{aligned} \quad (71)$$

Appendix D. Matrix Formats for MATLAB® Model

This appendix describes the matrix formats for the baseline model created in Phase I Model Formulation in Section 3.1 on page 33. To assemble the A-matrix in MATLAB®, we use $A = \text{Input}_1 + \text{Input}_2 - \text{Output} + \text{Exchange} - \text{Loss}$, where Input_1 accounts for inputs into all organs except the lungs and Input_2 is for lungs only. This was done to better organize the coding in MATLAB®. Note that Input_1 , Input_2 , and Output remain the same, regardless of the transport process that is used (instantaneous equilibration, diffusion, active transport, or carrier mediated transport). Loss and Exchange may change, depending on the transport assumptions.

Throughout the MATLAB® code, variables ‘a’, ‘b’, ‘c’, and ‘d’ were used to represent groupings of coefficients. Descriptions of these variables is as follows:

- a=fraction of nanoparticles exiting each compartment (output)
- b=fraction of total blood flow to each compartment (input)
- c=fraction exchanged between two compartments (exchange)
- d=fraction excreted or otherwise lost from a compartment (loss)

The MATLAB® code is built around a 24×24 matrix format, with each row representing the ODE for a specific subcompartment (e.g., liver blood, liver extracellular, etc.). An index showing the row positions is shown in Figure 75 on the following page.

Below are the matrices for Input_1 , Input_2 , and Output . Input_1 accounts for inputs into all organs except the lungs and Input_2 is for lungs only.

1. liverblood
2. liverextracellular
3. liverintracellular
4. kidneyblood
5. kidneyextracellular
6. kidneyintracellular
7. spleenblood
8. spleenextracellular
9. spleenintracellular
10. brainblood
11. brainextracellular
12. brainintracellular
13. rptblood
14. sptblood
15. mucosa
16. alveolarair
17. alveolarsurface
18. alveolarblood
19. giblood
20. gilumen
21. rptextracellular
22. rptintracellular
23. sptextracellular
24. sptintracellular

Figure 75. Index for the 24 rows

[illegible]

(72)

(73)

[illegible]

4.0.0.2 Loss.

The Loss matrix is diagonal, as loss terms are written as first-order losses. See Equation 75.

[illegible]

The Loss matrix is different for IE vs. Diffusion/Active/Carrier Mediated as the loss mechanisms are more accurately placed at the subcompartment level for the latter three processes, as compared to IE which only has a single compartment. For Diffusion/Active/Carrier Mediated transport processes, note that in Equation 76 on the following page the losses d_1 and d_3 are in different locations, as they now leave from the extracellular subcompartment:

(76)

4.0.0.3 Exchange.

The Exchange matrix will differ depending on whether an assumption of IE, diffusion, active transport, or carrier mediated transport is assumed for each organ. As would be assumed based on its name, the exchange matrix terms always occur in pairs (vertically). For example, c_{16} is subtracted from row 1 and is added to row 20, which represents the “exchange” of nanoparticles between the liver and GI tract. The Exchange matrix for IE, in terms of coefficients c , is:

(77)

For the other transport processes, each organ is represented with three *subcompartments* instead of the single *compartment*. Exchanges between subcompartments are noted

with coefficients c_x . The three lines between the extracellular and intracellular subcompartments represent diffusion, active transport, and carrier mediated transport. For this research, we leave all three transport processes on simultaneously (i.e., processes operate in parallel). In the liver subcompartment, note also that c_{17} represents the bile exchange for these transport processes, whereas c_{16} applies for the IE case only.

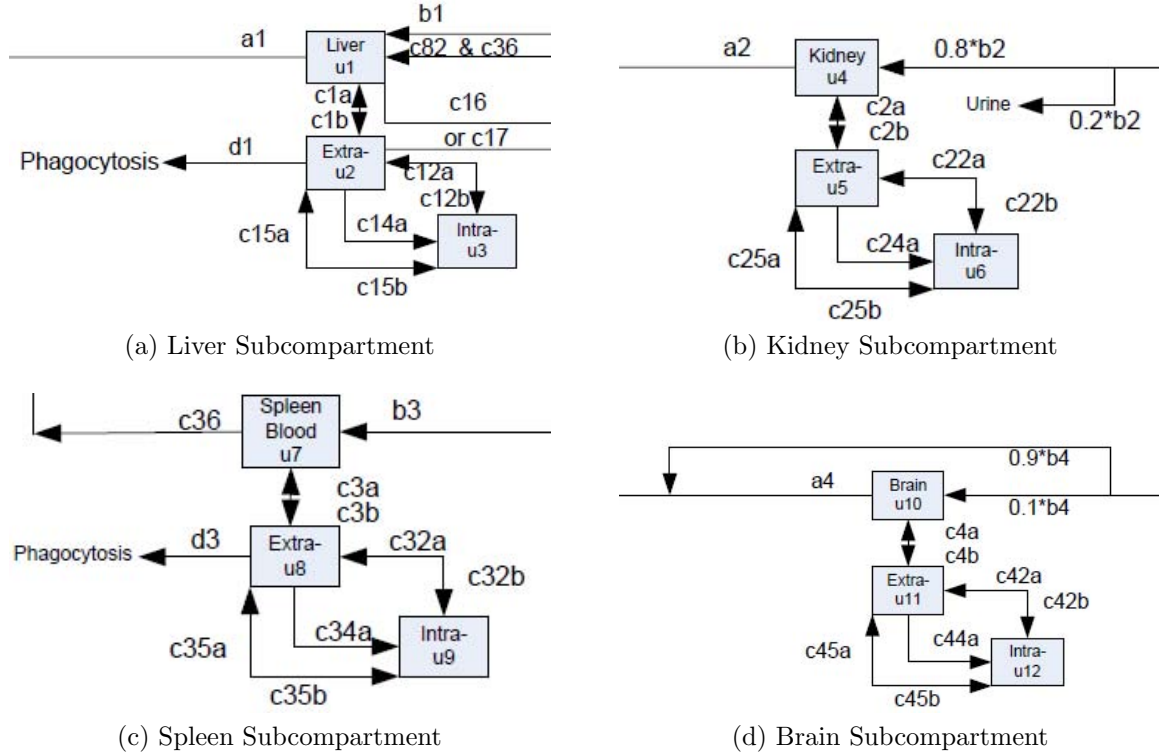


Figure 76. Liver, kidney, spleen, and brain subcompartments

For diffusion between extra- and intracellular, we can write the submatrices for the organs as follows:

$$\mathbf{Exchange}_{Liverdiff} = \begin{bmatrix} -c_{1a} & c_{1b} & 0 \\ c_{1a} & -c_{1b}-c_{17}-c_{12a} & c_{12b} \\ 0 & c_{12a} & -c_{12b} \end{bmatrix}$$

$$\mathbf{Exchange}_{Kidneydiff} = \begin{bmatrix} -c_{2a} & c_{2b} & 0 \\ c_{2a} & -c_{2b}-c_{22a} & c_{22b} \\ 0 & c_{22a} & -c_{22b} \end{bmatrix}$$

$$\mathbf{Exchange}_{\mathbf{Spleendiff}} = \begin{bmatrix} -c_{36}-c_{3a} & c_{3b} & 0 \\ c_{3a} & -c_{3b}-c_{32a} & c_{32b} \\ 0 & c_{32a} & -c_{32b} \end{bmatrix}$$

$$\mathbf{Exchange}_{\mathbf{Braindiff}} = \begin{bmatrix} -c_{4a} & c_{4b} & 0 \\ c_{4a} & -c_{4b}-c_{42a} & c_{42b} \\ 0 & c_{42a} & -c_{42b} \end{bmatrix}$$

Matrix formats for active transport and carrier mediated transport are assembled in a similar manner. One difference, however, is how to deal with the nonlinear terms associated with the Michaelis-Menten kinetics equation. If the system of ODEs is solved with those nonlinear terms as is, the major difference is that exchanges between extracellular and intracellular are no longer linear functions of concentration and the exchange terms need to be added outside of the A-matrix. In other words, the linear relationship $A \cdot \vec{c}$ no longer applies. Alternatively, the nonlinear terms can be linearized, such as by using a first- or zero-order assumption as discussed in Section 4.1.3 on page 103. Any resulting first-order terms would be included in the A-matrix and zero order terms would be added outside the A-matrix.

Appendix E. Eigenvalue Analysis Background

Derivation of the Steady State Solution

In this appendix, the solution to the linear system of differential equations shown in Equation 79 is determined.

$$\dot{\vec{c}} = A\vec{c} + \vec{s}(t), \text{ where } \vec{c}(0) = \vec{c}_o \quad (79)$$

The solution method will use the properties of eigenvalues and their associated normalized eigenvectors. To this end, we assume there is a complete set of linearly independent eigenvectors $\{\vec{v}_i\}_{i=1}^n$ associated with eigenvalues $\{\lambda_i\}_{i=1}^n$ for matrix A , such that

$$A\vec{v}_i = \lambda_i\vec{v}_i, \quad i = 1, 2, \dots, n \quad (80)$$

The eigenvectors are chosen so that $\vec{v}_i^T \vec{v}_i = 1$ (i.e., the transpose of the eigenvector applied on the eigenvector=1). Next, we define the matrix of eigenvectors, E , as:

$$E = \left[\vec{v}_1 \mid \vec{v}_2 \mid \dots \mid \vec{v}_n \right] \quad (81)$$

From this we observe

$$AE = \left[A\vec{v}_1 \mid A\vec{v}_2 \mid \dots \mid A\vec{v}_n \right] \quad (82a)$$

$$= \left[\lambda_1\vec{v}_1 \mid \lambda_2\vec{v}_2 \mid \dots \mid \lambda_n\vec{v}_n \right] = E\Lambda \quad (82b)$$

where

$$\Lambda = \begin{bmatrix} \lambda_1 & & & \\ & \lambda_2 & & \\ & & \ddots & \\ & & & \lambda_n \end{bmatrix} \quad (83)$$

is the diagonal matrix of eigenvalues. Because the eigenvectors are linearly independent, E^{-1} exists and it follows that

$$A = E\Lambda E^{-1} \quad (84)$$

Returning to the solution of Equation 79 on the preceding page, we introduce the coordinate transformation

$$\vec{c}(t) = E\vec{y}(t) \quad (85)$$

This leads to

$$\dot{\vec{c}} = E\dot{\vec{y}} = AE\vec{y} + \vec{s}(t), \quad \vec{c}(0) = E\vec{y}(0) = \vec{c}_o \quad (86)$$

Then by using Equation 84 we have

$$\dot{\vec{y}} = \Lambda\vec{y} + E^{-1}\vec{s}(t), \quad \vec{y}(0) = E^{-1}\vec{c}_o \quad (87)$$

This equation is now an uncoupled system of equations; that is, we may simply write it as

$$\dot{y}_k(t) = \lambda_k y_k(t) + f_k(t), \quad y_k(0) = b_k \quad k = 1, 2, \dots, n \quad (88)$$

where $f_k(t) = (E^{-1}\vec{s})_k$, the k^{th} element of the vector $E^{-1}\vec{s}(t)$ and $b_k = (E^{-1}\vec{c}_o)_k$. This equation has the solution

$$\vec{y}(t) = e^{\Lambda_k t} b_k + \int_0^t e^{\lambda_k(t-\tau)} f_k(\tau) d\tau. \quad (89)$$

Thus, the solution to Equation 87 becomes

$$y_k(t) = e^{\Lambda t} E^{-1} \vec{c}_o + \int_0^t e^{\Lambda(t-\tau)} E^{-1} \vec{s}(\tau) d\tau. \quad (90)$$

Applying Equation 85 produces the desired solution

$$\vec{c}(t) = E e^{\Lambda t} E^{-1} \vec{c}_o + \int_0^t E e^{\Lambda(t-\tau)} E^{-1} \vec{s}(\tau) d\tau. \quad (91)$$

or

$$\vec{c}(t) = \sum_{k=1}^n \vec{v}_k y_k(t) \quad (92a)$$

$$= \sum_{k=1}^n b_k \vec{v}_k e^{\lambda_k t} + \sum_{k=1}^n \vec{v}_k \int_0^t e^{\lambda_k(t-\tau)} f_k(\tau) d\tau. \quad (92b)$$

Next, we examine the solution in the context of this research, which focuses on concentration. First, assume the source vector $\vec{s}(t)$ is constant, then f_k is constant and the integral in Equation 92b can be evaluated to produce the solution

$$\vec{c}(t) = \sum_{k=1}^n b_k \vec{v}_k e^{\lambda_k t} + \sum_{k=1}^n \frac{f_k}{\lambda_k} (e^{\lambda_k t} - 1) \vec{v}_k. \quad (93)$$

The first sum represents the evolution due to the initial concentration \vec{c}_o , while the second sum represents the evolution due to the constant source, \vec{s} . The evolution of the concentration vector is clearly governed by the sign and size of the eigenvalues, λ_k . If λ_k is positive, we have exponential *growth*, while a negative λ_k produces exponential *decay*. In the context of this research, however, all of the eigenvalues λ are negative. Therefore, the first summation term of Equation 93 decays away and is not a major

contributor to long-term concentration. We can rewrite the equation as

$$\vec{c}(t) \approx \sum_{k=1}^n \frac{f_k}{\lambda_k} (e^{\lambda_k t} - 1) \vec{v}_k = \sum_{k=1}^n \frac{f_k}{-\lambda_k} (1 - e^{\lambda_k t}) \vec{v}_k. \quad (94)$$

On the other hand, the second term in Equation 93 evolves into the steady state concentration which can also be found by setting $\dot{\vec{c}}=0$ in Equation 79 on page 167 and solving for \vec{c}_{ss} (steady state), i.e.,

$$\vec{c}_{ss} = -A^{-1} \vec{s} = \sum_{k=1}^n \frac{f_k}{-\lambda_k} \vec{v}_k. \quad (95)$$

It is convenient to choose \vec{v}_k so that every component of \vec{f} is positive. This can be done by simply observing if $-f_k < 0$ then $f_k > 0$ and $f_k \cdot v_k = (-f_k)(-v_k)$ so we replace v_k with $-v_k$, if f_k is negative.

A Steady State Example

For the kidney example first described in Section 3.1.5.4 on page 55 and shown again in Figure 77 on the next page, the mass balance differential equation is written in general terms as shown in Equation 96a. The input, output, and exchange terms can be combined to form the A-matrix as they are linear terms. However, the source term is not linearly dependent and must be kept separate. Note that the source term flows into the kidney blood subcompartment.

$$V \frac{d}{dt} \begin{bmatrix} C_b \\ C_e \\ C_i \end{bmatrix} = \text{Input} - \text{Output} + \text{Exchange} + \text{Source} \quad (96a)$$

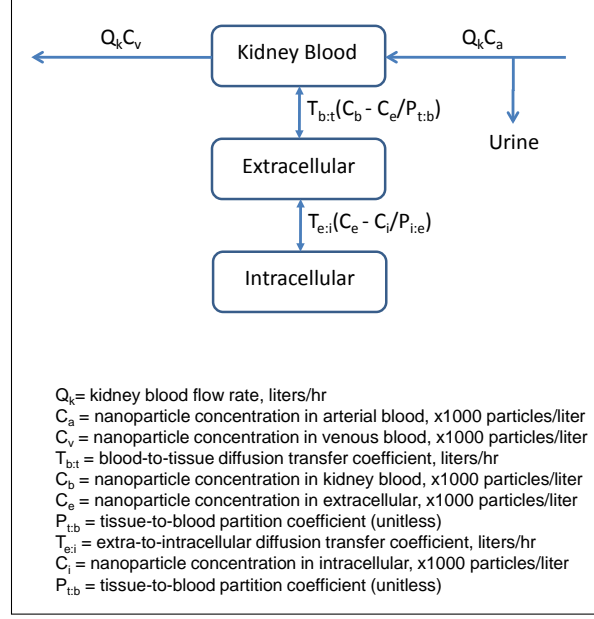


Figure 77. Example used for eigenvalue analysis

$$\Rightarrow \frac{d}{dt} \begin{bmatrix} C_b \\ C_e \\ C_i \end{bmatrix} = \cdots = \begin{bmatrix} & & \\ & A & \\ & & \end{bmatrix} \begin{bmatrix} C_b \\ C_e \\ C_i \end{bmatrix} + \begin{bmatrix} s \\ 0 \\ 0 \end{bmatrix} \quad (96b)$$

Using Equation 16 on page 56 and substituting in values for the parameters, the A-matrix equals:

$$A = \begin{bmatrix} \frac{-T_{b:t} - 0.2 \cdot Q_k}{V_b} & \frac{T_{b:t}}{P_{t:b} V_b} & 0 \\ \frac{T_{b:t}}{V_e} & -\frac{T_{b:t}}{P_{t:b} V_e} - \frac{T_{e:i}}{V_i} & \frac{T_{e:i}}{P_{i:e} V_e} \\ 0 & \frac{T_{e:i}}{V_i} & -\frac{T_{e:i}}{P_{i:e} V_i} \end{bmatrix} = \begin{bmatrix} -595.8 & 83.06 & 0 \\ 33.2 & -23.26 & 2.2 \\ 0 & 8.31 & -2.77 \end{bmatrix} \quad (97)$$

Assuming an inhalation concentration of $C_{inh}=500$ (x1000 particles/liter) and blood volume $V_b= 0.0301$ liters, the source vector can be written as shown in Equation 98. Note that the blood volume, V_b , appears in the denominator as the linear

system is multiplied by V^{-1} to clear volume from the left-hand side of the ODEs.

$$\vec{s} = \begin{bmatrix} \frac{C_{\text{inh}}}{V_b} \\ 0 \\ 0 \end{bmatrix} = \begin{bmatrix} \frac{500}{0.0301} \\ 0 \\ 0 \end{bmatrix} = \begin{bmatrix} 16611 \\ 0 \\ 0 \end{bmatrix} \quad (98)$$

Previously in Figure 16c on page 57, the eigenvalues were displayed using the L1-norm, where the components are fractions which sum to one for each eigenvector. Figure 78 displays the eigenstructure with eigenvectors written using the L2-norm (i.e., sum of squares of the components equals one).

$$\begin{bmatrix} \mathbf{-600.6} & \mathbf{-19.56} & \mathbf{-1.682} \\ -0.9983 & -0.1281 & 0.0181 \\ 0.0575 & -0.8890 & 0.1297 \\ -0.0008 & 0.4397 & 0.9914 \end{bmatrix}$$

Figure 78. Eigenstructure (using L2 norm)

Therefore, we have

$$E = \begin{bmatrix} -0.9983 & -0.1281 & 0.0181 \\ 0.0575 & -0.8890 & 0.1297 \\ -0.0008 & 0.4397 & 0.9914 \end{bmatrix} \Rightarrow E^{-1} = \begin{bmatrix} -0.9934 & 0.1429 & -0.0005 \\ -0.0604 & -1.0478 & 0.1382 \\ 0.0260 & 0.4648 & 0.9474 \end{bmatrix} \quad (99)$$

The L2-norm of the eigenvectors can then be used to write the general solution to the system of ODEs for this example. First, we solve for \vec{f} by applying the inverse of the eigenvector matrix, E , onto the source vector, \vec{s} :

$$\vec{f} = E^{-1} \cdot \vec{s} \quad (100a)$$

$$\Rightarrow \vec{f} = \begin{bmatrix} -0.9934 & 0.1429 & -0.0005 \\ -0.0604 & -1.0478 & 0.1382 \\ 0.0260 & 0.4648 & 0.9474 \end{bmatrix} \begin{bmatrix} 16611 \\ 0 \\ 0 \end{bmatrix} = \begin{bmatrix} -16502 \\ -1003 \\ 432 \end{bmatrix} \quad (100b)$$

To make all terms in \vec{f} positive, we multiply the corresponding eigenvector in the E-matrix by '-1'. Since the first two terms of \vec{f} are negative, we multiply the first two eigenvectors (i.e., columns) of E by '-1':

$$\text{new}\vec{f} = \begin{bmatrix} 16502 \\ 1003 \\ 432 \end{bmatrix} \Rightarrow \text{new}E = \begin{bmatrix} 0.9934 & -0.1429 & -0.0005 \\ 0.0604 & 1.0478 & 0.1382 \\ -0.0260 & -0.4648 & 0.9474 \end{bmatrix} \quad (101)$$

Equation 102 shows the concentration in the blood subcompartment as a function of time, using the values for f_k , λ_k , and v_k and Equation 94 on page 170.

$$\begin{aligned} C_b(t) &= \frac{f_1}{-\lambda_1} (1 - e^{\lambda_1 t}) (\vec{v}_{11}) + \frac{f_2}{-\lambda_2} (1 - e^{\lambda_2 t}) (\vec{v}_{21}) + \frac{f_3}{-\lambda_3} (1 - e^{\lambda_3 t}) (\vec{v}_{31}) \\ &= \frac{16502}{600.6} (1 - e^{-600.6t}) (0.9983) + \frac{1003}{19.56} (1 - e^{-19.56t}) (0.1281) \\ &\quad + \frac{432}{1.682} (1 - e^{-1.682t}) (0.0181) \end{aligned} \quad (102)$$

Once solved, the concentration equations for the blood subcompartment is as shown in Equation 103a. Equations for the extracellular and intracellular subcompartments are shown in Equations 103b and 103c, respectively.

$$C_b(t) = 27.43 (1 - e^{-600.6t}) + 6.57 (1 - e^{-19.56t}) + 4.65 (1 - e^{-1.682t}) \quad (103a)$$

$$C_e(t) = -1.58 (1 - e^{-600.6t}) + 45.6 (1 - e^{-19.56t}) + 33.3 (1 - e^{-1.682t}) \quad (103b)$$

$$C_i(t) = 0.022 (1 - e^{-600.6t}) - 22.55 (1 - e^{-19.56t}) + 254.5 (1 - e^{-1.682t}) \quad (103c)$$

Each concentration equation (Equations 103a - 103c) has three terms, with each

one corresponding to a specific eigenvalue. Figure 79 shows the total concentration plots (black lines) alongside plots for the three contributing components in each sub-compartment. We note that both extracellular and intracellular have terms that provide *negative contribution* to total concentration, as shown by plots extending into the negative y-direction. These negative terms are also indicated by the negative coefficients in Equations 103a - 103c.

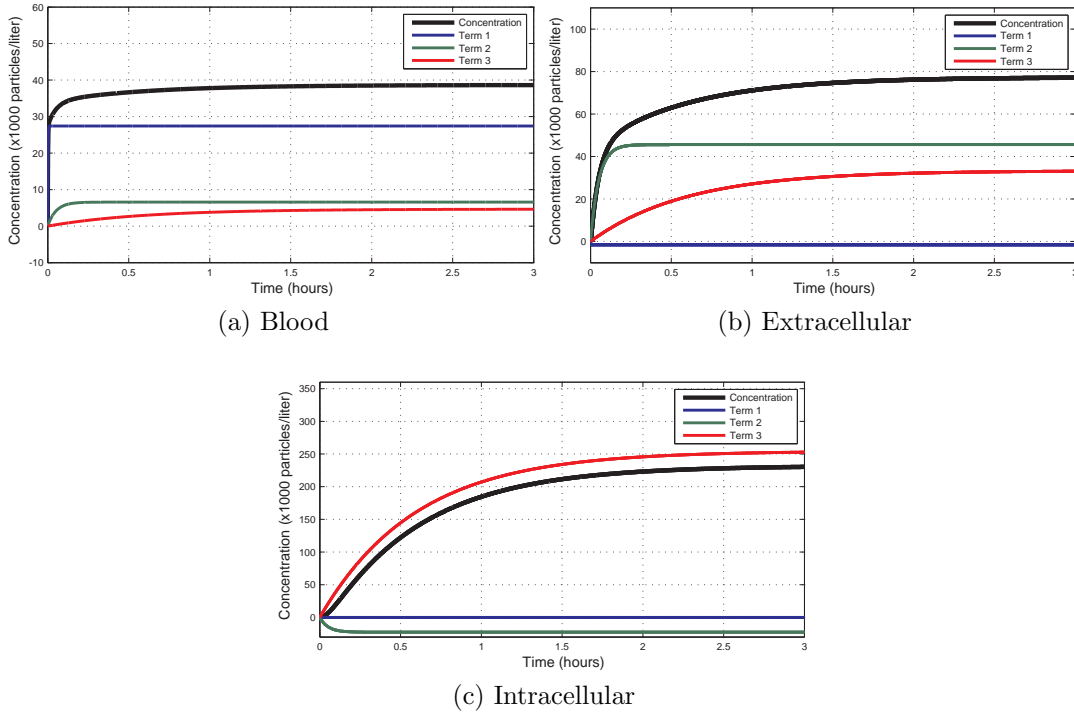


Figure 79. Contributions of exponential terms and total concentration in kidney sub-compartments

Figure 80 shows a comparison of the subcompartment concentrations shown in Figure 79. Note that the slight s-shaped pattern for intracellular (red line) in Figure 80 indicates the effect of a negative contribution term, which slows down the evolution of concentration at low t . At higher t , the effect of this term is more difficult to discern visually.

By recognizing that the exponential terms $\rightarrow 0$ as $t \rightarrow \infty$, we see that the con-

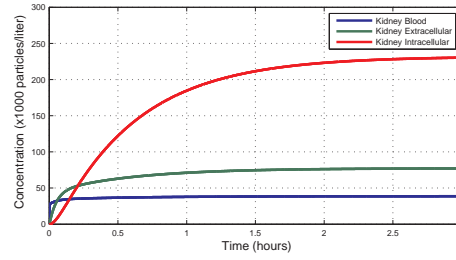


Figure 80. Comparison of subcompartments

centrations are approximately equal to the sum of the coefficients in Equations 103a - 103c, which yields $C_b(t) \approx 38.65$, $C_e(t) \approx 77.32$, and $C_i(t) \approx 231.97$. Alternatively, we can estimate these steady state concentrations by using Equation 95 on page 170 or by looking at the concentration values on the right side of the plots in Figure 79 on the previous page.

Appendix F. Eigenstructure Matrices

- $$\left(\begin{array}{l} 1. \textit{eigenvalue} \\ 2. \textit{liverblood} \\ 3. \textit{liverextracellular} \\ 4. \textit{liverintracellular} \\ 5. \textit{kidneyblood} \\ 6. \textit{kidneyextracellular} \\ 7. \textit{kidneyintracellular} \\ 8. \textit{spleenblood} \\ 9. \textit{spleenextracellular} \\ 10. \textit{spleenintracellular} \\ 11. \textit{brainblood} \\ 12. \textit{brainextracellular} \\ 13. \textit{brainintracellular} \\ 14. \textit{rptblood} \\ 15. \textit{sptblood} \\ 16. \textit{mucosa} \\ 17. \textit{alveolarair} \\ 18. \textit{alveolarsurface} \\ 19. \textit{alveolarblood} \\ 20. \textit{giblood} \\ 21. \textit{gilumen} \\ 22. \textit{rptextracellular} \\ 23. \textit{rptintracellular} \\ 24. \textit{sptextracellular} \\ 25. \textit{sptintracellular} \end{array} \right)$$

Figure 81. Index showing which subcompartments correspond to which rows

$$\begin{pmatrix}
-2.44e+003 & -1.01e+003 & -679 & -591 & -460 & -316 & -293 & -259 & -94 & -21.6 & -15.5 & -11.7 & -6.73 & -3 & -2 & -1.95 & -0.288 & -0.135 & -0.0865 & -0.0272 & -0.0257 & -0.018 & -0.0148 & -0.000806 \\
0 & 0 & -0.166 & 0 & 0 & 0.441 & -0.157 & -0.332 & -0.17 & 0 & 0 & 0 & 0 & 0 & 0 & 0 & 0 & 0 & 0 & 0 & 0 & 0 & 0 & 0 \\
0 & 0 & 0 & 0 & 0 & 0 & 0 & 0 & 0 & -0.0919 & 0 & -0.874 & 0 & 0 & 0 & 0 & 0 & 0 & 0 & 0 & 0 & 0 & -1 & 0 \\
0.461 & 0 \\
0 & 0 & 0 & 0 & 0 & 0 & 0 & 0 & 0 & 0 & -0.577 & 0 & 0 & 0 & 0 & 0 & 0 & -0.861 & 0 & 0 & 0 & 0 & 0 \\
0 & 0 \\
0 & 0 & 0.193 & 0 \\
0 & 0 & -0.108 & 0 & 0 & 0 & 0 & 0 & 0 & 0.627 & 0 & 0 & 0 & 0 & 0 & 0 & -1 & 0 & 0 & 0 & 0 & 0 & 0 \\
0 & 0 \\
0 & 0 & 0 & 0 & 0 & 0 & 0.515 & 0 & 0 & 0 & 0 & 0 & 0 & 0.684 & 0 & 0 & 0 & 0 & 0 & 0 & 0 & 0 & 0 \\
0 & 0 & 0 & 0 & 0 & 0 & 0 & 0 & 0 & 0 & 0 & 0 & 0 & 0 & 0 & 0 & 0 & 0 & -1 & 0 & 0 & 0 & 0 \\
0 & 0 & 0 & 0 & 0 & -0.38 & -0.328 & 0.409 & -0.131 & 0 & 0 & 0 & 0 & 0 & 0 & 0 & 0 & 0 & 0 & 0 & 0 & 0 & 0 & 0 \\
0 & 0 & -0.0965 & 0.213 & 0 & 0 & 0 & 0 & 0.245 & -0.281 & 0.423 & 0.126 & 0.87 & 0.176 & 0 & -0.138 & 0 & 0 & 0 & 0 & 0 & 0 & 0 & 0 \\
0 & 0 & -0.0459 & 0.0906 & 0 & 0 & 0 & 0 & 0 & 0 & 0 & 0 & 0 & 0 & 0 & 0 & 0 & 0 & 0 & 1 & 0 & 0 & 0 & 0 \\
0 & 0 & 0 & 0 & 0.624 & 0 & 0 & 0 & 0 & 0 & 0 & 0 & 0 & 0 & 0 & 0 & 0 & 0 & 0 & 0 & 0 & 0 & 0 & 0 \\
0 & 0 & 0 & 0 & -0.376 & 0 & 0 & 0 & 0 & 0 & 0 & 0 & 0 & 0 & -1 & 0 & 0 & 0 & 0 & 0 & 0 & 0 & 0 & 0 \\
-0.539 & 0 & 0.317 & -0.543 & 0 & 0.0931 & 0 & 0.0955 & -0.211 & 0 & 0 & 0 & 0 & 0 & 0 & 0 & 0 & 0 & 0 & 0 & 0 & 0 & 0 & 0 \\
0 & 0 & -0.0736 & 0.154 & 0 & -0.0854 & 0 & -0.163 & -0.243 & 0 & 0 & 0 & 0 & 0 & 0 & 0 & 0 & 0 & 0 & 0 & 0 & 0 & 0 & 0 \\
0 & 0 & 0 & 0 & 0 & 0 & 0 & 0 & 0 & 0 & 0 & 0 & 0 & -0.14 & 0 & -0.862 & 0 & 0 & 0 & 0 & 0 & 0 & 0 & 0 \\
0 & 1 & 0 & 0 & 0 \\
0 & 0 & 0 & 0 & 0 & 0 & 0 & 0 & 0 & 0 & 0 & 0 & -0.13 & 0 & 0 & 0 & 0 & 0.139 & -1 & 0 & 0 & 0 & 0 & 0 \\
0 & 1
\end{pmatrix}$$

Figure 82. Eigenstructure for $T_{e,i}=0.05$

$$\begin{pmatrix}
-2.44e+003 & -2.44e+003 & -1.01e+003 & -679 & -591 & -460 & -316 & -293 & -259 & -94.1 & -28.6 & -18.7 & -12 & -6.83 & -3.66 & -2.39 & -2.16 & -2 & -1.11 & -0.223 & -0.148 & -0.144 & -0.106 & -0.0257 & -0.00658 \\
0 & 0 & 0 & -0.166 & 0 & 0 & -0.441 & -0.157 & 0.332 & -0.17 & 0 & 0 & 0 & 0 & 0 & 0 & 0 & 0 & 0 & 0 & 0 & 0 & 0 & 0 \\
0 & 0 & 0 & 0 & 0 & 0 & 0 & 0 & 0 & 0 & 0 & 0 & -0.882 & 0 & 0 & 0 & 0 & 0 & 0 & 0 & 0 & 0 & 0 & 0 \\
0.461 & 0 & 0 & 0 & 0 & 0 & 0 & 0 & 0 & 0 & 0 & 0 & 0 & 0 & 0 & 0 & 0 & 0 & 0 & 0 & -1 & 0 & 0 & 0 \\
0 & 0 & 0 & 0 & 0 & 0 & 0 & 0 & 0 & 0 & 0 & -0.574 & 0 & 0 & 0 & 0 & 0 & 0 & 0 & 0 & 0 & 0 & 0 & 0 \\
0 & 0 & 0 & 0 & 0 & 0 & 0 & 0 & 0 & 0 & 0 & 0.11 & 0 & 0 & 0 & 0 & 0 & -1 & 0 & 0 & 0 & 0 & 0 & 0 \\
0 & 0 & 0 & 0.193 & 0 & 0 & 0 & 0 & 0 & 0 & 0.615 & 0 & 0 & 0 & 0 & 0 & -0.0636 & 0 & 0 & 0 & 0 & 0 & 0 & 0 \\
0 & 0 & 0 & -0.109 & 0 & 0 & 0 & 0 & 0 & 0 & -0.172 & 0 & 0 & 0 & 0 & 0 & -0.554 & 0 & 0 & 0 & 0 & 0 & 0 & 0 \\
0 & 0 & 0 & 0 & 0 & 0 & 0 & 0.515 & 0 & 0 & 0 & 0 & 0 & 0 & 0 & 0 & 0 & 0 & 0 & 0 & 0 & 0 & 0 & 0 \\
0 & 0 & 0 & 0 & 0 & 0 & 0 & 0 & 0 & 0 & 0 & 0 & 0 & 0 & -0.594 & 0 & 0 & 0 & 0.896 & 0 & 0 & 0 & 0 & 0 \\
0 & 0 & 0 & 0 & 0 & 0 & 0.38 & -0.328 & -0.409 & -0.131 & 0 & 0 & 0 & 0 & 0.117 & 0 & 0 & 0 & 0 & 0 & 0 & 0 & 0 & 0 & 0 \\
0 & 0 & 0 & -0.0962 & -0.213 & 0 & 0 & 0 & 0 & 0.245 & -0.214 & 0.315 & 0.118 & -0.871 & -0.183 & -0.118 & -0.119 & 0 & 0 & 0 & 0 & 0 & 0 & 0 & 0 \\
0 & 0 & 0 & -0.0458 & -0.0906 & 0 & 0 & 0 & 0 & 0 & 0 & 0 & 0 & 0 & 0 & 0 & 0 & 0 & 0 & 0 & 0 & 0 & 0 & 0 \\
0 & 0 & 0 & 0 & 0 & 0.624 & 0 & 0 & 0 & 0 & 0 & 0 & 0 & 0 & 0 & 0 & 0 & 0 & 0 & 0 & 0 & 0 & 0 & 0 \\
0 & 0 & 0 & 0 & 0 & -0.376 & 0 & 0 & 0 & 0 & 0 & 0 & 0 & 0 & 0 & 0 & 1 & 0 & 0 & 0 & 0 & 0 & 0 & 0 \\
-0.539 & 0 & 0 & 0.316 & 0.543 & 0 & -0.0931 & 0 & -0.0955 & -0.211 & 0 & 0 & 0 & 0 & 0 & 0 & 0 & 0 & 0 & 0 & 0 & 0 & 0 & 0 & 0 \\
0 & 0 & 0 & -0.0734 & -0.154 & 0 & 0.0854 & 0 & 0.163 & -0.243 & 0 & 0 & 0 & 0 & 0 & 0 & 0 & 0 & 0 & 0 & 0 & 0 & 0 & 0 & 0 \\
0 & 0 \\
0 & 0 & 0 & 0 & 0 & 0 & 0 & 0 & 0 & 0 & 0 & 0 & 0 & 0 & 0.106 & -0.735 & -0.263 & 0 & 0 & 0 & 0 & 0 & 0 & 0 & 0 \\
0 & 0 & 0 & 0 & 0 & 0 & 0 & 0 & 0 & 0 & 0 & 0 & 0 & 0 & 0 & 0.147 & 0 & 0 & 0 & -0.821 & 0 & 0 & 0 & 0 & 0 \\
0 & 0 & 0 & 0 & 0 & 0 & 0 & 0 & 0 & 0 & 0 & 0 & 0 & 0.129 & 0 & 0 & 0 & 0 & -0.104 & 0.179 & -0.831 & -0.831 & 0 & 0 & 0 \\
0 & 0 & 0 & 0 & 0 & 0 & 0 & 0 & 0 & 0 & 0 & 0 & 0 & 0 & 0 & 0 & 0 & 0 & 0 & 0.169 & 0.169 & 0 & 0 & 0 & 1
\end{pmatrix}$$

Figure 83. Eigenstructure for $T_{ei}=0.5$

-2.44e+003	-0.166	-0.082	-590	-400	-316	-293	-259	-115	-93.1	-58.1	-15.6	-11.7	-7.99	-6.9	-5.3	-3.45	-2	-1.11	-0.699	-0.459	-0.344	-0.0257	-0.0202
0	0	0	0	0	-0.441	-0.157	-0.332	0.0508	0.172	0	0	0	0	0	0	0	0	0	0	0	0	0	
0	0	0	0	0	0	0	0	0	0	0	0.798	0	0	0	0	0	0	0.0956	0	0	0	0	
-0.461	0	0	0	0	0	0	0	0	0	-0.202	0	0	0	0	0	0	0	0.904	0	0	0	0	
0	0	0	0	0	0	0	0	0	0.506	0	0	0	0	0	0	0.146	0	0	0	0	0	0	
0	0	0	0	0	0	0	0	0	-0.379	0	0	0	0	0	-0.0527	0.465	0	0	0	0	0	0	
0	0.194	0	0	0	0	0	0	-0.341	0	0	0	0	0	0	0.106	0	0	0	0	0	0	0	
0	-0.123	0	0	0	0	0	0	0.284	0	0	0	0	0	0.308	0	0	0	0	0	0	0	0	
0	0	0	0	0	0	0.515	0	0	0	0	0	0	0	0	0	0	0	0	0	0	0	0	
0	0	0	0	0	0	0	0	0	0	0	0	-0.501	0	0	0	0	0	0	-0.197	0	0	0	
0	0	0	0	0	0	0	0	0	0	0	0	0.375	0	0	0	0	0	0	-0.632	0	0	0	
0	-0.0932	-0.213	0	0	0.38	-0.328	0.409	0.0553	0.13	0	0	0.124	-0.318	0.578	0.349	0.251	0	0	0	0	0	0	
0	-0.0445	-0.0906	0	0	0	0	0	-0.0734	-0.247	-0.114	0	0	0	0	0	0	0	0	0	0	0	0	
0	0	0	0	0.624	0	0	0	0	0	0	0	0	0	0	0	0	0	0	0	0	1	0	
0	0	0	0	-0.376	0	0	0	0	0	0	0	0	0	0	0	0	-1	0	0	0	0	0	
0.539	0.308	0.542	0	-0.0933	0	0	0.0954	0.0794	0.211	0	0	0	0	0	0	0	0	0	0	0	0	0	
0	-0.0711	-0.154	0	0.0855	0	-0.163	0.116	0.24	0.24	0	0	0	0	0	0	0	0	0	0	0	0	0	
0	0	0	0	0	0	0	0	0	0	0	0	0	0	0	0	0	0	0	0	0	0	0	
0	0	0	0	0	0	0	0	0	0	0	0	0	0.396	0.179	0.0509	0	0	0	-0.18	0	0	0	
0	0	0	0	0	0	0	0	0	0	-0.285	-0.156	-0.285	-0.156	-0.0652	-0.059	0	0	0.0869	-0.575	0	0	0	
0	0	0	0	0	0	0	0	0	0	0	0	0	-0.0867	-0.069	-0.079	0	0	0.0834	0.161	0.569	0	0.239	
0	0	0	0	0	0	0	0	0	0	0	0	0	0	0	0	0	0	0	-0.0844	-0.431	0	0.761	

Figure 84. Eigenstructure for $T_{\text{ei}}=5$

Bibliography

- [1] Alberts, Bruce, Alexander Johnson, Julian Lewis, Martin Raff, Keith Roberts, and Peter Walter. *Molecular Biology of The Cell*. Garland Science, New York NY, 2002.
- [2] Alexander, Andrew J. *Carbon Nanotube Structures and Compositions: Implications for Toxicological Studies*, 7–18. Nanotoxicology: Characterization, Dosing and Health Effects. Informa Healthcare USA, New York NY, 1st edition, 2007.
- [3] Andersen, Melvin E. “Toxicokinetic modeling and its applications in chemical risk assessment”. *Toxicology letters*, 138(1):9, 2003.
- [4] Andersen, Melvin E., Harvey J. Clewell, and ML Gargas. “Physiologically based pharmacokinetics and the risk assessment process for methylene chloride”. *Toxicology and Applied Pharmacology*, 87:185–205, 1987.
- [5] Andersen, Melvin E., Harvey Clewell III, and Kannan Krishnan. “Tissue Dosimetry, Pharmacokinetic Modeling, and Interspecies Scaling Factors”. *Risk Analysis: An International Journal*, 15(4):533–537, 1995.
- [6] Borm, Paul J.A. and Detlef Muller-Schulte. *Nanoparticles in Medicine*, 387–411. Particle Toxicology. CRC Press, Taylor & Francis Group, LLC, Boca Raton FL, 2007.
- [7] Boyce, Richard C. and William E. DiPrima. *Elementary Differential Equations and Boundary Value Problems*. John Wiley & Sons, Inc., Hoboken NJ, 1977.
- [8] Buzea, Cristina, Ivan I. Pacheco Blandino, and Kevin Robbie. “Nanomaterials and nanoparticles: sources and toxicity”. *Biointerphases*, 2(4):MR17–MR172, 2007.
- [9] Cahill, T., I. Cousins, and D. Mackay. “Development and application of a generalized physiologically based pharmacokinetic model for multiple environmental contaminants”. *Environmental Toxicology and Chemistry*, 22:26–34, 2003.
- [10] Champion, Julie A., Yogesh K. Katare, and Samir Mitragotri. “Particle shape: a new design parameter for micro- and nanoscale drug delivery carriers”. *Journal of Controlled Release*, 121:3–9, 2007.
- [11] Churg, Andrew. *Particle Uptake by Epithelial Cells*, p.401–435. Particle-Lung Interactions. Marcel Dekker, Inc., New York NY, 2000.
- [12] Clewell, Rebecca A. and Harvey J. Clewell III. “Development and specification of physiologically based pharmacokinetic models for use in risk assessment”. *Regulatory Toxicology and Pharmacology*, 50(1):129–143, 2008.

- [13] Dennison, James E., Melvin E. Andersen, Harvey J. Clewell, and Raymond S.H. Yang. "Development of a physiologically based pharmacokinetic model for volatile fractions of gasoline using chemical lumping analysis". *Environmental science & technology*, 38(21):5674, 2004.
- [14] Dennison, James E., Philip L. Bigelow, Moiz M. Mumtaz, and Melvin E. Andersen. "Evaluation of Potential Toxicity from Co-Exposure to Three CNS Depressants (Toluene, Ethylbenzene, and Xylene) Under Resting and Working Conditions Using PBPK Modeling". *Journal of Occupational and Environmental Hygiene*, 2(3):127, 2005.
- [15] Dixit, Rakesh, Jim Riviere, Kannan Krishnan, and Melvin E. Andersen. "Toxicokinetics and Physiologically Based Toxicokinetics in Toxicology and Risk Assessment". *Journal of Toxicology & Environmental Health: Part B*, 6(1):1, 2003.
- [16] Fox, Stuart Ira. *Human Physiology*. McGraw Hill, New York NY, 2006.
- [17] Freund, Rudolf, Ramon Littell, and Lee Creighton. *Regression Using JMP®*. SAS Institute Inc., Cary NC, 2003.
- [18] Garnett, Martin C. *Biodistribution of nanoparticles: insights from drug delivery*, 85–97. Nanotoxicology: Characterization, Dosing and Health Effects. Informa Healthcare USA, Inc., New York NY, 2007.
- [19] Garnett, M.C. "Delivery Systems for Cancer Drugs". Lecture. Online @ http://www.nottingham.ac.uk/ncmh/lecture_notes/D2DBT5/D2DBT5_DrGarnett_CancerDrugDelivery.doc, Apr 2004.
- [20] Garnett, MC and P. Kallinteri. "Nanomedicines and nanotoxicology: some physiological principles". *Occupational Medicine*, 56:p.307–311, 2006.
- [21] Gearhart, Jeffery M., Gary W. Jepson, Harvey J. Clewell, Melvin E. Andersen, and Rory B. Conolly. "Physiologically Based Pharmacokinetic Model for the Inhibition of Acetylcholinesterase by Organophosphate Esters". *Environmental Health Perspectives*, 51–60, 1994.
- [22] Geiser, Marianne, Barbara Rothen-Rutishauser, Nadine Kapp, Samuel Schurch, Wolfgang Kreyling, Holger Schulz, Manuela Semmler, Vinzenz Im Hof, Joachim Heyder, and Peter Gehr. "Ultrafine particles cross cellular membranes by non-phagocytic mechanisms in lungs and in cultured cells". *Environ. Health Perspect.*, 113(11):1555–1560, 2005.
- [23] Gibson, Rosemary M. *Understanding the potential neurotoxicology of nanoparticles*, 299–316. Nanotoxicology: Characterization, Dosing and Health Effects. Informa Healthcare USA, Inc., New York NY, 2007.
- [24] Green, S.B. "How many subjects does it take to do a regression analysis?" *Multivariate Behavioral Research*, 26:499–510, 1991.

- [25] Hagens, Werner I., Agnes G. Oomen, Wim H. de Jong, Flemming R. Cassee, and Adrienne J.A.M. Sips. "What do we (need to) know about the kinetic properties of nanoparticles in the body?" *Regulatory Toxicology and Pharmacology*, 49:217–229, 2007.
- [26] Hinds, William C. *Aerosol Technology: Properties, Behavior, and Measurement of Airborne Particles*. John Wiley & Sons, Inc., New York NY, 1999.
- [27] Hoet, Peter HM, Irene Bruske-Hohlfeld, and Oleg V. Salata. "Nanoparticles - known and unknown health risks". *Journal of Nanobiotechnology*, 2(12):1–15, 2004.
- [28] International Commission on Radiological Protection. *ICRP Publication 66: Human Respiratory Tract Model for Radiological Protection*. Elsevier Science, Inc., Tarrytown NY, 1994.
- [29] Jallouli, Youssef, Archibauld Paillard, Jiang Chang, Emmanuel Sevin, and Didier Betbeder. "Influence of surface charge and inner composition of porous nanoparticles to cross blood-brain barrier in vitro". *Int. J. Pharm.*, 344:103–109, 2007.
- [30] Jani, P., GW Halbert, J Langridge, and AT Florence. "Nanoparticle uptake by the rat gastrointestinal mucosa: quantitation and particle size dependency". *J Pharm Pharmacol*, 42:821–826, 1990.
- [31] Kandlikar, M., G. Ramachandran, A. Maynard, and B. Murdock. *Health risk assessment for nanoparticles: a case for using expert judgment*, 137–156. Nanoparticles and Occupational Health. Springer, Dordrecht The Netherlands, 1st edition, 2006.
- [32] Kedar, N.P. "Can We Prevent Parkinson's and Alzheimer's Disease?" *J. Postgrad. Med.*, 49(3):236–245, 2003.
- [33] Kent, Chris. *Basics of Toxicology*. John Wiley & Sons, Inc., New York NY, 1998.
- [34] Klaassen, Curtis D. *Casarett & Doull's Toxicology: The Basic Science of Poisons*. The McGraw-Hill Companies, Inc., New York NY, 2008.
- [35] Kreuter, Jorg. "Nanoparticulate systems for brain delivery of drugs". *Advanced Drug Delivery Reviews*, 47:p.65–81, 2001.
- [36] Kreyling, W., M. Semmler, F. Erbe, P. Mayer, S. Takenaka, and H. Schulz. "Translocation of ultrafine insoluble iridium particles from lung epithelium to extrapulmonary organs is size-dependent but very low". *J. Toxicol. Environ. Health*, 65A:1513–1530, 2002.
- [37] Kreyling, W. G., W. Moller, M. Semmler-Behnke, and G. Oberdorster. *Particle dosimetry: deposition and clearance from the respiratory tract and translocation*

towards extra-pulmonary sites, p.47–74. Particle Toxicology. CRC Press, Taylor & Francis Group, LLC, Boca Raton FL, 2007.

- [38] Kreyling, Wolfgang G. and Gerhard Scheuch. *Clearance of Particles Deposited in the Lungs*, p.323–376. Particle-Lung Interactions. Marcel Dekker, Inc., New York NY, 2000.
- [39] Krishnan, Kannan and Melvin E. Andersen. *Physiologically Based Pharmacokinetic Modeling in Toxicology*, 193–241. Principles and Methods of Toxicology. Taylor & Francis, Philadelphia PA, 4th edition, 2001.
- [40] Kuempel, Eileen D., Ellen J. O’Flaherty, Leslie T. Stayner, and Randall J. Smith. “A Biomathematical Model of Particle Clearance and Retention in the Lungs of Coal Miners, I. Model Development”. *Regulatory Toxicology and Pharmacology*, 34:69–87, 2001.
- [41] Kumar, Challa. *Nanomaterials- Toxicity, Health and Environmental Issues*. Wiley-VCH, KGaA, Weinheim, 2006.
- [42] Lani, James. “Multiple Regression”. On-line @ <http://www.statisticssolutions.com/methods-chapter/statistical-tests/multiple-regression/>, 2010.
- [43] Li, S.D. and L. Huang. “Pharmacokinetics and biodistribution of nanoparticles”. *Mol. Pharm.*, 5:496–504, 2008.
- [44] Linkov, Igor, Jeffery Steevens, Gitanjali Adlakha-Hutcheon, Erin Bennett, Mark Chappell, Vicki Colvin, J. Michael Davis, Thomas Davis, Alison Elder, Steffen Foss Hansen, Pertti Bert Hakkinen, Saber M. Hussain, Delara Karkan, Rafi Korenstein, Iseult Lynch, Chris Metcalfe, Abou Bakr Ramadan, and F. Kyle Satterstrom. “Emerging methods and tools for environmental risk assessment, decision-making, and policy for nanomaterials: summary of NATO Advanced Research Workshop”. *J. Nanopart. Res.*, 11:513–527, 2009.
- [45] Lockman, P.R., R.J. Mumper, M.A. Khan, and D.D. Allen. “Nanoparticle technology for drug delivery across the blood-brain barrier”. *Drug Development and Industrial Pharmacy*, 28(1):1–12, 2002.
- [46] Maynard, Andrew D. *Nanoparticle Safety - A perspective from the United States*, 118–131. Nanotechnology - Consequences for human health and the environment. The Royal Society of Chemistry, Cambridge UK, 1st edition, 2007.
- [47] Maynard, Andrew D. and Eileen D. Kuempel. “Airborne nanostructured particles and occupational health”. *Journal of Nanoparticle Research*, 7:587–614, 2005.
- [48] McCormick, P. Aiden. *Hypersplenism*, 771–778. Textbook of Hepatology: From Basic Science to Clinical Practice. Blackwell Publishing, Malden MA, 2007.

- [49] McNeil, Scott E. “Nanotechnology for the biologist”. *Journal of Leukocyte Biology*, 78:585–594, 2005.
- [50] Mohanraj, V.J. and Y. Chen. “Nanoparticles - A Review”. *Tropical Journal of Pharmaceutical Research*, 5(1):561–573, 2006.
- [51] National Institute for Occupational Safety and Health. *Approaches to Safe Nanotechnology: Managing the Health and Safety Concerns Associated with Engineered Nanomaterials*, DHHS (NIOSH) Publication #2009-125. Department of Health and Human Services, Centers for Disease Control and Prevention, 2009.
- [52] National Institute for Occupational Safety and Health. *Strategic Plan for NIOSH Nanotechnology Research and Guidance– Filling the Knowledge Gaps*, DHHS (NIOSH) Publication #2010-105. Department of Health and Human Services, Centers for Disease Control and Prevention, 2009.
- [53] Nemmar, A., P. Hoet, B. Vanquickenborne, D. Dinsdale, M. Thomeer, M. Hoylaerts, H. Vanbilloen, L. Mortelmans, and B. Nemery. “Passage of inhaled particles into the blood circulation in humans”. *Circulation- Journal of the American Heart Association*, 105:411–414, 2002.
- [54] Oberdörster, G., A. Maynard, K. Donaldson, V. Castranova, J. Fitzpatrick, K. Ausman, J. Carter, B. Karn, W. Kreyling, D. Lai, S. Olin, N. Monteiro-Riviere, D. Warheit, and H. Yang. “Principles for characterizing the potential human health effects from exposure to nanomaterials: elements of a screening strategy”. *Particle and Fibre Toxicology*, 2(8):1–35, 2005.
- [55] Oberdörster, G., Z. Sharp, V. Atudorei, A. Elder, R. Gelein, W. Kreyling, and C. Cox. “Translocation of Inhaled Ultrafine Particles to the Brain”. *Inhalation toxicology*, 16(6):437–445, 2004.
- [56] Oberdörster, G., Z. Sharp, V. Atudorei, A. Elder, R. Gelein, A. Lunts, W. Kreyling, and C. Cox. “Extrapulmonary translocation of ultrafine carbon particles following whole-body inhalation exposure of rats”. *J. Toxicol. Environ. Health Pt A*, 65(20):1531–1543, 2002.
- [57] Oberdörster, Günter, Eva Oberdörster, and Jan Oberdörster. “Nanotoxicology: An Emerging Discipline Evolving from Studies of Ultrafine Particles”. *Environmental Health Perspectives*, 113(7):823–839, 2005.
- [58] Oberdörster, Günter, Vicki Stone, and Ken Donaldson. “Toxicology of nanoparticles: A historical perspective”. *Nanotoxicology*, 1(1):2–25, 2007.
- [59] Owens III, D.E. and N.A. Peppas. “Opsonization, biodistribution, and pharmacokinetics of polymeric nanoparticles”. *Int. J. Pharm.*, 307:93–102, 2006.

- [60] Peters, T., J. D’Arcy, and P. Raynor. “Presentation at the 2007 American Industrial Hygiene Conference & Exposition: PDC 425 The FUN of Aerosols: Fine, Ultrafine, and Nano Particles in Workplace Atmospheres”. 2007.
- [61] Ramsey, John C. and Melvin E. Andersen. “A Physiologically Based Description of the Inhalation Pharmacokinetics of Styrene in Rats and Humans”. *Toxicology and Applied Pharmacology*, 73:159–175, 1984.
- [62] Reddy, Micaela B., Raymond S.H. Yang, Harvey J. Clewell, and Melvin E. Andersen. *Physiologically Based Pharmacokinetic Modeling Science and Applications*. John Wiley & Sons, Inc., New Jersey, 2005.
- [63] Riviere, Jim E. “Pharmacokinetics of nanomaterials: an overview of carbon nanotubes, fullerenes and quantum dots”. *Wiley Interdispl. Rev. Nanomed. Nanobiotechnology*, 1:26–34, 2009.
- [64] Riviere, Jim E. and C. Lang Tran. *Pharmacokinetics of Nanomaterials*, 127–152. *Nanotoxicology: Characterization, Dosing and Health Effects*. Informa Healthcare USA, Inc., New York, NY 10017, 1st edition, 2007.
- [65] Robinson, Peter J., Jeffrey M. Gearhart, Deirdre A. Mahle, Kyung O. Yu, Elaine A. Merrill, and Teresa R. Sterner. *Physiologically-Based Pharmacokinetic/Toxicokinetic Modeling in Risk Assessment*. Technical Report AFRL-HE-WP-TR-2005-0084, Air Force Research Laboratory Human Effectiveness Directorate, 2005.
- [66] Schulz, Holger, Peter Brand, and Joachim Heyder. *Particle Deposition in the Respiratory Tract*, p.229–290. *Particle-Lung Interactions*. Marcel Dekker, Inc., New York NY, 2000.
- [67] Shelley, M.L., R.L. Harris, and B.A. Boehlecke. “A Mathematical Model of Bronchial Absorption of Vapors in the Human Lung and its Significance in Pharmacokinetic Modeling”. *SAR and QSAR in Environmental Research*, 5:221–253, 1996.
- [68] Shelley, M.L., A.J. Wagner, S.M. Hussain, and C. Bleckmann. “Modeling the in vivo case with in vitro nanotoxicity data”. *International Journal of Toxicology*, 27:p.259–367, 2008.
- [69] Shvedova, Anna A., Tina Sager, Ashley R. Murray, Elena Kisin, Dale W. Porter, Stephen S. Leonard, Diane Schwegler-Berry, Victor A. Robinson, and Vincent Castranova. *Critical Issues in the Evaluation of Possible Adverse Pulmonary Effects Resulting from Airborne Nanoparticles*, 225–236. *Nanotoxicology: Characterization, Dosing and Health Effects*. Informa Healthcare USA, Inc., New York NY 10017, 1st edition, 2007.

- [70] STELLA[®] v.9.0.2. (modeling/simulation software), ISEE Systems, Lebanon NH, 2007.
- [71] Stolnik, S., L. Illum, and S.S. Davis. “Long circulating microparticulate drug carriers”. *Advanced Drug Delivery Reviews*, 16:195–214, 1995.
- [72] Storm, Gert, Sheila O. Belliot, Toos Daemen, and Danilo D. Lasic. “Surface modification of nanoparticles to oppose uptake by the mononuclear phagocyte system”. *Advanced Drug Delivery Reviews*, 17:31–48, 1995.
- [73] Tabata, Yasuhiko and Yoshito Ikada. “Effect of the size and surface charge of polymer microspheres on their phagocytosis by macrophage”. *Biomaterials*, 9:356–362, 1988.
- [74] Teeguarden, Justin G., Paul M. Hinderliter, Galya Orr, Brian D. Thrall, and Joel G. Pounds. “Particokinetics In Vitro: Dosimetry Considerations for In Vitro Nanoparticle Toxicity Assessments”. *Toxicological Sciences*, 95(2):300–312, 2006.
- [75] Tinkle, Sally S., James M. Antonini, Brenda A. Rich, Jenny R. Roberts, Rebecca Salmen, Karyn DePree, and Eric J. Adkins. “Skin as a Route of Exposure and Sensitization in Chronic Beryllium Disease”. *Environmental Health Perspectives*, 111(9):1202, 2003.
- [76] Tozer, Thomas N. and Malcolm Rowland. *Introduction to Pharmacokinetics and Pharmacodynamics: The Quantitative Basis of Drug Therapy*. Lippincott Williams & Wilkins, Baltimore MD, 2006.
- [77] Tran, C.L. and K. Donaldson. “Toxicological and Health Effects”. *International Conference on Nanotechnology Occupational and Environmental Health & Safety (NOEHS): Research to Practice*. 2006.
- [78] Tran, C.L., A.D. Jones, R.T. Cullen, and K. Donaldson. “Mathematical Modeling of the Retention and Clearance of Low-Toxicity Particles in the Lung”. *Inhalation toxicology*, 11(12):1059–1076, 1999.
- [79] Tran, Lang and Eileen Kuempel. *Biologically Based Lung Dosimetry and Exposure-Dose-Response Models for Poorly Soluble Inhaled Particles*, 351–386. Particle Toxicology. CRC Press, Taylor & Francis Group, LLC, Boca Raton FL, 2007.
- [80] Truskey, George A., Fan Yuan, and David F. Katz. *Transport Phenomena in Biological Systems*. Pearson Prentice Hall, Upper Saddle River NJ, 2009.
- [81] Vaia, R., D. Miracle, and T. Cruse. *Nanoscience and Technology at the Air Force Research Laboratory*. Technical Report AFRL WS 05-0015, Air Force Research Laboratory, 2005.

- [82] Wikipedia. “Mean value theorem”. On-line @ http://en.wikipedia.org/wiki/Mean_value_theorem#First_mean_value_theorem_for_integration, 2010.
- [83] Wilson Van Voorhis, Carmen R. and Betsy L. Morgan. “Understanding Power and Rules of Thumb for Determining Sample Sizes”. *Tutorials in Quantitative Methods for Psychology*, 3(2):43–50, 2007.
- [84] Yamamoto, Dirk P. and Michael L. Shelley. “A Mechanistic Model Prototype For Nanotoxicity Risk Analysis (poster presentation)”. *2009 American Industrial Hygiene Conference & Exposition*. Toronto ON, Canada, 2009.
- [85] Yamamoto, Dirk P. and Michael L. Shelley. “Developing a Mathematical Approach to Assess Nanoparticle Toxicokinetics (poster presentation)”. *2010 American Industrial Hygiene Conference & Exposition*. Denver CO, 2010.
- [86] Yamamoto, Dirk P. and Michael L. Shelley. “Mathematical Modeling of Cellular Transport Phenomena in a PBPK Model for Nanoparticle Exposures (podium presentation)”. *2010 American Industrial Hygiene Conference & Exposition*. Denver CO, 2010.
- [87] Yang, Wei, Jay I. Peters, and Robert O. Williams III. “Inhaled nanoparticles - a current review”. *International Journal of Pharmaceutics*, 356:239–247, 2008.

Vita

Lt Col Dirk Yamamoto was born in Minneapolis, Minnesota. After graduating from nearby Richfield High School in 1988, he studied Electrical Engineering at the University of Minnesota under a four-year Air Force Reserve Officer Training Corps (AFROTC) scholarship. He completed the undergraduate honors program, graduating with a Bachelor of Science in Electrical Engineering and receiving his Air Force commission in 1992. He was also the Top Graduate of his ROTC class and a nationwide AFROTC Distinguished Graduate. Lt Yamamoto's first assignment was at the Human Systems Center system program office (SPO), Brooks AFB, TX, where he worked as a 62E project engineer on various aircrew life support systems and chemical-biological warfare detection programs from 1993-1995. He completed a Master of Science in Engineering Systems Management from St Mary's University (TX) in 1995. Following his assignment in Texas, Lt Yamamoto cross-trained into the Bioenvironmental Engineering career field as a Biomedical Science Corps officer, and was assigned to Grand Forks AFB, ND, from 1995-1998. His next assignment involved base closure of McClellan AFB, CA, and the Sacramento Air Logistics Center (SM-ALC), where he served as the Base Radiation Safety Officer. After that assignment, Capt Yamamoto was selected for an AFIT/Civilian Institute-sponsored graduate program at University of Utah, where he completed a Master of Science in Public Health (Industrial Hygiene emphasis) in 2003. From 2003-2007, he served as an industrial hygiene consultant, project engineer, and program manager at Brooks City-Base, TX, responsible for development of the DOEHRS-IH and EESOH-MIS software systems for the Air Force Surgeon General and Civil Engineering communities. Maj Yamamoto was selected to attend AFIT in-residence in 2007 to complete a PhD in Systems Engineering. His follow-on assignment is to serve as faculty at AFIT/ENV, leading the instruction of the Master's of Industrial Hygiene program for the Bioenvironmental Engineering career field. Lt Col Yamamoto is a Certified Industrial Hygienist (CIH) and licensed Professional Engineer (PE). He recently completed Air War College, by correspondence. He is married and has two wonderful children.

REPORT DOCUMENTATION PAGE					Form Approved OMB No. 0704-0188	
<p>The public reporting burden for this collection of information is estimated to average 1 hour per response, including the time for reviewing instructions, searching existing data sources, gathering and maintaining the data needed, and completing and reviewing the collection of information. Send comments regarding this burden estimate or any other aspect of this collection of information, including suggestions for reducing this burden to Department of Defense, Washington Headquarters Services, Directorate for Information Operations and Reports (0704-0188), 1215 Jefferson Davis Highway, Suite 1204, Arlington, VA 22202-4302. Respondents should be aware that notwithstanding any other provision of law, no person shall be subject to any penalty for failing to comply with a collection of information if it does not display a currently valid OMB control number. PLEASE DO NOT RETURN YOUR FORM TO THE ABOVE ADDRESS.</p>						
1. REPORT DATE (DD-MM-YYYY)		2. REPORT TYPE		3. DATES COVERED (From — To)		
16-09-2010		Doctoral Dissertation		Aug 2007 — Sep 2010		
4. TITLE AND SUBTITLE Providing a Theoretical Basis for Nanotoxicity Risk Analysis Departing from Traditional Physiologically-Based Pharmacokinetic (PBPK) Modeling				5a. CONTRACT NUMBER		
				5b. GRANT NUMBER		
				5c. PROGRAM ELEMENT NUMBER		
6. AUTHOR(S) Yamamoto, Dirk P., Lt Col, USAF, BSC				5d. PROJECT NUMBER		
				5e. TASK NUMBER		
				5f. WORK UNIT NUMBER		
7. PERFORMING ORGANIZATION NAME(S) AND ADDRESS(ES) Air Force Institute of Technology Graduate School of Engineering and Management (AFIT/EN) 2950 Hobson Way WPAFB OH 45433-7765				8. PERFORMING ORGANIZATION REPORT NUMBER AFIT/DS/ENV/10-S01		
9. SPONSORING / MONITORING AGENCY NAME(S) AND ADDRESS(ES) Intentionally left blank				10. SPONSOR/MONITOR'S ACRONYM(S)		
				11. SPONSOR/MONITOR'S REPORT NUMBER(S)		
12. DISTRIBUTION / AVAILABILITY STATEMENT APPROVED FOR PUBLIC RELEASE; DISTRIBUTION UNLIMITED.						
13. SUPPLEMENTARY NOTES This material is declared a work of the U.S. Government and is not subject to copyright protection in the United States.						
14. ABSTRACT Novel properties of engineered nanoparticles that make them attractive may also present unique exposure risks. The traditional physiologically-based pharmacokinetic (PBPK) modeling assumption of instantaneous equilibration likely does not apply to nanoparticles. This simulation-based research begins with development of a model that includes diffusion, active transport, and carrier mediated transport. Eigenvalue analysis was used to examine model behavior to focus future research. Results show that cellular transport processes greatly affect biokinetics of nanoparticles. The new paradigm established by this research leverages traditional in vitro, in vivo, and PBPK modeling, but includes area under the curve to bridge animal testing results to humans. This allows assessment of risk and assists in setting appropriate exposure limits. The model provides critical understanding of nanoparticle biokinetics and allows estimation of total exposure. This effort highlights future research needs and demonstrates how modeling can be used as a tool to advance nanoparticle risk assessment.						
15. SUBJECT TERMS PBPK, Pharmacokinetic Modeling, Nanoparticles, Cellular Transport						
16. SECURITY CLASSIFICATION OF:			17. LIMITATION OF ABSTRACT	18. NUMBER OF PAGES	19a. NAME OF RESPONSIBLE PERSON	
a. REPORT	b. ABSTRACT	c. THIS PAGE			Dr. Michael L. Shelley (ENV)	
U	U	U	UU	205	19b. TELEPHONE NUMBER (include area code) (937)255-3636x7387; michael.shelley@afit.edu	